New findings on the onset of thermal disassembly in spallation reactions

Paolo Napolitani

24 Septembre 2004 IPNO-T-04-14

THESE

présentée par

Paolo NAPOLITANI

pour obtenir

LE GRADE DE DOCTEUR EN SCIENCES
DE L'UNIVERSITE PARIS XI ORSAY

Sujet: New findings on the onset of thermal disassembly
in spallation reactions

THÈSE

présentée

devant l'UNIVERSITÉ PARIS XI

pour l'obtention

du DIPLÔME DE DOCTORAT

par

Paolo NAPOLITANI

Titre de la thèse :

NEW FINDINGS ON THE ONSET OF THERMAL DISASSEMBLY IN SPALLATION REACTIONS

Soutenue le 24 Septembre 2004 devant la commission d'examen

Mr.	Bernard	BORDERIE	Rapporteur
Mr.	Alexander	BOTVINA	Examinateur
Mme.	Nimet	FRASCARIA	Président
Mme.	Francesca	GULMINELLI	Rapporteur
Mr.	Karl-Heinz	SCHMIDT	Directeur de thèse
Mr.	Laurent	TASSAN-GOT	Directeur de thèse

“Ma allora,” ardii commentare, “siete ancora lontano dalla soluzione...”
“Ci sono vicinissimo,” disse Guglielmo, “ma non so a quale.”
“Quindi non avete una sola risposta alle vostre domande?”
“Adso, se l’avessi insegnerei teologia a Parigi.”
“A Parigi hanno sempre la risposta vera?”

Umberto Eco
Il Nome Della Rosa

Abstract

"Thermal multifragmentation" is the process of multibody disassembly of a hot nucleus when the excitation is almost purely thermal. i.e. dynamical effects like compression (characteristic of ion-ion collisions at Fermi energy) are negligeable. Suited reactions are proton induced collision or ion-ion abrasion at relativistic incident energy. Thus we measured four systems at FRS in inverse kinematics: ^{56}Fe+p, ^{56}Fe+$^{\rm nat}$Ti, ^{136}Xe+p, ^{136}Xe+$^{\rm nat}$Ti at 1 A GeV. The inverse kinematics allows to observe all particles without any threshold in energy. This is a great advantage compared to experiments in direct kinematics, because only in inverse kinematics it is possible to obtain complete velocity spectra (without a hole for low velocities) for fully identified isotopes. The complex shape of the velocity spectra allows to identify the different deexcitation channels and it clearly shows the transition from a chaotic-dominated process (Gaussian cloud in velocity space) to a direct Coulomb- (or eventually expansion-) dominated process (shell of a sphere in velocity space). Different possible descriptions of the reaction process are discussed, based either on asymmetric fission or multifragmentation. The resulting physical picture is especially interesting for the ^{56}Fe+p, and ^{136}Xe+p systems: proton induced collisions could result in the split of the system in two or more fragments due to a fast break-up process. In this case, the configuration of the break-up partition is very asymmetric. The discussion will be extended to other characteristics, like the restoring of nuclear structure features in the isotopic production and the temperature dependence of the isotopic composition of the residues.

Key–Words

Spallation reactions – Multifragment emission and correlations – Nuclear reaction models and methods – Mass and neutron distributions.

Nouvelles approches pour l'étude de la multifragmentation thermique dans la spallation

Résumé

L'investigation des voies de décroissance d'un noyau excité au-dessus de l'énergie de liaison est l'un des grands sujets de recherche de la physique nucléaire. A partir des années quatre-vingt, la présence d'autres voies de décroissance que la fission et l'évaporation des résidus a été prédite et mise en évidence dans des systèmes nucléaires très excités. Ces voies ont été décrites comme l'explosion du noyau chaud et la dilution en de nombreux fragments, formés simultanément, dans des situations de coexistence de phases liquide et gazeuse de la matière nucléaire. Plusieurs types de collisions ont été étudiés pour induire l'excitation nécessaire à la désintégration du noyau et pour mettre en évidence les propriétés déterminantes de ce processus.

Un cas particulièrement intéressant est celui de la "multifragmentation thermique", le processus de cassure multiple d'un noyau chaud quand l'excitation est quasiment purement thermique, c'est à dire que les effets dynamiques comme la compression (caractéristiques des collisions d'ions lourds à l'énergie de Fermi) sont négligeables. Les réactions particulièrement adaptées sont les collisions induites par des protons. Au cours des dernières années, un large programme expérimental conduit au FRS (Fragment Separator, GSI, Darmstadt) focalisé sur l'étude des propriétés fondamentales des résidus de spallation et fragmentation a abouti à l'étude des systèmes

^{56}Fe+p, ^{56}Fe+$^{\mathrm{nat}}$Ti, ^{136}Xe+p, ^{136}Xe+$^{\mathrm{nat}}$Ti à 1 A GeV. Pour les quatre systèmes, la cinématique inverse nous a permis d'observer toutes les particules sans aucun seuil en énergie. La forme complexe du spectre en vitesse permet d'identifier des différents canaux de désexcitation et manifeste clairement la transition d'un processus en prévalence chaotique (nuage Gaussien dans l'espace des vitesses) vers un

processus dominé directement par la répulsion Coulombienne, ou éventuellement par l'expansion (couche sphérique dans l'espace des vitesses).

En nous concentrant sur les systèmes ^{56}Fe+p, ^{136}Xe+p, différentes descriptions possibles du processus de réaction sont discutées, basées soit sur la fission asymétrique ou sur la multifragmentation, caractérisée par des cassures rapides très asymétrique. Une discussion est dédiée explicitement à décrire comment, et sur la base de quelles hypothèses, il a été possible d'extraire des sections efficaces invariantes à partir des mesures inclusives. L'outil mathématique développé a ce propos constitue un nouveau concept dans les expériences au FRS et il établit un lien avec d'autres types de données expérimentales, comme celles obtenues dans des mesures exclusives. Une discussion particulière est étendue à d'autres aspects, comme la dépendance en température de la composition isotopique des résidus et le ré-établissement des caractéristiques de la structure nucléaire dans la production isotopique.

Ces recherches s'inscrivent dans le programme de l'aval du cycle électronucléaire, et de nombreuses applications comme la conception des cibles de spallation pour des réacteurs hybrides dédiés à la production d'énergie ainsi qu'à l'incinération des actinides peuvent en profiter. En particulier, nous avons mis en évidence que les effets de l'introduction de l'étape de la multifragmentation dans un modèle de spallation peuvent jouer un rôle important pour des énergies incidentes autour de 1 A GeV, et améliorer notablement la reproduction des données expérimentales tant pour la production isotopique que pour la description de la cinématique d'émission des fragments légers. Cette étude est aussi essentielle pour progresser dans l'étude fondamentale des phénomènes astrophysiques, comme la nucléosynthèse et les propriétés de la matière dans des étoiles à neutrons.

Contents

Preface **1**

1 Equilibration processes **5**

1.1 The formation of light residues 6

1.2 Measurement of light-fragment properties 10

2 Experiment and analysis **11**

2.1 The experiment 12

2.2 The FRagment Separator 12

2.2.1 Dispersion and high-resolution achromatic mode 13

2.2.2 Measurement and setting of the Ion-optic parameters . . . 17

2.3 Nuclide identification 20

2.3.1 Charge and Time of flight 21

2.3.2 Mass separation 24

2.4 Longitudinal velocities 24

2.5 Normalization to the beam dose 29

2.5.1 Beam-current monitor 29

2.5.2 Total number of fragments traversing the spectrometer . . . 31

3 Results **33**

3.1 Velocities 34

3.2 Nuclide cross section 43

4 The reaction mechanism **49**

4.1 Systematics of kinematical features 50

4.1.1 Absolute-velocity spectra 51

4.1.2 Kinetic-energy spectra 54

4.2 Nuclear-model calculations 57

4.2.1 Calculation of the excitation energy of the hot collision remnants 57

4.2.2 Sequential fission-evaporation decay 60

4.2.3 Fast break-up 65

5 Structural effects **75**

5.1 A schematic explanation 78

5.2 Reflection of the nuclear-structure effects in the emission velocity spectra. 79

6 Temperature and isotopic composition **81**

6.1 The neutron excess of the residues and the reaction mechanism . . . 82

6.2 The isospin thermometer 84

6.3 Interpretation of the experimental results for the systems ^{56}Fe+p , ^{56}Fe+$^{\mathrm{nat}}$Ti , ^{136}Xe+p , and ^{136}Xe+$^{\mathrm{nat}}$Ti 85

6.4 Calculations 88

6.5 Comparison with other systems 89

6.5.1 Systems with similar N/Z 89

6.5.2 Systems with different N/Z 91

7 Conclusion **93**

A General equations of motion **95**

A.0.3 The motion of a charged particle in a magnetic field 95

A.0.4 The dispersion function 98

A.0.5 The transfer matrix for a series of optical elements 100

B Numerical inversion of the relation between the measured velocity spectra and the cross sections **103**

C Isotopic cross sections **105**

Bibliography **125**

Preface

In November 2002, in Darmstadt, the synchrotron SIS was delivering a beam of ^{136}Xe at the incident energy of $1A$ GeV. The measurement of the production of all the heaviest residues generated in the interaction of the beam with a target of liquid hydrogen was the main purpose of the experiment. In the recent years a vast collection of similar data were measured, concentrating on the production of residues close to the mass of the projectile in ion-proton interactions at the incident energy of $1A$ GeV. This measurements were carried on by the groups *CHARMS ("Collaboration for High-Accuracy Experiments on Nuclear Reaction Mechanisms with the FRS")* at GSI (Darmstadt, Germany), *PACS ("Physique de l'Aval du Cycle et de la Spallation")* at IPN (Orsay,France), *"Grupo experimental de núcleos y partículas"*, at "Universidad de Santiago de Compostela" (Spain), and *DAPNIA/SPhN* at CEA (Saclay, France). The research carried on by the collaboration was aimed to creating the physical background for the design of Accelerator-Driven Systems, that are subcritical nuclear reactors where the neutron flux is kept constant by adding a neutron source. Such a system has the advantage of working as an amplifier of the neutron flux: the multiplicative medium of the nuclear reactor keeps a flux of neutrons that is proportional to the intensity of the neutron source. Recently, there is increasingly large interest in using this high neutron-flux to "incinerate" nuclear wastes. The high neutron-flux can also be exploited for the production of energy, like in a conventional thermo-nuclear system. In the latter case, the coupling of the subcritical neutron-multiplicative medium with a neutron source works as an "energy amplifier": the higher is the intensity of the source, the higher is the energy production. Unfortunately, this option, that would eliminate *ex fundamenta* any possibility for a deviation of the neutron flux, does not seem to be considered in future scenarios of large-scale energy production and will probably remain an academic utopia. It is evident that, for both the two applications, we need a very intense source of neutrons. Such a source can be obtained in a so-called *spallation* reaction, induced by directing relativistic protons on a neutron-rich target, like lead or uranium. In general, the heavy nuclides generated as residues of this reaction, are in average more proton rich with respect of the β-stable nuclei. Therefore, the more neutron rich is the nucleus used as a spallation target, the higher is the neutron flux generated by the neutron source. This justifies the interest for heavy, neutron-rich targets.

The number of measured reactions is limited, and it is necessary to achieve enough confidence with modelling the reaction mechanism in order to extrapolate to all the cases where the spallation process is not measured or is too difficult to be measured. For instance, some of the most studied systems, especially interesting for applications, like ^{208}Pb+p and ^{238}U+p at 1 A GeV, are complex because, after the collision, the nucleus leads to a competition between the sequential evaporation of nucleons and symmetric fission. If the cross sections for the production of the reaction residues are integrated and ordered as a function of the mass, we expect that the cross section is maximum for the mass of the projectile and gradually decreases for lighter masses. this behavior reflects the spallation-evaporation process. The slope of this portion of the spectrum is also a major test for a spallation-reaction model and for the general understanding of the process. It is in fact related to the excitation energy introduced in the system during the collision. The cross sections continue to decrease for lower masses till the trend reverses and the function increases towards another maximum, that coincides with symmetric fission.

The competition between evaporation and symmetric fission is particularly evident for any system obtained by bombarding heavier nuclei than gold with relativistic protons. In this case, it is very complicated to elaborate a spallation model on the basis of the experimental data. In particular, recent models that even contain a very consistent description of the fission process, and that provide a correct total reaction cross-section, have evident difficulties in reproducing the slope of the portion of the mass spectrum related to the spallation-evaporation residues. In general, this slope is too steep, so that the production yields of lighter nuclides than the projectiles is lower than the experimental values. This underestimation is the indication that the overall reaction mechanism was not fully understood. In the model, a too high fission probability would result into an underestimation of the competing evaporation production. Indeed, the evaporation production was underestimated by the models even when fission was very consistently described. Thus, when the formation of fission and evaporation residues is correctly described, the wrong slope of the mass spectrum associated to spallation-evaporation might reflect an inconsistency in the calculation of the excitation energy deposited in the system during the collision. A way to test the pertinence of a model in describing the collision mechanism is to verify that the spectrum of the emitted neutrons as a function of the kinetic energy is correct. The portion of the neutron spectrum associated to the highest energies is related to the neutrons emitted promptly in the collision and gives more direct indications about the collision mechanism. Some models that provide correct descriptions of the neutron spectra, still fail in reproducing the slope of the mass spectrum associated to spallation-evaporation. This inconsistency was even more preoccupying, because it seemed to hide a more fundamental problem.

A very fundamental problem could be that a spallation model is not sufficient to describe the interaction between protons and nuclei in the 1 A GeV incident-energy range. At the FRagment Separator the reaction ^{136}Xe+p was measured, in order to solve at least one major problem: ^{136}Xe is about as neutron rich as Lead, but too light to manifest symmetric fission. ^{136}Xe is actually the most neutron-rich stable isotope for which the contribution of fission could be neglected. It was somehow the ideal experimental case for measuring the slope of the mass spectrum related to evaporation, in the region of heavy masses.

Two years before, another system, ^{56}Fe+p at 1 A GeV, had been measured at the FRS. The experimental purpose of the measurement was different: iron is a structural material in an Accelerator Driven System and it was necessary to investigate its behavior when bombarded by relativistic protons. The heavy residues produced in ^{56}Fe+p were analyzed in my diploma-work at IPN in Orsay and, in parallel, it was also analyzed by Carmen Villagrasa at CEA in Saclay as the subject of her thesis, leading to results in consistent agreements. On the other hand, all the spallation models that were tested failed again in reproducing the slope of the mass spectrum (that, for this system, does not suffer from any disturbance related to symmetric fission!). The spectral region of about half the mass of the projectile was severely underestimated in most of the calculations. Initially, the light residues were disregarded because, while at this incident energies heavy residues are relatively easy to analyze, the light ones present several difficulties, related to the experimental conditions and, at the moment, we had no mathematical tools to overcome those complications. Later, these light nuclides attracted much interest, because light masses constituted the region where the reason for the inconsistencies of our models had still not been tested. After a new analysis of the ^{56}Fe+p system, extended to the full mass range, the expectations were encouraged. The lightest nuclides manifested in fact huge yields, higher than any spallation model could reproduce (even including light-particle emission). A deeper and deeper analysis of these nuclides revealed more and more new fundamental details about the emission kinematics, the reaction mechanism, thermal properties involved in the nuclear system, and even nuclear-structure effects. All these features are crucial for the realization of a nuclear-reaction model.

The increasing interest for light-nuclide production, inspired by the study of ^{56}Fe+p was the reason why the whole possible isotopic production in ^{136}Xe+p was measured, going beyond the standard plan of restricting to the heaviest residues. The "point of view" of the various spallation models was rather skeptical about the possibility that light residues could be produced with a measurable yields in the ^{136}Xe+p reaction. Indeed, like in ^{56}Fe+p , a remarkably generous light-fragment production showed up once more. In the past, several experiments were dedicated to study the collisions of relativistic protons with heavy ions. To cite one significant experiment, it should be mentioned that in 1986 L. N. Andronenko and collaborators measured the reaction induced by a beam of 1 A GeV protons on targets of nickel and silver. The systems are similar to those analyzed in this work and, again, high yields were measured for the light fragments. In that case, *multifragmentation* was the process advocated for describing the experimental results and, in successive theoretical works, A. Botvina and J. P. Bondorf demonstrated that a statistical multifragmentation model is capable to describe the yields of the light nuclides that were measured in the experiment. Especially at the end of the eighties, a dispute opened up and compound-nucleus models and multifragmentation models were alternatively proposed to explain the origin of light fragments in reactions induced by relativistic protons.

In the first chapter of the thesis the main argumentations that inspired this dispute are presented. In the second chapter, a brief description of the experimental device and of the data analysis is drown. The third chapter presents the most significant experimental results. Especially for the isotopic production obtained with the ^{136}Xe beam, a special effort was done to extend the range of isotopic cross sections from Lithium to Barium. A discussion is explicitly dedicated to describe how (and on the basis of which assumptions) the invariant cross sections could be extracted from the inclusive measurement. This approach is a new concept in the experiments with the FRagment Separator, and it creates a bridge with other kinds of experimental data, like those obtained in exclusive measurements. A large discussion on the reaction mechanism, expecially dedicated to ^{56}Fe+p , is illustrated in the fourth chapter. In the framework of this discussion, a possible solution to the original problem of describing the mass distribution is proposed. A more sophisticated model where spallation-evaporarion channels compete with fragmentation succeeds to provide a very satisfactory description of the whole measured mass spectra. This model is even capable to describe the complex features of the emission kinematics of the light fragments. In the fifth and sixth chapters special discussions are dedicated to extract considerations about the nuclear temperature from the isotopic component of the residues and to study the structural effects in the isotopic production, respectively. The seventh chapter constitutes the conclusions about a research that, initially aimed to obtaining the most complete survey on the isotopic production in two specific nuclear systems, even extended beyond, leading to new findings on the onset of thermal multifragmentation.

August 2004, P.N.

Chapter 1

Equilibration processes in the decay of hot remnants

Contents

1.1 The formation of light residues 6
1.2 Measurement of light-fragment properties 10

For the last decades, the investigation of the maximum excitation energy that a nuclear system can hold has remained as much a challenge as the description of the decay of a hot collision remnant, excited beyond the limits of nuclear binding. It was found that other decay modes than fission and evaporation prevail at high excitation energy. These modes are often described as a simultaneous break-up of the hot system in many parts, named “multifragmentation”. The excitation energy above which multifragmentation appears is still source of intense theoretical and experimental research. A point of particular interest is to recognise the distinguishing traits denoting this decay mode when the excitation is just sufficient for its onset. In line with this investigation, one foremost aspect of intense discussion is the connection of the kinematics of the residues to the kind of equilibration process involved in the earliest stages of the decay. This question is related to the complementary effort in constructing physical models to deduce the formation cross-sections of the residues when the excitation energy of the system is taken as initial condition. Especially light residues are suited for this purpose. Several details of the deexcitation mechanism could emerge from the kinematics of light fragments, due to the high sensitivity in probing the Coulomb field of the decaying system. Moreover, the distribution of their isotopic cross-sections carry additional signatures connected to different decay modes.

1.1 The formation of light residues

Light residues can be generated in several kinds of processes. One of these, the binary decay of an excited greatly thermalised complex, named compound nucleus, was widely studied [Sanders 1999]. We might also recall that evaporation of nucleons and light nuclei and symmetric fission are just the opposite extremes of the manifestation of this process: there is a gradual transition from very asymmetric to symmetric configurations in the division of decaying compound nuclei, and thus all binary decays of a greatly thermalised system can be named fission in a generalized sense. This generalization was introduced by Moretto [Moretto 1975, Moretto 1989]. A compound system far below the Businaro-Gallone point [Businaro 1955a, Businaro 1955b] (like iron-like nuclei) undergoes very asymmetric fission, resulting in a characteristic U-shape in the mass distribution of the yields. A minimum located at symmetry in the yield mass spectrum corresponds to a maximum placed at symmetry in the ridge lines of the potential. In configurations where a heavy partner is present, the whole decay process is dominated by the binary decay, and an additional evaporation of single nucleons would not disturb the kinematics remarkably. Such a process exhibits the typical feature of the population of the shell of a sphere in velocity space, in the reference frame of the mother nucleus.

At high excitation, multifragmentation becomes the competing process to compound-nucleus reactions. There is a fundamental difference between the binary decay of a compound nucleus and the simultaneous disintegration of a hot collision remnant in several constituents. The difference is in the kind of instabilities which are the reason for the decay, and is reflected in the kind and in the time evolution of the consequent equilibration process followed by the system.

A hot nucleus with an excitation energy above the threshold for emission of particles or clusters (including fission) has the possibility to decay by any of the open channels. If the excited system is not too hot, the favoured process is a reordering of its configurations: a great number of arrangements are available where all nucleons remain in states below the continuum, occupying excited single-particle levels around the Fermi surface. Oscillations in fission direction are included in this picture as well, but too rarely the fission barrier is reached. Rather seldom, compared with this thermal chaotic motion of the system, one nucleon acquires enough energy to pass above the continuum and may eventually leave the nucleus. This picture might be extended to cluster decay and to fission. Since this decay is a rare process, one evaporation event, or fission event, proceeds after the other, sequentially. In this process, the compound system follows a dynamic trajectory in deformation space, which is governed by the potential-energy surface and the dynamic properties of the compound system, related, for instance, to the inertia tensor and dissipation tensor. All decays are binary.

If the system becomes drastically more unstable, this picture is not valid any-

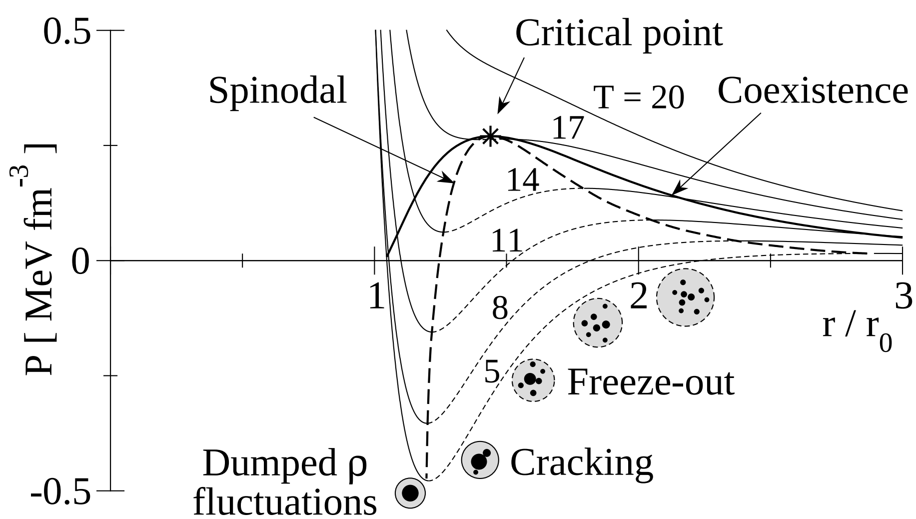

Figure 1.1: Idealistic plot of the phase diagram of nuclear matter, deduced from a Skyrme force ([Jaqaman 1983] parameterised according to [Levit 1985]). Pressure is shown as a function of the average relative nucleon distance r normalized to the distance r_0 at ground state. System configurations are drawn as possible final results of the expansion phase. When the thermalization path leads to the coexistence region, out of the spinodal region, dumped density fluctuations occur. In the spinodal region density fluctuations are unstable and lead to cracking. At low density freeze-out is attained with different possible partition configurations: fragments are free to leave the system.

more. The exploration of possible states of the excited system includes numerous unstable configurations. Thus, the disintegration can not be understood as a sequence of binary decays, but rather portrayed as a simultaneous break-up in several constituents [Randrup 1981, Gross 1997, Botvina 1985a, Bondorf 1985, Bondorf 1995]. The disintegration is simultaneous in the sense that it evolves in so short a time interval (10^{-22}-10^{-21}s) that the ejected fragments can still exchange mutual interactions during their acceleration in the Coulomb field of the system. In heavy-ion collisions, part of the excitation could be introduced in the system in the form of compressional energy. According to the impact parameter and the incident energy, the interaction might result in a very complex interplay between dynamic effects (beside compression, also deformation and rotation degrees of freedom) and thermal excitation. This is the case of central collisions in the Fermi-energy range. On the contrary, peripheral heavy-ion collisions at relativistic energies may be rather pictured according to an "abrasion" process [Gaimard 1991, Brohm 1994], where the remnant is formed by the spectator nucleons, heated by mainly thermal energy. In this case, the role of compressional energy has minor incidence. Even with proton projectiles, the multifragmentation regime might be accessible when very high excitation is introduced in the nucleus. In reactions induced by relativistic protons (but also by very light nuclei), the dynamic effects of the collision have even smaller importance. The excitation energy is almost purely thermal. Some authors even attributed the specific name of "thermal multifragmentation" to this particular process (see the review articles [Karnaukhov 1999, Karnaukhov 2003a]). It might be suggested that proton-induced relativistic collisions are better suited than ion-ion collisions for investigating thermal properties of nuclear matter (e.g. [Karnaukhov 1999, Hirsch 1984, Andronenko 1986, Kotov 1995, Avdeyev 1998]). In finite nuclei, the transition from the fission-evaporation mode to multifragmentation manifests rather smoothly. This opening of break-up channels even inspired interpretations in line with the liquid-gas phase transition of nuclear matter [Richert 2001, Chomaz 2004, Pochodzalla 1995, Borderie 2002]. The similarity of the nucleon-nucleon interaction with the Lennard-Jones molecular potential suggests that infinite neutral nuclear matter resembles a Van-der-Waals fluid [Sauer 1976]. As shown in fig. 1.1, also in the phase diagram of nuclear matter an area of liquid-gas coexistence can be defined. In this region, the "dense" phase of nuclear droplets is in equilibrium with the "gaseous" phase of free nucleons and light complex particles. Within the Hartree-Fock approximation, according to the type of Skyrme force chosen for obtaining the nuclear equation of state, the critical temperature T_c was calculated to vary in a range of around 15-20 MeV for nuclear matter [Sauer 1976, Jaqaman 1983, Levit 1985]. (One of the latest investigations, based on an improved Fisher's model [Elliott 2002] indicated $T_c = 6.7 \pm 0.2 MeV$ for finite nuclear systems. This value is source of controversy, e.g. [Natowitz 2002, Natowitz 2002, Gulminelli 2002, D'Agostino 2003, Karnaukhov 2003a, Karnaukhov 2003b]). During the reaction process, the system explores different regions of the phase diagram. Since at relativistic energies the collision is related to short wavelengths, the hot remnant should reach high positive values of pressure P due to thermal energy (rather than mechanical compression, characteristic of Fermi-energy collisions) without deviating sensibly from the initial density ρ_0. It is commonly assumed that at this stage the system is still not thermalised and it undergoes expansion in order to attain equilibrium (There exist also opposite interpretations assuming thermalization already before expansion and a successive "Big-Bang-like" expansion out of equilibrium [Campi 2003]). If the initial pressure is high enough, the subsequent expansion could lead to rather low densities, and the system, after dissipating the incoming momentum, could reach a point belonging to the spinodal region. Due to the inverse relation between pressure and density $dP/d\rho < 0$, this region is unstable, and density fluctuations are magnified. The nucleus breaks apart due to spinodal instability. The system disassembles also due to Coulomb instability. The inclusion of the long-range Coulomb interaction in the equation of state was introduced by Levit and Bonche [Levit 1985], with the result that the solution of the coexistence equation vanishes above a "limiting temperature" T_{lim}, in general much lower than T_c, depending on the conditions taken for the calculation (see also [Jaqaman 1989a, Jaqaman 1989b]). Density fluctuations reflect a continuous evolution of the size and number of nuclear droplets from a configuration to another [Bugaev 2001]. If the average mutual distance among the nucleons exceeds the strong nuclear interaction range (i.e. about $\sqrt{<\sigma_n>/\pi}$, where $<\sigma_n>$ is the average nucleon-nucleon collision cross section), the break-up configuration "freezes" and the formed nuclei and nucleons fly away freely, all carrying signatures of the so-called freeze-out temperature of their common source. From comparing results from different experimental approaches e.g. [Hirsch 1984, Pochodzalla 1995, Schmidt 2002, Napolitani 2002b] this temperature is found to be restricted to a range of 5 to 6 MeV (corresponding to a range of excitation energy per nucleon around 2.5 to 3.5 MeV), quite independently of the reaction. This finding, not directly compatible with the phase diagram of ideal nuclear matter even suggested to search for a "characteristic temperature" of fragmentation [Friedman 1988]. The break-up configuration at freeze-out is expected to reflect the excitation energy of the system. The dense phase of highly heated systems should have the aspect of an ensemble of copious almost-equal-size light fragments. At reduced excitation, just sufficient for attaining the freeze-out, the break-up partition might evolve to more asymmetric configurations, where the formation of a heavy fragment close to the mass of the hot remnant is accompanied by one or more light fragments and clusters. As an extreme, this configuration might even reduce to a binary asymmetric decay. In the case of a very asymmetric split of the system, the partition multiplicity has minor influence on the kinematics of the light ejectiles. The emission of light particles populates spherical shells in velocity space and can not be easily distinguished by the kinematics from a binary decay when large mass-asymmetries characterize the partition. A binary or binary-like decay issued from a break-up configuration is a "fast" process. Compared to asymmetric fission, asymmetric break-up decays should result in a similar U-shape of the mass spectra of the yields. On the other hand, break-up decays should be reflected in the higher magnitude of the yields, and in the emission kinematics that, still mostly governed by the Coulomb field, should exhibit an additional contribution due to the eventual expansion of the source.

1.2 Measurement of light-fragment properties

Great part of the information on light-particle emission at high excitation energies was collected in 4-π-type experiments, suited for measuring the multiplicity and the correlations of intermediate-mass fragments [Schüttauf 1996b, Marie 1998, Scharenberg 2001]. Still, the measurement of correlations and the linear-momentum-transfer was the basis for pursuing intense researches on the transition from the formation of compound nuclei to multifragmentation [Klotz-Engmann 1987, Klotz-Engmann 1989].

In this work, we discuss additional results derived from new inclusive measurements of the reactions ^{56}Fe+p, ^{56}Fe+$^{\mathrm{nat}}$Ti, ^{136}Xe+p and ^{136}Xe+$^{\mathrm{nat}}$Ti at 1 A GeV, effectuated in inverse kinematics with the FRagment Separator (FRS) [Geissel 1992] at GSI (Darmstadt). The experimental set-up was not intended to measure multiplicity and correlations, but to provide formation cross sections and high-resolution velocity spectra for isotopically identified projectile-like residues. The excitation of the ^{56}Fe+p and ^{136}Xe+p systems consists of purely thermal energy, and it is just high enough to approach the conditions for the onset of multifragmentation. On the basis of these data we search for the properties of the early appearance of break-up events and their competition with compound-nucleus emission. The systems ^{56}Fe+$^{\mathrm{nat}}$Ti and ^{136}Xe+$^{\mathrm{nat}}$Ti are compatible with an abrasion picture. The excitation energy deposited in the projectile spectator, still mostly of thermal nature, establishes the dominance of multifragmentation in the decay process. We will especially discuss the differences in the kinematics of light-fragment emission in the two systems, conditioned by two different levels of excitation magnitude.

Chapter 2

Experiment and analysis procedures

Contents

2.1 The experiment 12

2.2 The FRagment Separator 12

2.2.1 Dispersion and high-resolution achromatic mode 13

2.2.2 Measurement and setting of the Ion-optic parameters . . 17

2.3 Nuclide identification 20

2.3.1 Charge and Time of flight 21

2.3.2 Mass separation 24

2.4 Longitudinal velocities 24

2.5 Normalization to the beam dose 29

2.5.1 Beam-current monitor 29

2.5.2 Total number of fragments traversing the spectrometer . . 31

2.1 The experiment

The experiments were performed at GSI (Darmstadt) in two sessions: in October 2000 a primary beam of ^{56}Fe was used and in November 2002 a ^{136}Xe beam was used. The primary beam was delivered by the heavy-ion synchrotron SIS at an energy of 1 A GeV. The target was constituted of liquid hydrogen (with a thickness of 87.3 mg/cm^2) contained in a cryostat with thin titanium windows (36.3 mg/cm^2 in total), wrapped in thin Mylar foils ($C_5H_4O_2$, total thickness: 8.3 mg/cm^2) for thermal insulation. In the target area, other layers of matter intersected the ion-beam: the accelerator-vacuum window of titanium (4.5 mg/cm^2) and the beam-current monitor. The latter was composed of aluminum foils (8.9 mg/cm^2) at the time of the measurement with the ^{56}Fe beam, and it was successively replaced by titanium foils (13.5 mg/cm^2) before running the experiment with the ^{136}Xe beam. In order to disentangle the production and the physical results related to the interaction with hydrogen from the contribution associated to the other materials, the whole experimental runs were repeated in identical conditions, after replacing the target by titanium foils having the same thickness of the cryostat windows and wrapped in Mylar foils having the same thickness of the cryostat insulation. This procedure did not only determine the disturbing contributions in the measurement of the ^{56}Fe+p and ^{136}Xe+p systems, but it also provided additional experimental data on other reaction systems. With some arbitrariness we name *titanium target* ($^{\mathrm{nat}}$Ti) the ensemble of the titanium foils replacing the cryostat window, the Mylar wrapping, the accelerator-vacuum window and the beam-current monitor. Unfortunately, the measurement of the ^{56}Fe+$^{\mathrm{nat}}$Ti and ^{136}Xe+$^{\mathrm{nat}}$Ti systems accounts also for non-titanium nuclei, the pollution of which corresponds to their portion in the total number of target nuclei per area and is equal to 25.9% (Al) + 7.2% (Mylar) = 33.1%. It should be remarked that these components are not placed at the same distance from the entrance of the spectrometer. Fragments produced in the beam-current monitor or in the accelerator-vacuum window could have lower probabilities to be registered in the experiment since the angular acceptance is reduced by factors of 0.33 and 0.25, respectively, compared to products from the titanium foils replacing the cryostat. Henceforth, we refer to the liquid hydrogen as *proton target* (p). In this case no polluting contributions are included in the final results.

2.2 The FRagment Separator

The advantage of studying relativistic reactions in inverse kinematics is that all collision products leave the target with velocities close to the beam velocity and they can be analyzed in-flight, by tracking their trajectories in a magnetic field, by measuring their momenta and by registering their energy-loss in matter. The collision products were analyzed inclusively by the FRagment Separator (FRS, Darmstadt) set in *high-resolution achromatic mode*. A schematic view of its main components and functioning is presented in fig. 2.1

2.2.1 Dispersion and high-resolution achromatic mode

The spectrometer FRS is composed of a series of four large bending dipole magnets positioned behind the target. To focus the beam of reaction products, quadrupole magnets are placed in front and behind the dipoles. The magnetic fields are set so that the particle trajectories encounter a dispersive lattice and split apart according to the different momenta. The motion of a particle of magnetic rigidity $B\rho$, charge q and momentum $p = qB\rho$ in a dispersive magnetic field can be described in terms of the *dispersion function*, defined as

$$D(s_0) = \frac{x(s_0)}{\delta} \quad , \tag{2.1}$$

where x is the transverse displacement in the horizontal plane from the reference-particle trajectory s_0, and δ is the *momentum deviation* with respect to a reference particle of momentum $p_0 = qB\rho_0$, defined by the relation

$$\delta \doteq \frac{p - p_0}{p_0} = \frac{B\rho - B\rho_0}{B\rho_0} \quad . \tag{2.2}$$

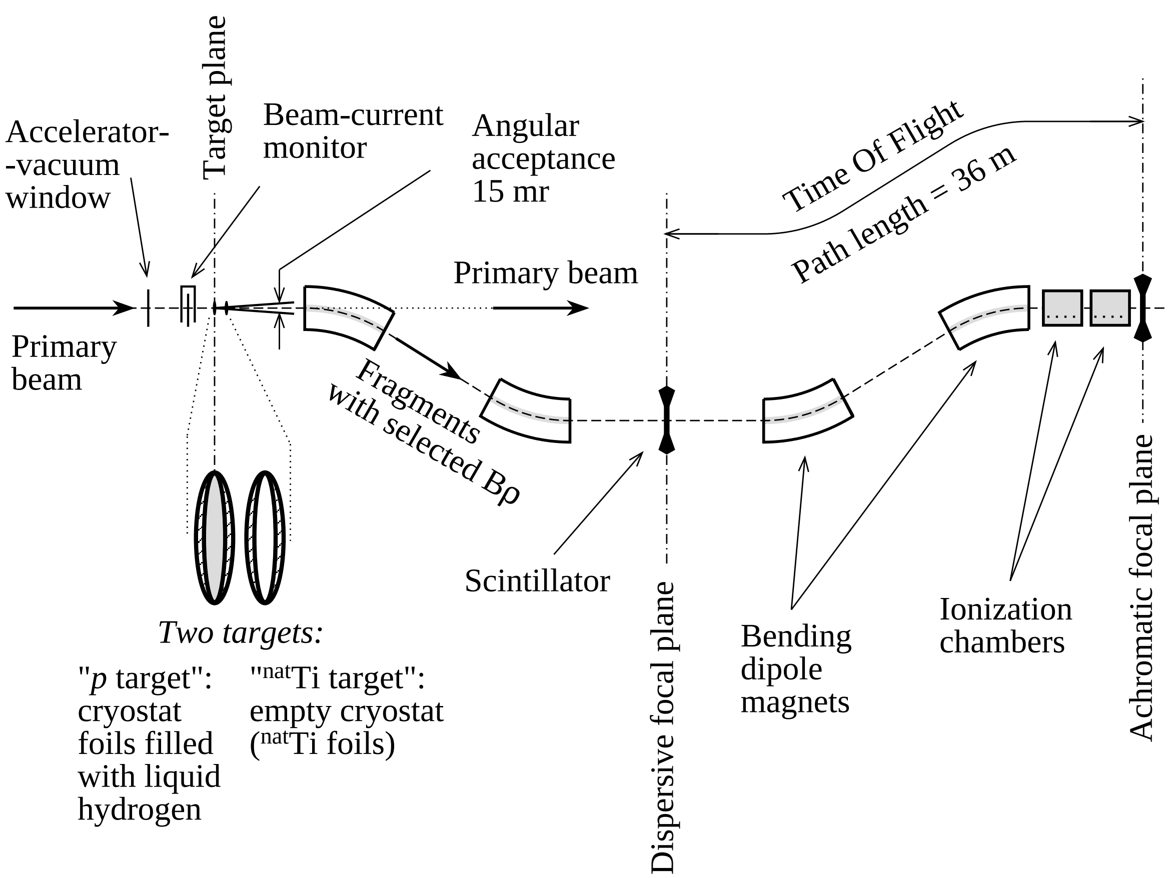

Figure 2.1: Standard layout of the FRagment Separator FRS. The positions of the four dipole magnets, the focal planes and the main detectors are shown in a horizontal plane view.

As demonstrated in the appendix A, the equations describing the motion of charged particles in the horizontal plane can be written in the following form:

$$\begin{pmatrix} x(s_0) \\ x'(s_0) \end{pmatrix} = \underbrace{\begin{pmatrix} g(s_0) & h(s_0) \\ g'(s_0) & h'(s_0) \end{pmatrix} \begin{pmatrix} x_i \\ x'_i \end{pmatrix}}_{\text{HARMONIC TERM}} + \underbrace{\delta \begin{pmatrix} D_i \\ D'_i \end{pmatrix}}_{\text{DISPERSION TERM}} \quad , \tag{2.3}$$

where the prime represents a derivative with respect of the curvilinear coordinate associated to the path length s_0 travelled by the reference particle. x_i and x'_i are initial conditions, and D_i a partial solution of the dispersion equation (see appendix A, eq (A.38)). We recognise a first term, which we may call *harmonic*, that comes from the Hill equation (A.40) and describes the transverse oscillation of a particle about its equilibrium trajectory. This is basically due to the strong focusing of the quadrupole magnets. The second term indicated as *dispersion term* introduces the dependence of the actual trajectory on the momentum deviation, with respect to the reference path s_0 and, therefore, fixes the equilibrium trajectory followed by the actual particle. The dispersion term is crucial for the identification of the fragment masses. By adding the trivial equation $\delta = \delta$ we can write the equations (2.3) in terms of *transfer matrix* $\mathcal{T}_i^{s_0}$:

$$\mathcal{X}(s_0) = \mathcal{T}_i^{s_0} \mathcal{X}_i \quad , \tag{2.4}$$

with

$$\mathcal{X}_i = \begin{pmatrix} x_i \\ x'_i \\ \delta \end{pmatrix} \quad , \quad \mathcal{X}(s_0) = \begin{pmatrix} x(s_0) \\ x'(s_0) \\ \delta \end{pmatrix} \quad , \quad \mathcal{T}_i^{s_0} = \begin{pmatrix} g(s_0) & h(s_0) & D_i \\ g'(s_0) & h'(s_0) & D'_i \\ 0 & 0 & 1 \end{pmatrix} \quad ,$$

The dispersion $D(s_0)$ has a maximum value in the middle of the beam-line, between the second and the third dipole, in correspondence with a focal plane. The optical property of a focal plane is the existence of a *point-to-point imaging* relation with respect to the initial plane, which corresponds to the target plane of the FRagment Sepatator (indicated by the number 0). This means that any particle with given momentum p issued from a point x_0 in the target plane hits the focal plane in a corresponding image point x_2, independently on the initial angle x'_0. As a consequence, the element $t_{1,2}$ of the matrix $\mathcal{T}_0^2$ is equal to zero.

This focal plane will be generally referred to as the *dispersive focal plane* (indicated by the number 2). A particle intersects the dispersive focal plane in a point x_2 that depends on the momentum p. The motion of particles between the target plane and the dispersive focal plane is described by the transfer matrix

$$\mathcal{T}_0^2 = \begin{pmatrix} g_0 & 0 & D_2 \\ g'_0 & h'_0 & D'_2 \\ 0 & 0 & 1 \end{pmatrix} \quad .$$

We could assume that the target is point-like and impose $x_0 = 0$. As a consequence, even though the trajectories of the reaction products split apart due to the different

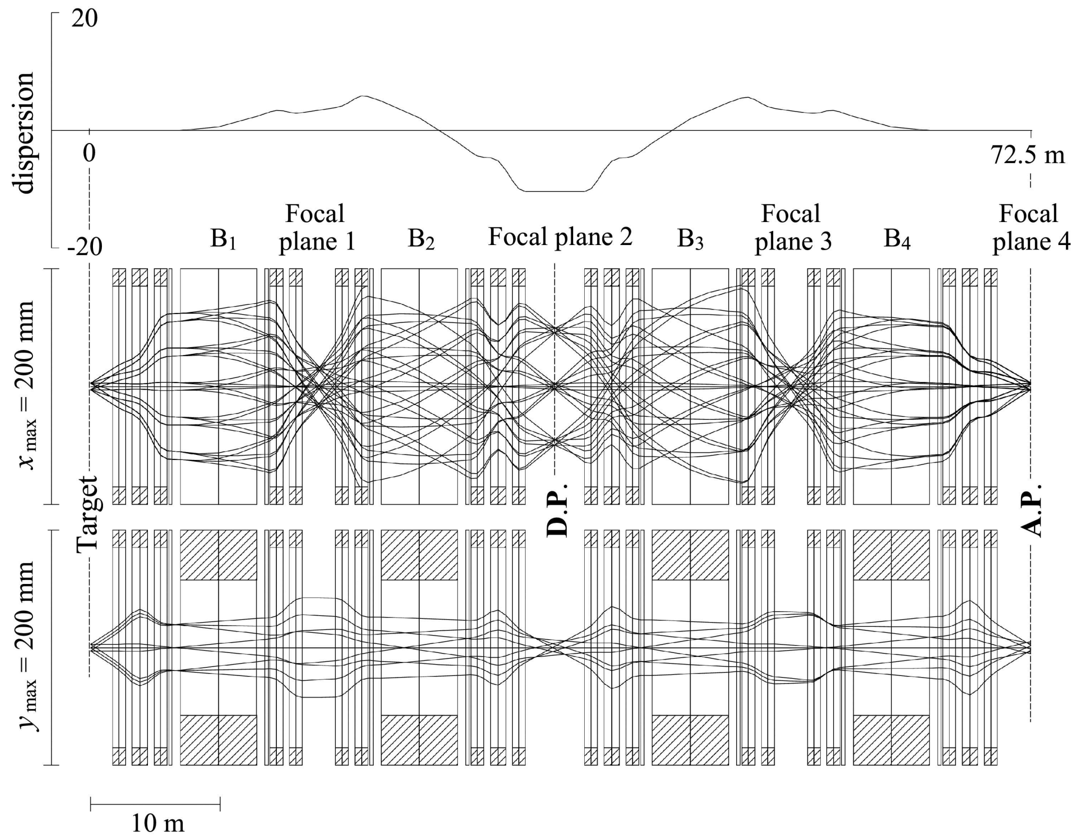

Figure 2.2: Simulation of the operation of the FRagment Separator in high-resolution achromatic mode. *Top.* Evolution of the dispersion along the beam axis in the FRagment Separator. *Centre.* Horizontal plane. Thirty trajectories originating from two spatially distinct points in the target plane for particles differing for having five different emission angles and three different momenta. *Bottom.* Vertical plane. Three spatially distinct points and three emission angles are chosen.

momenta and initial angles, they will then converge to focal points in the horizontal plane on the dispersive focal plane at positions depending on the momentum deviation δ only. As an example, these properties of the ion-optics are simulated in fig. 2.2. The spectrometer was operated in an overall achromatic mode, so that all reaction products encounter an *achromatic focal plane* (indicated by the number 4) at the end of the beam-line, in correspondence of which the momentum dispersion vanishes (In the transfer matrix we set the $t_{1,3} = t_{2,3} = 0$). This means that all particles issued from a given point in the target plane will focus in a corresponding point in the achromatic focal plane independently on their angle spread and momentum. The transfer matrix describing the particle motion between the target plane and the achromatic focal plane has the form

$$\mathcal{T}_0^4 = \begin{pmatrix} g_0 & 0 & 0 \\ g_0' & h_0' & 0 \\ 0 & 0 & 1 \end{pmatrix} \quad .$$

The motion of particles between the dispersive focal plane and the achromatic focal plane is described by a transfer matrix similar to the one associated to the first half of the spectrometer

$$\mathcal{T}_2^4 = \begin{pmatrix} g_2 & 0 & D_4 \\ g_2' & h_2' & D_4' \\ 0 & 0 & 1 \end{pmatrix} \quad .$$

From the first row of the equation of motion $\mathcal{X}_2 = \mathcal{T}_0^2 \mathcal{X}_0$ we obtain an expression to relate the momentum deviation δ to the dispersion D_2 by the knowledge of the position in the dispersive focal plane:

$$\delta = \frac{x_2}{D_2} \quad . \tag{2.5}$$

Similarly, from the first row of the equation $\mathcal{X}_4 = \mathcal{T}_2^4 \mathcal{X}_2$ we obtain

$$\tilde{\delta} = \frac{x_4 - g_2 x_2}{D_4} \quad , \tag{2.6}$$

where we indicated $\tilde{\delta}$ the momentum deviation in the second half of the spectrometer. $\tilde{\delta}$ could differ from δ due to the presence of matter (detectors) between the second and the third dipole. In this case, the initial momentum p changes due to the energy-loss in matter. If we assume $\tilde{\delta} \approx \delta$, we can combine the equations (2.5) and (2.6) in $g_2 D_2 + D_4 = x_4/\delta$. If the optics is achromatic, x_4 is the image of $x_0 = 0$, and we can impose $x_4 = 0$. Thus we obtain the following *condition of achromatism*:

$$g_2 = -\frac{D_4}{D_2} \tag{2.7}$$

From the definitions (2.1) and (2.2), we can write the dispersion D_2 and D_4 in terms of magnetic rigidity:

$$D_2 = \frac{B\rho_0}{(B\rho - B\rho_0)} \, x_2 \quad , \tag{2.8}$$

$$D_4 = \frac{B\rho_0}{(\widetilde{B\rho} - B\rho_0)} \, (x_4 - g_2 x_2) \quad , \tag{2.9}$$

where $B\rho$ and $\widetilde{B\rho}$ are the values of the magnetic rigidity of the tracked particle in the first and in the second half of the spectrometer, respectively. It should be observed that like the momentum or the energy, the magnetic rigidity is a property of the particle and not of the optics. On the other hand, the magnetic field B, the curvature radius ρ, and the dispersion D_2 and D_4 and the magnification factor g_2 are characteristics of the ion-optics.

2.2.2 Measurement and setting of the Ion-optic parameters

At the beginning of the experiment the optics was set so that the primary beam of ^{56}Fe or ^{136}Xe (with the target off-beam) was directed through the spectrometer crossing both the dispersive focal plane and the achromatic focal plane in the centre. This optic setting defined the reference trajectory s_0 and the curvature radius ρ_0. The complete set of all the magnetic fields (of dipole and quadrupole magnets) constituting the spectrometer were registered in a magnetic-field reference file. The magnetic fields of the first two dipoles B_1 and B_2 were set to close values (differing of around 1%) and in the following we will simply indicate them by their average $B_{12} = (B_1 + B_2)/2$. Also the magnetic fields of the third and fourth dipole were almost identical and we will refer to their average $B_{34} = (B_3 + B_4)/2$.

In order to scan all the magnetic rigidities (and therefore the momenta) of the reaction products, the magnetic fields had to be changed several times during the whole experiment. On the contrary, the parameters D_2, D_4 and g_2, crucial for the data analysis were measured at the beginning of the experiment with specific calibration runs, and were then fixed as constant values for the whole experiment. In order to keep these optics parameters unchanged the magnetic fields of the ensemble of magnets where changed by applying two scaling factors with respect to the magnetic-field reference file: one applied to the first half of the spectrometer (from the target plane to the dispersive focal plane), the other applied to the second half (from the dispersive focal plane to the achromatic focal plane). The two scaling factors, though very similar, differ due to the presence of layers of matter with non-negligible thickness (scintillating detectors or degraders) intersecting the ion-beam in proximity of the dispersive focal plane.

We should recall that the reference trajectory s_0 was set in order to intersect the dispersive focal plane and the achromatic focal plane in the centre. Therefore, the measurement of the distance of the crossing point of a particle in the dispersive and achromatic focal planes from the centre coincides with the spacial deviation from the reference trajectory x_2 and x_4, respectively. The measurement of the positions x_2 and x_4 should be as accurate as possible. Scintillating detectors were preferred due to their homogeneous material. The use of non-homogeneous detectors like multiwires would in fact affect the ion-optics. Nevertheless, multiwire detectors provide a better linearity of the signal. For this reason, calibration experiments were dedicated to measure the non-linearity of the scintillator by placing an additional multiwire detector behind the scintillator. Supposing that the signal given by the multiwire is perfectly linear, the distortion of the signal of the scintillator mounted in the dispersive focal plane is the curve shown in the diagram (a) of fig. 2.3. This distortion was then eliminated in the data analysis.

Once a precise measurement of x_2 is available, The dispersion D_2 can be measured by applying the equation (2.8), that relates the position x_2 to the magnetic rigidity of a particle. Eq. (2.8) can be written in the form

$$B\rho = B\rho_0 \left(1 + \frac{x_2}{D_2}\right) \quad , \tag{2.10}$$

or

$$B\rho = B_{12}\rho_0 \left(1 + \frac{x_2}{D_2}\right) \quad , \tag{2.11}$$

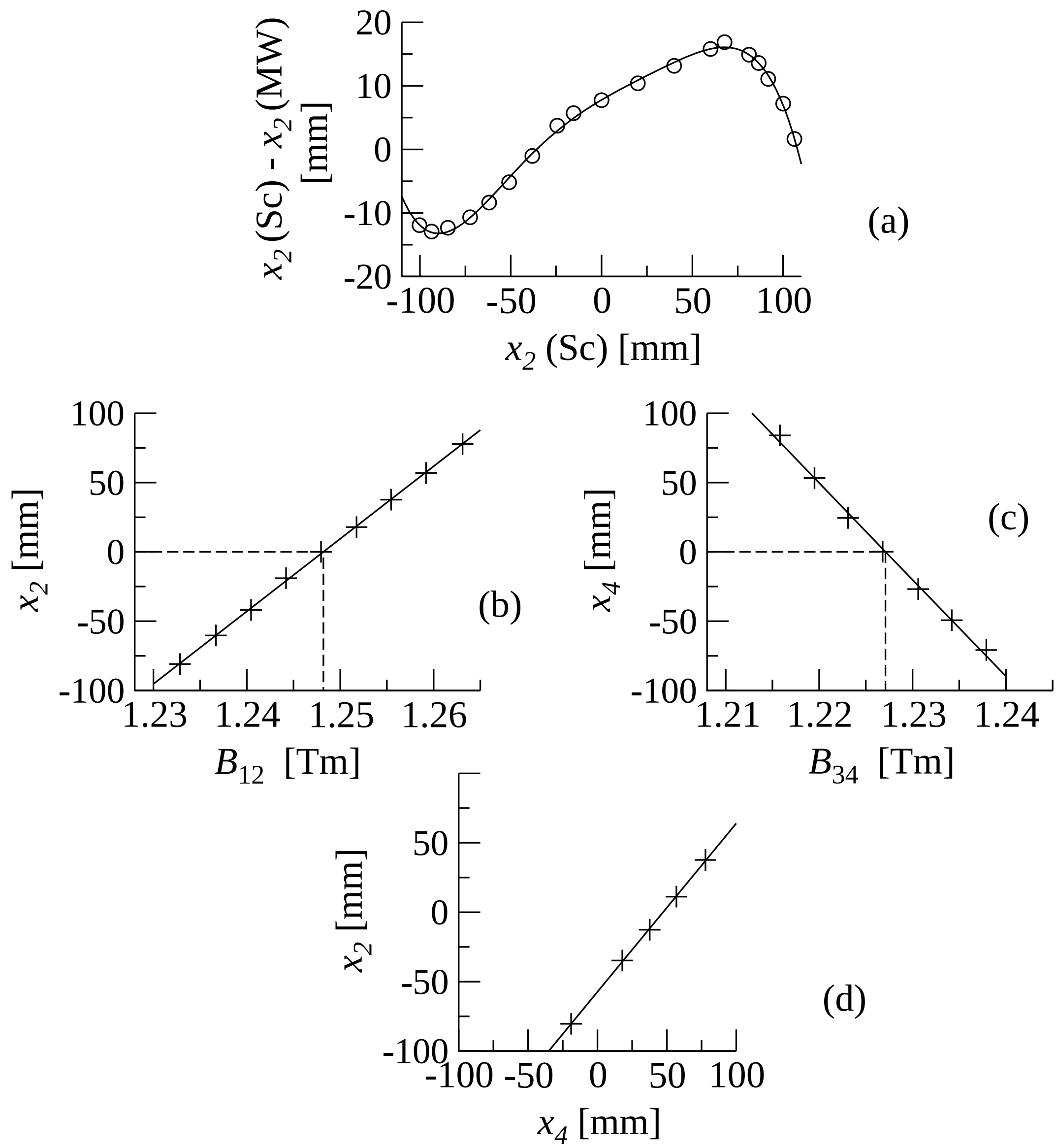

Figure 2.3: Experimental determination of the main parameters for the data-analysis in the measurement with a ^{136}Xe beam. (a) Difference in the measurement of the position by the scintillator (Sc) and the multiwire (MW) detectors in the dispersive focal plane. (b) Determination of D2. (c) Determination of D4. (d) Determination of g2.

where the magnetic rigidity of a particle is expressed as a deviation from the reference trajectory in eq. (2.10), and is related to the required caracteristics of the optics in eq. (2.11). Eq. (2.11) indicates that the position x_2 varies with the magnetic rigidity of the particle when the optics setting is fixed, and is a function of the magnetic field when the magnetic rigidity of the particle is kept constant. The latter case is the principle that was used in practice to evaluate the dispersion D_2 in some calibration runs. With the target off-beam, the primary beam (which, being chosen as a reference, has $B\rho = B\rho_0$) was directed through a magnetic field B^0_{12}, set in order to have $x_2 = 0$ and, as a consequence

$$B\rho_0 = B^0_{12}\rho_0 \quad . \tag{2.12}$$

The magnetic field was than changed of a quantity ΔB_{12}, in order to obtain a position deviation equal to Δx_2, as expressed by the relation

$$B\rho_0 = (B^0_{12} + \Delta B_{12})\rho_0 \left(1 + \frac{\Delta x_2}{D_2}\right) \quad . \tag{2.13}$$

Eliminating $B\rho_0$ in eq. (2.12) and eq. (2.13), we obtain the relation

$$B^0_{12} = (B^0_{12} + \Delta B_{12}) \left(1 + \frac{\Delta x_2}{D_2}\right) \quad , \tag{2.14}$$

that leads to

$$D_2 = -B^0_{12}\frac{\Delta x_2}{\Delta B_{12}} - \Delta x_2 \approx -B^0_{12}\frac{\Delta x_2}{\Delta B_{12}} \quad , \tag{2.15}$$

where the additional term $-\Delta x_2$ was neglected because in our case ΔB_{12} is around two orders of magnitude smaller than B_{12}. In the diagram (b) of fig. 2.3 the experimental measurement of the slope $\Delta x_2/\Delta B_{12}$ is shown. The reference value B^0_{12} could be either measured or extrapolated from the slope itself.

The measurement of the dispersion D_4 was effectuated by centring the primary beam at $x_2 = 0$ and varying the magnetic field B_{34} only. We impose $x_2 = 0$ in eq. (2.9) and apply the same procedure used for D_2 so as to obtain

$$D_4 = -B^0_{34}\frac{\Delta x_4}{\Delta B_{34}} \quad . \tag{2.16}$$

In the diagram (c) of fig. 2.3 the experimental measurement of the slope $\Delta x_4/\Delta B_{34}$ is shown.

The parameter g_2 is deduced from eq. (2.9), that could be written in the form

$$x_4 - g_2 x_2 = \left(\frac{B\rho}{B_{34}\rho_0} - 1\right) D_4 \quad . \tag{2.17}$$

A scaling of B_{12} without any variation of B_{34} and $B\rho$ would keep the second term of eq. (2.17) constant and produce a variation Δx_2 and Δx_4 only. This is what was also done experimentally, still using the primary beam, in order to obtain the simple relation

$$g_2 = \frac{\Delta x_4}{\Delta x_2} \quad . \tag{2.18}$$

2.3 Nuclide identification

One single optic setting of the spectrometer allows for a partial transmission of the p/q distribution of produced fragments. The selected p/q range is of about $\pm 1.5\%$ in the dispersive focal plane. Thus, a limited A/Z range of fragments can traverse the first half of the spectrometer. This imposed to scale the set of magnetic fields several times in order to scan all the distribution of momenta (and therefore of masses) of the reaction products.

When the layers of matter present in the dispersive-focal-plane region have a non-negligible thickness, the fragments lose part of their kinetic energy as a function of Z^2, and both the momenta and the magnetic rigidities change. Such an effect results in an additional selection in the second half of the spectrometer, limiting the passage of the fragments to a restricted range of charges. In certain conditions, the selection of a limited Z-range is desirable, as it allows to measure separately elements with low yields and with high yields, respectively. In the measurement with ^{136}Xe projectiles

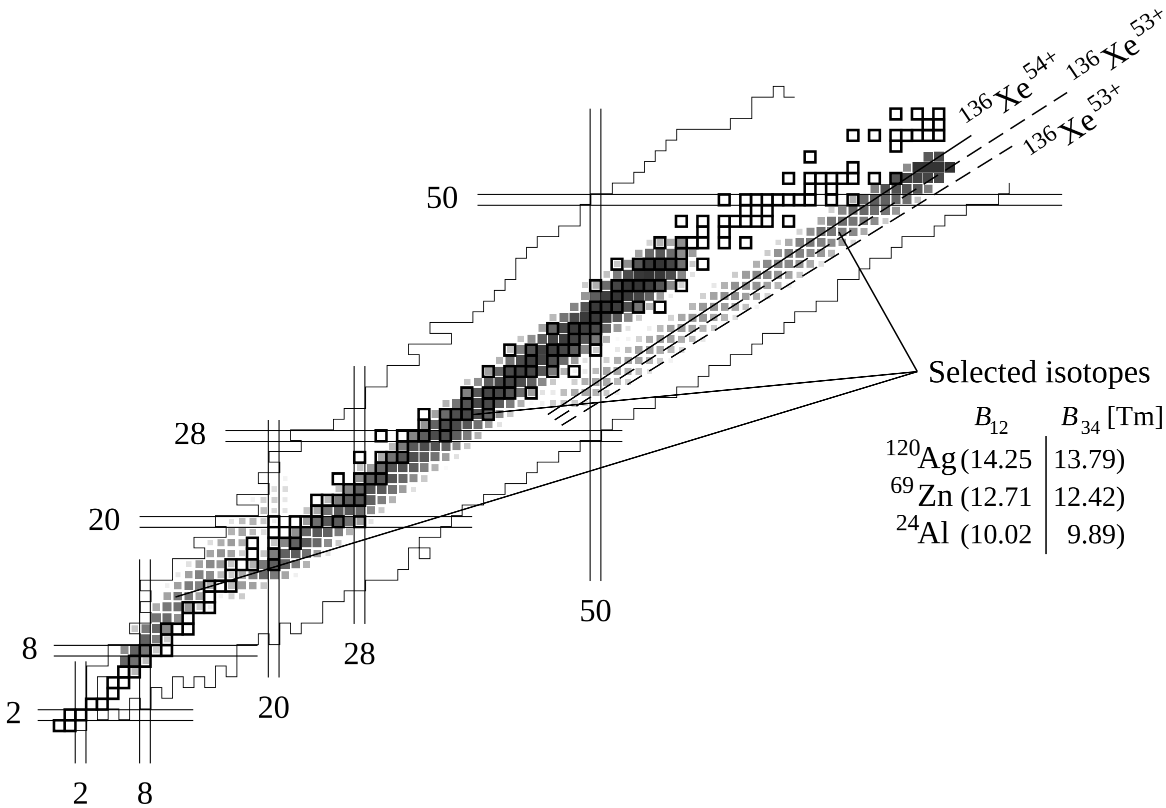

Figure 2.4: Expected counting rate for a group of isotopes selected by three different magnetic settings. In the table the corresponding central isotopes and magnetic fields are indicated. For the calculation the ion-optic code Lieshen was used[Schmidt 1987, Hanelt 1992]. The calculation neglects the light isotopes.

an additional layer of matter was positioned behind the scintillator in the dispersive-focal-plane area [1], in order to measure the isotopic production along three bands centred around Ag, Zn and Al, respectively. Compared to heavy nuclides and light fragments, the Zn-band corresponded to a low-yield region and it required to be measured separately. The simultaneous measurement of the intermediate-Z band and heavy-Z band would have severely spoiled the statistics of the former band. In fig. 2.4 the expected measurable isotopic production associated to three settings with ^{136}Xe projectiles is shown, as estimated before the experiment by the use on an ion-optical calculation. The projectile and its one-electron and two-electron charge states (unfortunately, non completely stripped ions are always present in the primary beam) are not products of the nuclear reaction and induce a huge counting rate: they saturate the data acquisition and might damage the detectors. It is therefore necessary to select out the corresponding p/q by employing specific slits in the focal plane 1 (see fig. 2.1). In fig. 2.4 three lines mark the isotopes with magnetic rigidity close to the projectile (solid line) and to the one-electron and two-electron charge states of ^{136}Xe (dashed line). The momentum distribution of these isotopes could not be measured completely. For the settings dedicated to the ^{56}Fe projectiles no degrader was used, and all the produced elements with a given p/q were measured at once.

2.3.1 Charge and Time of flight

The time of flight was measured by the scintillators installed in the dispersive focal plane and in the achromatic focal plane, as the time interval needed by a particle to fly along the path $\ell \approx 36m$ from one focal plane to the other. Technically, the measurement starts with the detection in the achromatic plane, while the corresponding signal coming from the scintillator placed in the dispersive focal plane is delayed and used to stop the acquisition. This is a solution to disregard the particles lost in the second half of the spectrometer and reduce the dead-time considerably.

The particle charge was measured by one (with ^{56}Fe beam) or two (with ^{136}Xe beam) ionization chambers placed in front of the achromatic plane. They were filled with a mixture of Ar (90%) and CH_4 (10%) at room temperature and about normal pressure. When traversed by an ionising particle, the gas generates a cloud of electrons and ions around the trajectory, and four anodes produce a signal proportional to the number of stripped electrons collected. At incident energies of around 1 A GeV, the energy lost by a projectile traversing a layer of matter is described by the Bethe-Bloch equation. Therefore, in an ideal case, the signal of the ionization chambers should be about proportional to the ratio q^2/β^2. Technically, there is one complication. The stripped electrons, falling towards the anodes, could be captured by gas molecules. This recombination effect increases with the electron path length. Since the anodes are positioned on the horizontal beam-plane on one side of the detector,

[1] An aluminum degrader constituted of rotating-wedges was used, with a thickness of 816.6 mg/cm^2

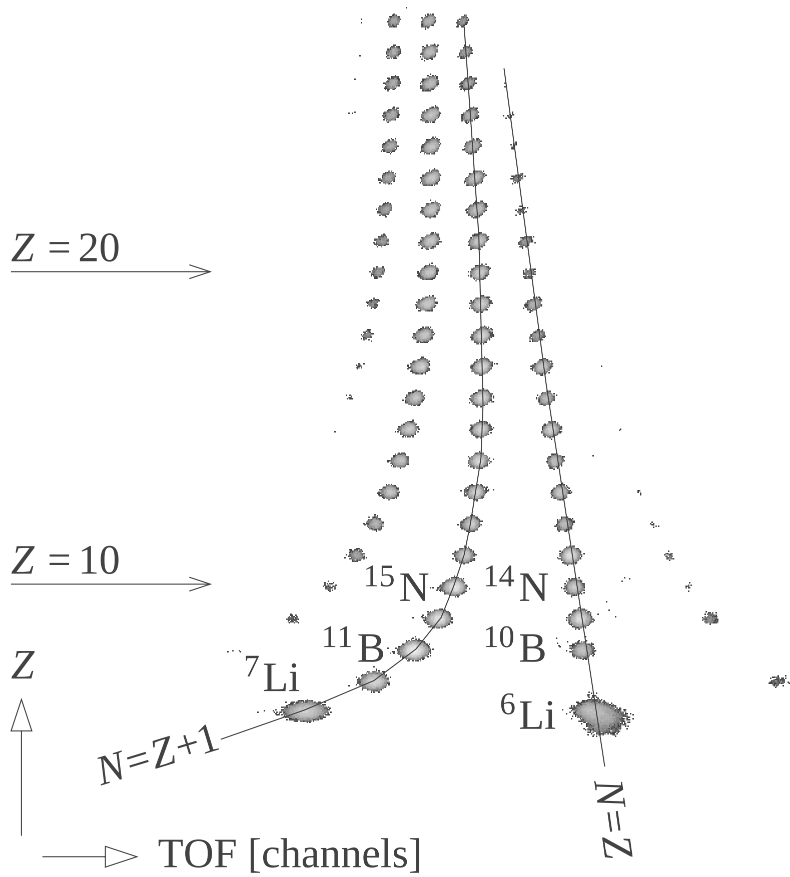

Figure 2.5: Identification plot of fragments measured with a ^{136}Xe beam.

the measurement of the energy loss of a particle is slightly affected by a dependence $f(x_4)$ on the position x_4 in the achromatic focal plane. The β^2-dependence of the signal can be reduced to a function of the measured time of flight $g(TOF)$. Since the reaction products were fully stripped, the nuclear charge $Z = q$ was deduced directly, after eliminating the dependence on the position $f(x_4)$ and on the velocity $g(TOF)$. In fig. 2.5 the nuclear charge measured by the ionization chambers is represented as a function of the measured time of flight for one magnetic setting of the spectrometer dedicated to register light fragment of a ^{136}Xe projectile. The cloud of event concentrates in clusters, each one corresponding to a single fragment (A, Z). The effect of "clustering", so helpful for the data analysis, is a consequence of the limited magnetic-rigidity acceptance of the FRagment Separator. Since for an isotope the accepted velocity spread is very narrow, the Z^2 dependence is dominant in the measurement of the energy loss ΔE. Moreover, for the same reason, $\beta\gamma$ (whose expression is $\beta\gamma \propto B\rho\frac{Z}{A}$) depends strongly on the mass A; as a consequence, the same dependence will characterize the time of flight. If the magnetic-strength acceptance were wider, the $MUSIC$-time of flight plot would be confused and the cluster structures would vanish.

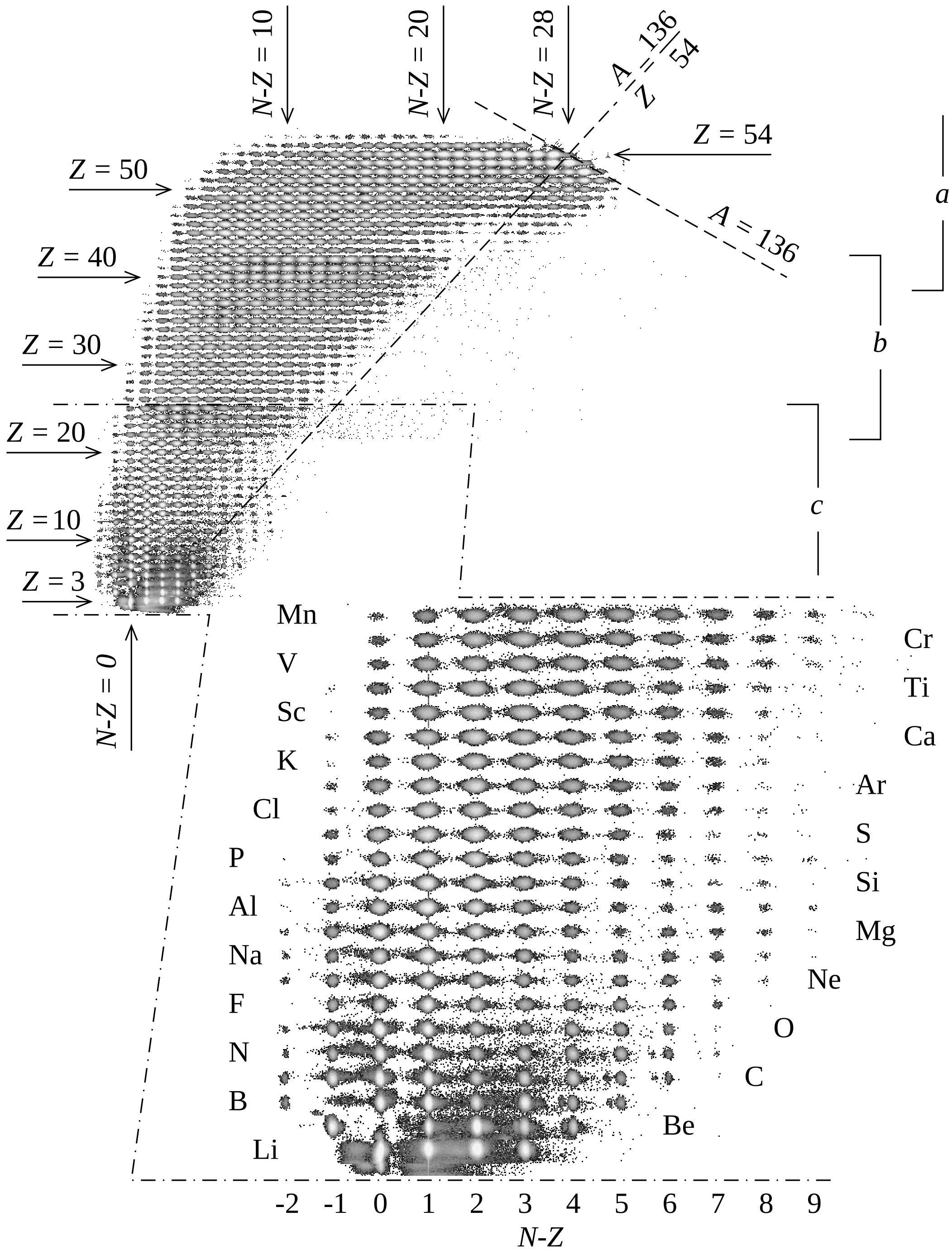

Figure 2.6: Composition of all identified events measured with a ^{136}Xe beam at 1 A GeV. Three overlapping bands a, b and c correspond to the three groups of magnetic settings for the central isotopes ^{120}Ag, ^{69}Zn, ^{24}Al, respectively. The band c, collecting light nuclides, is enlarged in order to show the isotopic resolution.

2.3.2 Mass separation

The mass A was deduced from the time of flight and the magnetic rigidity of the particles according to the relation

$$\frac{A}{Z} = \frac{1}{\mathrm{c}} \cdot \frac{\mathrm{e}}{\mathrm{m}_0 + \delta m} \cdot \frac{B\rho}{\beta\gamma(\mathrm{TOF})} \quad , \tag{2.19}$$

where $B\rho$ is the magnetic rigidity of a particle, c the velocity of light, e the elementary charge, m_0 the nuclear mass unit, $\delta m = \mathrm{d}M/A$ the mass excess per nucleon. For the purpose of the isotopic identification, the variation of δm with A/Z can be neglected, and a linear variation of A/Z as a function of $B\rho/\beta\gamma$ can be assumed. In eq. (2.19) the quantity $\beta\gamma(TOF)$, or rather β, is not deduced directly from the TOF measurement. A set of eight coefficients $\vec{k} = (k_1, \ldots, k_8)$, constant for all the runs was searched for, in order to write the path length ℓ as:

$$\ell = l + k_1 x_{S_2} + k_2 x_{S_4} \quad ,$$

(Where $l = 36m$ is the average path length.) and the time of flight as:

$$t = k_3 + k_4 TOF + k_5 x_2^2 + k_6 x_4^2 + k_7 e^{-k_8 Z^2} \quad , \tag{2.20}$$

where quadratic terms in x_2 and x_4 describe non-linear effects of the light-propagation time; A Z-dependent term is added to take into account the remaining walk dependence of the discriminators (i.e an amplitude dependence). Thus, the relative velocity is the ratio:

$$\beta = \frac{\ell}{ct} \quad . \tag{2.21}$$

The terms $\vec{k}$ are then deduced by numerical optimization and used for the whole data analysis (as far as the characteristics of the detectors were unchanged). In fig. 2.6 the raw data collecting all the events measured in the experiment with a ^{136}Xe projectile are shown. Events are ordered according to the measured Z and $N - Z$ so as to obtain an isotopic identification plot.

2.4 Longitudinal velocities

The measurement of the time of flight is precise enough for an accurate identification of the mass of the fragments. Nevertheless, mainly due to the resolution and additionally due to a slight dependence on the trajectory [Napolitani 2001a] it is not suited for a fine measurement of the velocities of the fragments. On the other hand, once an isotope is identified in mass and charge, a much more precise measurement of the velocity is obtained directly from the magnetic rigidity of the particle

$$\beta\gamma = B\rho \cdot \frac{1}{\mathrm{c}} \cdot \frac{\mathrm{e}}{\mathrm{m}_0 + \delta m} \cdot \frac{Z}{A}; \quad . \tag{2.22}$$

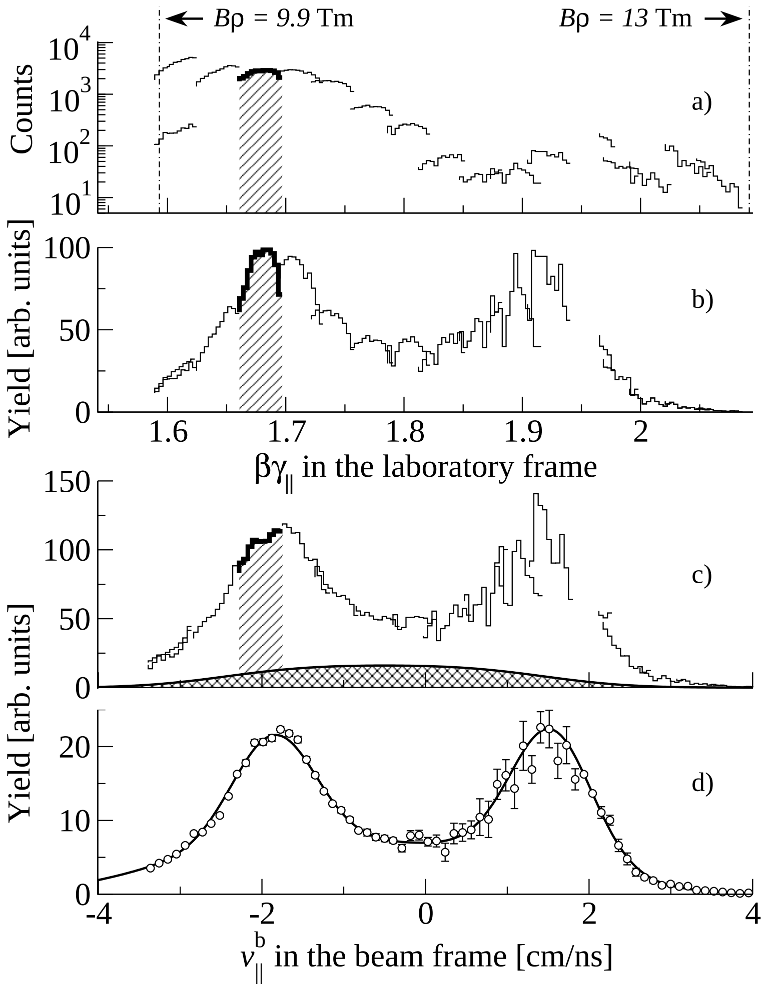

Figure 2.7: Four steps of the analysis procedure to obtain the observed velocity spectrum of ^{6}Li emitted in the reaction ^{56}Fe+p. (a) Raw spectra of counts as a function of $\beta\gamma$ in the laboratory frame. Each segment results from a different scaling of the magnetic fields of the FRS. One segment associated to the same magnetic scaling is marked with hatched areas in this plot and in the two following ones. Arrows delimit the scanned $\beta\gamma$ range. (b) Yields normalized to the same beam dose. (c) Elimination of the angular-transmission distortion. Spectrum as a function of the longitudinal velocity in the beam frame $v_{\|}^{b}$. The broad Gaussian-like hatched area indicates the contributions from non-hydrogen nuclei. (d) All components of the spectrum are composed together averaging overlapping points. Contributions from non-hydrogen-nuclei were suppressed. The spectrum was divided by the number of nuclei per area of the liquid-hydrogen target. Statistical uncertainties and a fit to the data are shown.

In this case, the precision of $\beta\gamma$ depends only on $B\rho$, that has a relative uncertainty of $5 \cdot 10^{-4}$ (FWHM) for individual reaction products. The absolute calibration of the deflection in the magnet in terms of magnetic rigidity $B\rho$ was performed at the beginning of the experiment with a dedicated calibration run using the primary beam as detailed above. $B\rho$ is the magnetic rigidity of the fragments in the first half of the spectrometer, before the dispersive focal plane as calculated accordig to eq. (2.11).

Since one single magnetic configuration of the FRS selects only a $B\rho$ range of about $\pm$ 1.5%, several overlapping runs have been repeated imposing different magnetic fields. While for the heavy residues close to the projectile one or few settings were sufficient to cover the whole velocity spectrum, the light fragments often required more than ten runs. The $B\rho$ scanning of ^{6}Li, produced in the interaction of ^{56}Fe with the target of liquid hydrogen enclosed in the cryostat constitutes the diagram (a) of fig. 2.7: each segment of the spectrum is obtained from a different scaling of the set of magnetic fields of the FRS. In order to obtain consistent weightings, the counts of the different measurements were normalized to the same beam dose. For each magnetic scaling, this normalization was obtained by dividing the corresponding segment of the spectrum by the number of projectiles that hit the target during the corresponding run. The impinging projectiles were counted with the beam-current monitor. The renormalized yields are shown in the diagram (b) of fig. 2.7. We should note that the spectrometer accepts only the fragments emitted in a cone of about 15 mr around the beam-axis in the laboratory frame, when the reaction occurs in the hydrogen-target position. As a consequence, a light residue like, for example, ^{6}Li, generated in a collision at a beam energy of 1 A GeV can be detected only if emitted with small transverse momentum. The experimental spectrum represents the part of the density distribution in the velocity space selected by the angular acceptance of the spectrometer, projected on the longitudinal axis. Unfortunately, the angular acceptance depends on the magnetic rigidity of the particles. As pointed out in the work [Benlliure 2002], for a given set-up of the spectrometer, the more the intersection of the trajectory of a particle with the dispersive or the achromatic planes is displaced from the centres, the lower is the acceptance angle of the FRS. The effect appears in the curved sides of each single segment, with the result of disturbing the overall structure of the $B\rho$ scanning. This distortion, seen in the spectrum of the plot (b) of fig. 2.7, can be successfully corrected by means of ion-optical calculations that fix the dependence of the angular transmission on the trajectory. The calculation of the ratio of the transmission T relative to its maximum value is presented in fig. 2.8. The corrected spectrum, seen in the plot (c) of fig. 2.7, is the result of scaling up the yields of the spectrum by the factor T_{max}/T. We also changed from a $\beta\gamma$ spectrum to a longitudinal-velocity spectrum and, to simplify the analysis, the reference frame was changed from the laboratory to the beam frame. On the average, the projectile interacts in the middle of the target. Therefore, we take into account the slowing down of ^{56}Fe in the first half of the target, as represented in the upper diagram of fig. 2.9. We also consider that the fragments slowed down in the remaining half of the target and, therefore, were emitted at higher velocity than the one we observed. The analysis so far illustrated was repeated for all the isotopes produced in the interaction with the target of liquid hydrogen enclosed in the cryostat. Successively, the same procedure was applied to the corresponding isotopes produced in the interaction with the ^{nat}Ti target. As all spectra are normalized to the same beam dose, by subtracting the velocity spectra of the residues produced in ^{56}Fe+^{nat}Ti (indicated by the hatched area in the plot (c) of fig. 2.7) from those of the corresponding isotopes produced in the target of hydrogen stored in the cryostat, we could obtain the measured velocity distributions for the reaction with the liquid hydrogen. The resulting yields are unambiguously disentangled from any disturbing contributions produced by other material present in the target area. Finally, the velocity spectra obtained for the ^{56}Fe+p system were divided by the number of nuclei per area of the proton target. The resulting spectrum is shown in the diagram (d) of fig. 2.7. In the case of the ^{56}Fe+^{nat}Ti and ^{136}Xe+^{nat}Ti systems, we should consider that the target is constituted of three components, the titanium foils replacing the cryostat, the beam-current monitor and the accelerator-vacuum window, having a number of nuclei per area equal to n_0, n_1, and n_2, respectively. We should also recall that these components are placed at different distances from the entrance of the spectrometer and are subjected to different values of the angular acceptance, that is about $\alpha_0 = 15.8$ mr, $\alpha_1 = 9$ mr, and $\alpha_2 = 7.8$ mr, for the layers n_0, n_1, and n_2, respectively. Thus, the cross sections given in this work for the "titanium" target are calculated using a target composition where the different layers are weighted by the corresponding estimated transmission values T, assuming identical production cross sections in the different target components. In particular, the velocity spectra obtained for the ^{56}Fe+^{nat}Ti and ^{136}Xe+^{nat}Ti systems should be divided by the quantity $n_0 T(\alpha_0) + n_1 T(\alpha_1) + n_2 T(\alpha_2)$.

The experimental data are already complete enough to let us recognise an important signature of the Coulomb repulsion: the double-humped spectrum reveals that the velocity of ^{6}Li nuclei emitted at small angles has two components: one appre-

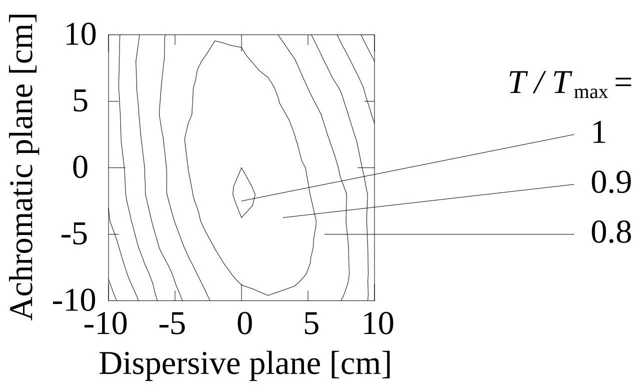

Figure 2.8: Transmission of the FRS as a function of the positions in the dispersive and achromatic planes, relative to its maximum value. Numerical values are taken from ref. [Benlliure 2002].

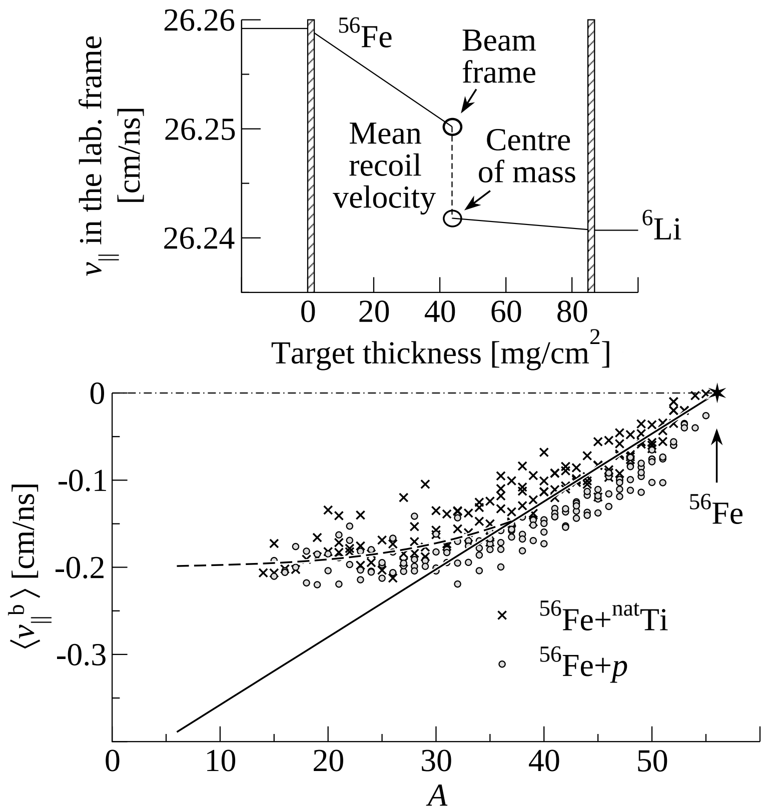

Figure 2.9: *Top.* Definition of the beam frame and of the centre-of-mass frame of the emitting source with respect to the laboratory frame. The diagram corresponds to realistic conditions of the present experiment for ^{6}Li. The solid lines describe the slowing down of the beam and of the centroid of the velocity spectrum of ^{6}Li in traversing the target. *Bottom.* Mean longitudinal recoil velocities in the beam frame $< v_{||}^{b} >$ of the reaction residues compared with the systematics of Morrissey [Morrissey 1989] (solid line); only isotopes with sufficient statistics and entirely measured velocity spectra are considered.

ciably higher and one appreciably lower than the beam. According to the references [Benlliure 2001, Enqvist 2001b, Bernas 2002], where similar structures have been observed for fission fragments, we may connect the double-humped spectrum to the action of the Coulomb field of a heavy partner in the emission process.

Once changed to longitudinal velocities in the beam-frame $v_{||}^{b}$, the shift of the barycentre of the spectrum with respect to zero is equal to the mean reaction recoil $< v_{||}^{b} >$. Also this quantity, studied in the lower diagram of fig. 2.9, carries a valuable information about the reaction mechanism, and it can be related to the friction suffered by the projectile in the collision, according to a given impact parameter [Morrissey 1989]. Due to the limited angular acceptance of the FRS which favours the detection of heavier nuclei, a depletion of the statistics for the measurement of the lightest nuclei is expected when, as in the measurement with the ^{56}Fe beam, the light fragments are measured together with the heaviest in the same magnetic setting. Due to these problems, the mean velocities of the light residues can only be determined with relatively large uncertainties. With these large uncertainties, the information from the mean velocities could not be exploited. Although these mean velocities also enter into the evaluation of the cross sections, the uncertainties they introduce are comparable to those from other sources. It is therefore preferable to deduce the mean recoil velocities of lithium, beryllium, boron and carbon by extrapolation from the systematics of the data relative to the ensemble of the heavier residues.

2.5 Normalization to the beam dose

2.5.1 Beam-current monitor

A beam-current monitor was installed in front of the target. it was composed of three metal foils perpendicular to the beam, the external one constituting the anode, and the middle foil working as the cathode. Electrons, originating from the cathode are collected by the anode; since any significant space-charge effect has been observed, the secondary-electron current measured on the middle foil is assumed to be proportional to the primary-beam current. The device is named SEcondary Electron TRAnsmission Monitor [Junghans 1996, Jurado 2002] (SEETRAM). The advantage with respect to using a scintillator is the efficiency in measuring high primary-beam currents and a smaller thickness. A scintillator would seriously deteriorate the beam quality due to its thickness, comparable to an additional target.

The counting rate can be obtained calibrating the secondary-electron current respect to the primary-beam current; since the output signal of the SEETRAM is turned into a voltage and then digitalized, the calibration resolves into the ratio:

$$\kappa_{\text{seetram}} = \frac{\text{secondary-electron current}}{\text{primary-beam current}} = \frac{\text{SEETRAM counts}}{\text{number of impinging projectiles}} \quad .$$

In order to obtain the impinging-projectile counting, a scintillator is inserted in the beam between the SEEETRAM and the target during a calibration procedure, and is then removed during the experiment. The figure 2.10 shows a comparison between the time evolution of particle counts measured with the scintillator and the corresponding SEETRAM counts during a calibration run aimed to measure the parameter κ_{seetram}. The SEETRAM reproduces properly the beam structure, with the only addition of an offset, due to a current added at the output of the digitalizer. The signal produced by the middle foil is in fact firstly turned into a voltage, filtered, and finally digitalized. For very low signals the filter could generate some fluctuations around zero and the signal could drop to negative values: in this case the output current of the digitaliser could be interrupted. In order to have an always-positive signal the addition of a constant positive offset is necessary.

Before integrating the SEETRAM counts for each spill, this offset should be accurately subtracted. After this operation, the number of particles constituting each spill (measured with the scintillator) can be ordered as a function of the corresponding SEETRAM counts as in the insert in fig. 2.10.

The quadratic dependence of the particle counting as a function of the beam intensity reveals a saturation [Jurado 2002] of the scintillator: as a consequence, we assume more significant the region of the curve corresponding to low counts, and we obtain the calibration coefficient as the initial slope of the quadratic fit of the function.

The number of projectiles can be measured for each run by subtracting the offset

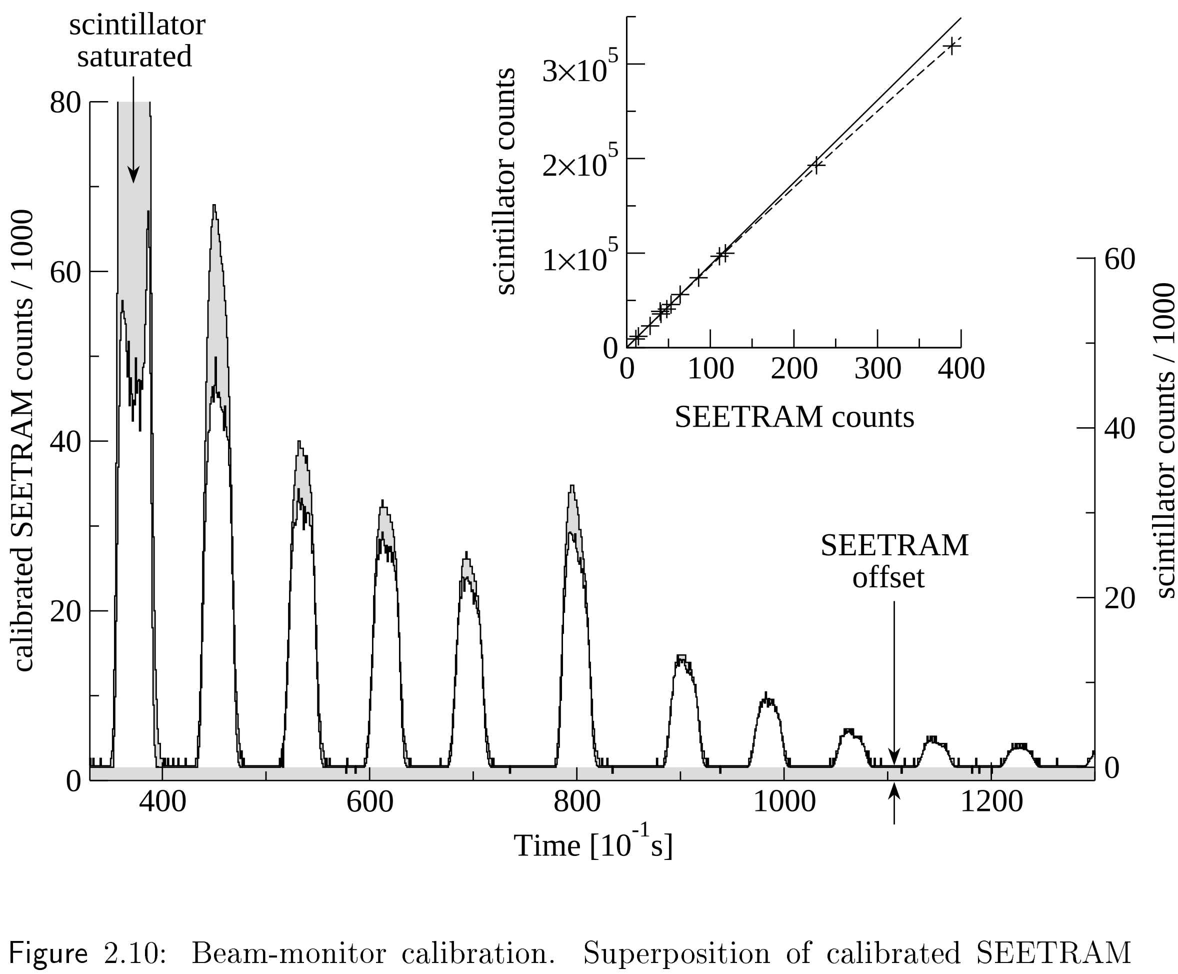

Figure 2.10: Beam-monitor calibration. Superposition of calibrated SEETRAM counts (grey-filled spectrum, axis label on the left) and scintillator counts (white-filled spectrum, axis label on the right). The SEETRAM spectrum is rescaled of its offset and multiplied by the parameter $\kappa_{\mathrm{seetram}}$, that coincides with the calibration slope shown in the insert.

from the corresponding SEETRAM counting and multiplying the resulting difference for the calibration coefficient.

$$N_{\text{projectiles}} = \kappa_{\text{seetram}}(\text{SEETRAM} - \text{offset}) \quad .$$

2.5.2 Total number of fragments traversing the spectrometer

The row-data plot of fig. 2.6 collects the number N_{measured} of particles detected by the scintillator in the achromatic focal plane and not the real number N of fragments that traversed the separator. A specific acquisition device counts independently all the particles N crossing the separator, even if they do not correspond to a measured event (i.e. an event is characterized by the registration of all identification parameters). The dead-time may be defined as

$$\tau = \frac{N - N_{\text{measured}}}{N} \quad .$$

Finally, in order to obtain normalized yields to the beam dose from the measured yiels it is necessary to divide them by the number of impinging projectiles and by the events-to-detected-particle ratio:

$$\text{Normalized yields} = \frac{\text{measured yields}}{N_{\text{projectiles}}(1 - \tau)} \quad .$$

It should be observed that the normalized yields do still not correspond to cross sections, as we are still disregarding the portion of fragments emitted outside of the solid angle defined by the angular acceptance of the spectrometer.

Chapter 3

Results

Contents

3.1 Velocities **34**

3.2 Nuclide cross section **43**

3.1 Velocities

When a fragment is emitted with a large absolute velocity $v = |\vec{v}|$ in the centre of mass, not all the angles of the corresponding velocity vector $\vec{v}$ are selected by the finite angular acceptance of the spectrometer. As a result of the data analysis detailed in the previous section, we obtain the measurement of the apparent cross section $\mathrm{d}\mathcal{I}(v_{||})/\mathrm{d}v_{||}$ as a function of the longitudinal velocity $v_{||}$. This observed cross section differs from the real cross section due to the angular acceptance. The detection of a particle depends on the perpendicular velocity $v_\perp = \sqrt{v^2 - v_{||}^2}$ in the centre-of-mass frame, the angle of rotation around the beam direction φ, and the velocity u of the centre of mass with respect to the laboratory. The dependence on φ comes about because the beam pipe inside the quadrupoles is not cylindrical. A diagram constructed on the basis of experimental data is presented in fig. 3.1, to detail the geometry of the spectrometer acceptance.

We intend to extract data on the fragment-emission kinematics and eliminate any dependence on the experimental device. For this purpose, we need to search for a connection between the cross-section variation in velocity space in the centre-of-mass frame and the measured spectra $\mathrm{d}\mathcal{I}(v_{||})/\mathrm{d}v_{||}$ as a function of the longitudinal velocity component $v_{||}$ in the centre-of-mass frame. In a general case, the former distribution is not isotropic, but a function of the absolute velocity v, the polar angle from the beam direction θ, and the azimuthal angle around the beam axis φ. It will be denoted as $\mathrm{d}^3\sigma/(\mathrm{d}v\,\mathrm{d}\Omega)$, where Ω is the solid angle. The velocity component orthogonal to the beam axis is $v_\perp$. The contribution to the experimental yield in the interval $[v_{||}, v_{||} + \Delta v_{||}]$ is obtained by integrating $v_\perp$ in the slab orthogonal to the beam axis :

$$\begin{aligned} \frac{\mathrm{d}\mathcal{I}(v_{||})}{\mathrm{d}v_{||}} &= \iint \frac{\mathrm{d}^3\sigma}{\mathrm{d}\vec{v}}\, v_\perp\, \mathrm{d}v_\perp\, \mathrm{d}\varphi \\ &= \iint \frac{1}{v^2}\frac{\mathrm{d}^3\sigma}{\mathrm{d}v\,\mathrm{d}\Omega}\, v_\perp\, \mathrm{d}v_\perp\, \mathrm{d}\varphi \quad . \end{aligned} \tag{3.1}$$

For the orthogonal velocity integration the lower limit is 0 and the higher limit is related to the angular acceptance of the spectrometer. Since the latter is not necessarily circular, it can depend on φ and will be denoted as $\alpha(\varphi)$. The maximal orthogonal velocity may be derived from the Lorentz transformation of the momentum and it reads : $\widetilde{v}_\perp(\varphi) = \gamma(u + v_{||})\alpha(\varphi)$, where u and γ are the velocity and the Lorentz factor of the center of mass in the laboratory frame, respectively. Introducing these limits in the integration we write :

$$\frac{\mathrm{d}\mathcal{I}(v_{||})}{\mathrm{d}v_{||}} = \int_0^{2\pi} \left[\int_0^{\widetilde{v}_\perp(\varphi)} \frac{1}{v^2}\frac{\mathrm{d}^3\sigma}{\mathrm{d}v\,\mathrm{d}\Omega}\, v_\perp\, \mathrm{d}v_\perp \right] \mathrm{d}\varphi \quad . \tag{3.2}$$

Changing the integration variable from $v_\perp$ to $v = \sqrt{v_\|^2 + v_\perp^2}$ we obtain :

$$\frac{\mathrm{d}\mathcal{I}(v_\|)}{\mathrm{d}v_\|} = \int_0^{2\pi} \left[\int_{|v_\||}^{\sqrt{v_\|^2+\tilde{v}_\perp^2(\varphi)}} \frac{1}{v} \frac{\mathrm{d}^3\sigma}{\mathrm{d}v\,\mathrm{d}\Omega} \mathrm{d}v \right] \mathrm{d}\varphi \quad . \tag{3.3}$$

To reconstruct the full velocity distribution, independent of the angular acceptance of the spectrometer, an assumption on the angular distribution is necessary. It was concluded from experiments, to which the full angular range was accessible, that the

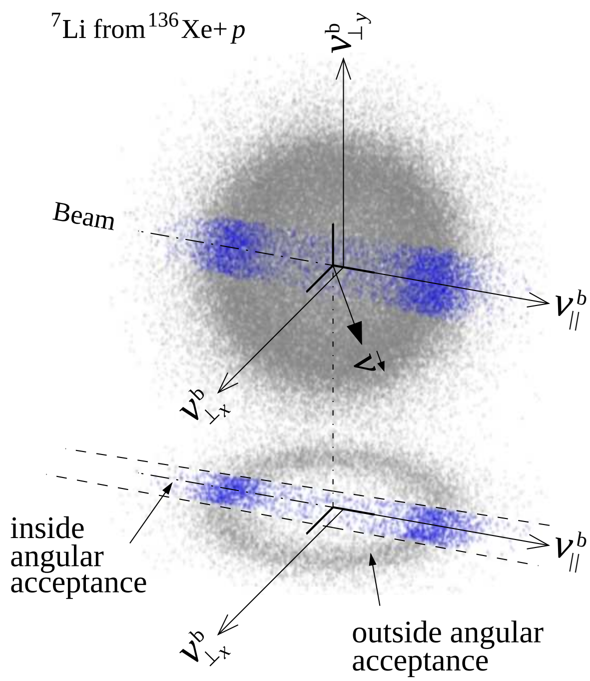

Figure 3.1: Statistics of velocity vectors $\vec{v}$ of ^{7}Li, emitted in the fragmentation of a ^{136}Xe beam, reconstructed on the basis of the longitudinal velocities, measured experimentally. The velocity coordinates of the beam frame are shown (observe the back-shift of the centre of mass, origin of the vector $\vec{v}$, with respect to the origin of the beam frame coordinates). The black dots are the velocity vectors accepted by the spectrometer. The gray dots indicate the particles that are not transmitted through the angular acceptance. A cut for $v_\perp = 0$ is shown in the bottom. The cut, in the shape of a ring, reveals that the emission corresponds to a shell in velocity space and reveals a Coulomb hole. The dashed lines delimit the region accepted by the spectrometer and reveal that, for this specific ejectile, only a forward portion and a backward portion of the emission shell can be measured.

data are in satisfactory agreement with an isotropic emission (see, for example, the treatment of "Moving source analysis" presented in [Korteling 1990]). This assumption has been corroborated by a vast collection of data for reactions of very different nature. Isotropic emission has been observed either for lowly excited fissioning systems [Moretto 1989], or even for very highly excited nuclei undergoing expansion flow in thermal multifragmentation [Karnaukhov 1999, Karnaukhov 2003a]. At least the ^{56}Fe+p and ^{136}Xe+p systems can be safely included in this range. Slightly less justified is the assumption for ^{56}Fe+^{nat}Ti and ^{136}Xe+^{nat}Ti , since some effects of dynamical multifragmentation could disturb the isotropy. Thus, if we assume isotropic particle emission in the centre-of-mass frame, $\mathrm{d}^3\sigma/(\mathrm{d}v\,\mathrm{d}\Omega)$ reduces to $(1/4\pi)(\mathrm{d}\sigma/\mathrm{d}v)$ and the variation of the cross section $\sigma(v)$, as a function of the absolute velocity v, is related to the variation of the apparent cross section $\mathcal{I}(v_\|)$ as a function of $v_\|$ by the equation:

$$\frac{\mathrm{d}\mathcal{I}(v_\|)}{\mathrm{d}v_\|} = \frac{1}{4\pi}\int_0^{2\pi} \mathrm{d}\varphi \int_{|v_\||}^{\sqrt{v_\|^2+\tilde{v}_\perp^2(\varphi)}} \frac{1}{v}\frac{\mathrm{d}\sigma(v)}{\mathrm{d}v}\,\mathrm{d}v \quad , \tag{3.4}$$

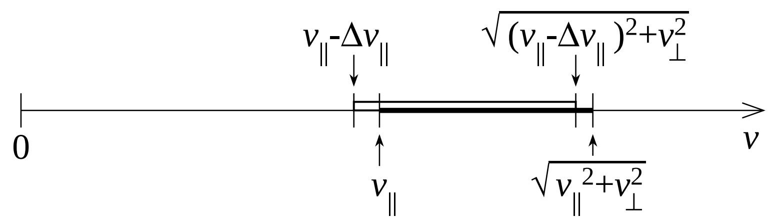

Figure 3.2: Integration domains of eq. (3.4).

In equation (3.4), the term $\mathrm{d}\sigma/\mathrm{d}v$ is the physical quantity that we wish to extract. It describes the variation of the cross section $\sigma(v)$ as a function of the absolute velocity v in the centre-of-mass frame The measured quantity is the left-hand term $\mathrm{d}\mathcal{I}(v_\|)/\mathrm{d}v_\|$, representing the variation of the apparent cross section as a function of the longitudinal velocity component $v_\|$ in the centre-of-mass frame. In principle, equation (3.4) could not be inverted in an unambiguous way for general shapes of the $\mathrm{d}\sigma/\mathrm{d}v$ function. However, for the restricted shapes describing the data, this inversion becomes possible. This is particularly the case if this function is supposed to decrease monotonically to 0 at large v and if $\mathrm{d}\mathcal{I}(v_\|)/\mathrm{d}v_\|$ also follows the same behavior at large $|v_\||$, as it is evident from fig. 2.7.

In order to describe the inversion procedure, let us consider a given bin in longitudinal velocity defined by the interval $[v_\|, v_\| + \Delta v_\|]$. The yield for this bin is $(\mathrm{d}\mathcal{I}(v_\|)/\mathrm{d}v_\|)/\Delta v_\|$, while the corresponding integral over v in equation (3.4) extends from $v_\|$ to $\sqrt{v_\|^2 + v_\perp^2}$. This domain is depicted by the thick segment in fig. 3.2. Let us assume that the values of the function $\mathrm{d}\sigma/\mathrm{d}v$ are known over this interval and that they comply to equation (3.4).

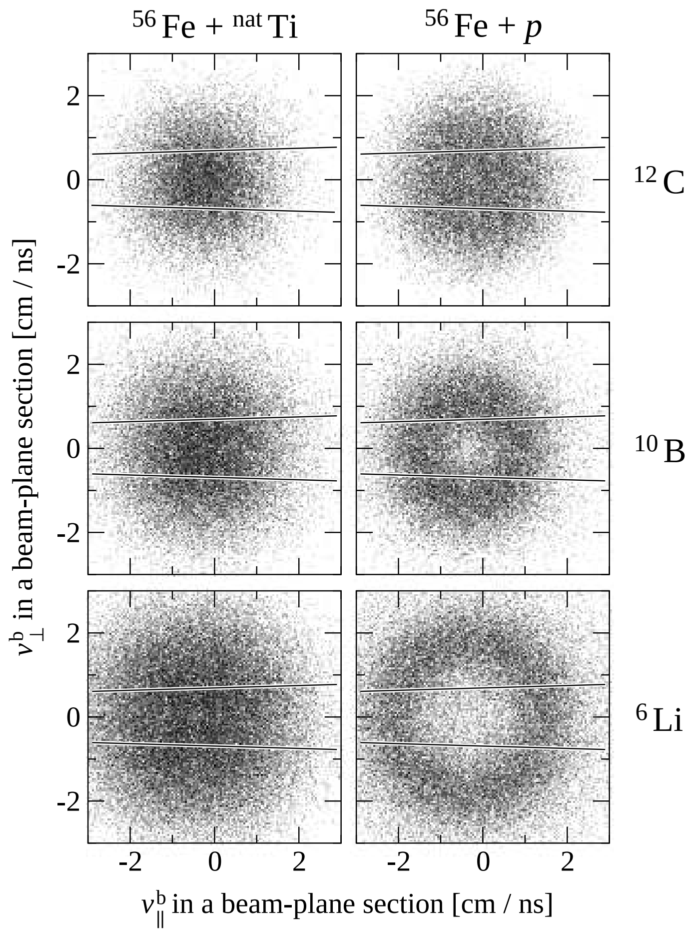

Figure 3.3: Reconstructed density plots in velocity space in the beam frame $(v_{\|}^{b}, v_{\perp}^{b})$ representing the distribution on a plane containing the beam axis. The solid lines denote the angular acceptance of the spectrometer.

We consider now the $v_{\|}$ bin located between $v_{\|} - \Delta v_{\|}$ and $v_{\|}$, for which the integration extends from $v_{\|} - \Delta v_{\|}$ to $\sqrt{(v_{\|} - \Delta v_{\|})^2 + v_{\perp}^2}$, as shown by the thin segment above the axis in fig. 3.2. It can be seen that, if $\Delta v_{\|}$ is small enough, this segment has a large overlap with the previous one. If this were not the case, the inversion procedure would even be simplified as $\mathrm{d}\sigma/\mathrm{d}v$ would be directly proportional to the yield divided by the interval length, provided that the yield has a low variation over $\Delta v_{\|}$. In the case of overlap of the two integration segments, as shown in the figure, the variation of the yield comes only from the values of $\mathrm{d}\sigma/\mathrm{d}v$ at the edges. If the value is known on the right non-overlapping extremity, the variation between the two adjacent $v_{\|}$ bins delivers the value on the left non-overlapping extremity. The procedure can be continued for lower $v_{\|}$ bins, fixing the values of the function for decreasing values of v.

So far, no specific assumption has been made except that the function $\mathrm{d}\sigma/\mathrm{d}v$ is known over a given interval. This can be practically achieved by assuming that

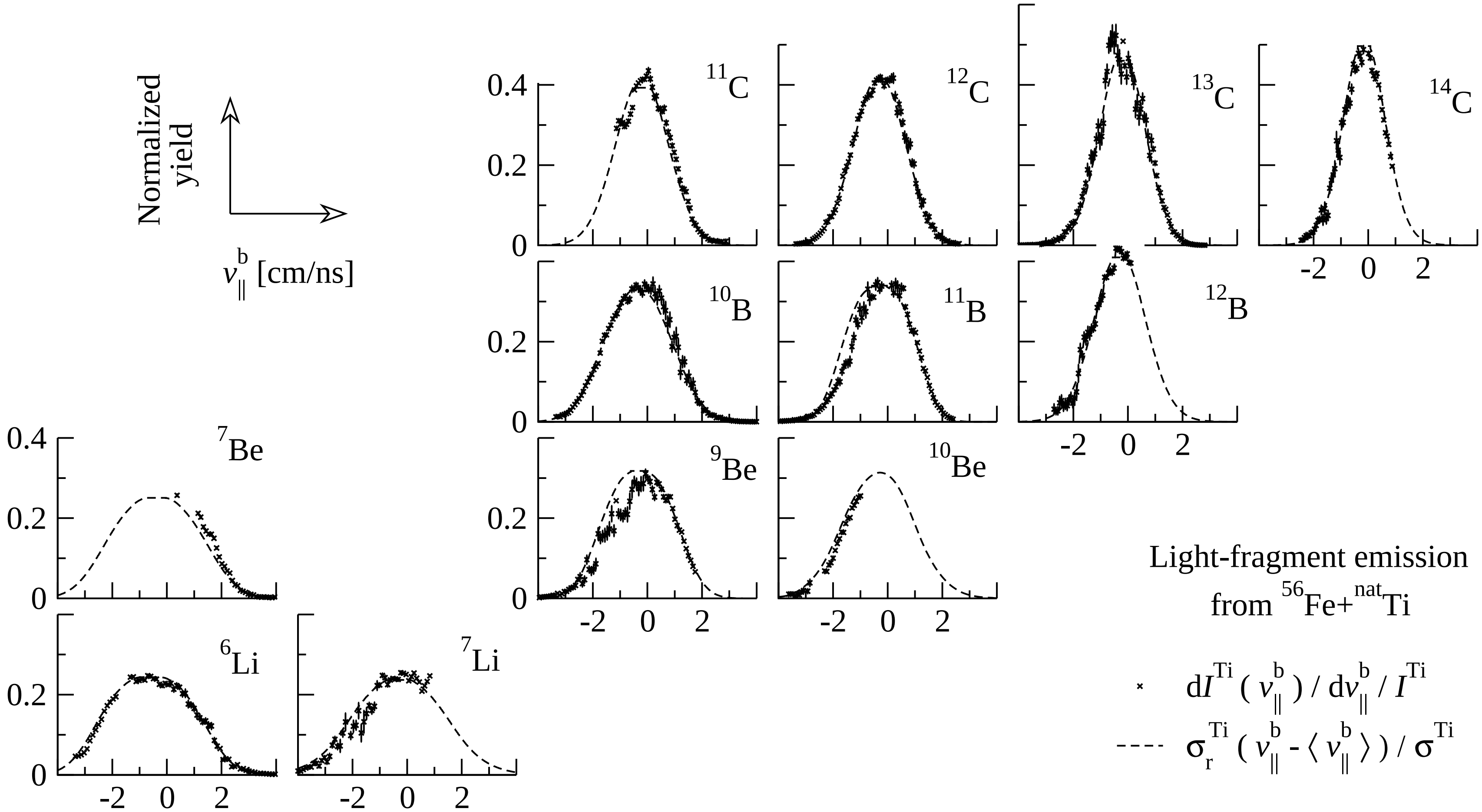
Normalized yield
$v_{\parallel}^{b}$ [cm/ns]
^{11}C
^{12}C
^{13}C
^{14}C
^{10}B
^{11}B
^{12}B
^{7}Be
^{9}Be
^{10}Be
^{6}Li
^{7}Li
0
0.2
0.4
-2
2
Light-fragment emission from ^{56}Fe+^{nat}Ti
$dI^{Ti}(v_{\parallel}^{b}) / dv_{\parallel}^{b} / I^{Ti}$
$\sigma_{r}^{Ti}(v_{\parallel}^{b} - \langle v_{\parallel}^{b} \rangle) / \sigma^{Ti}$

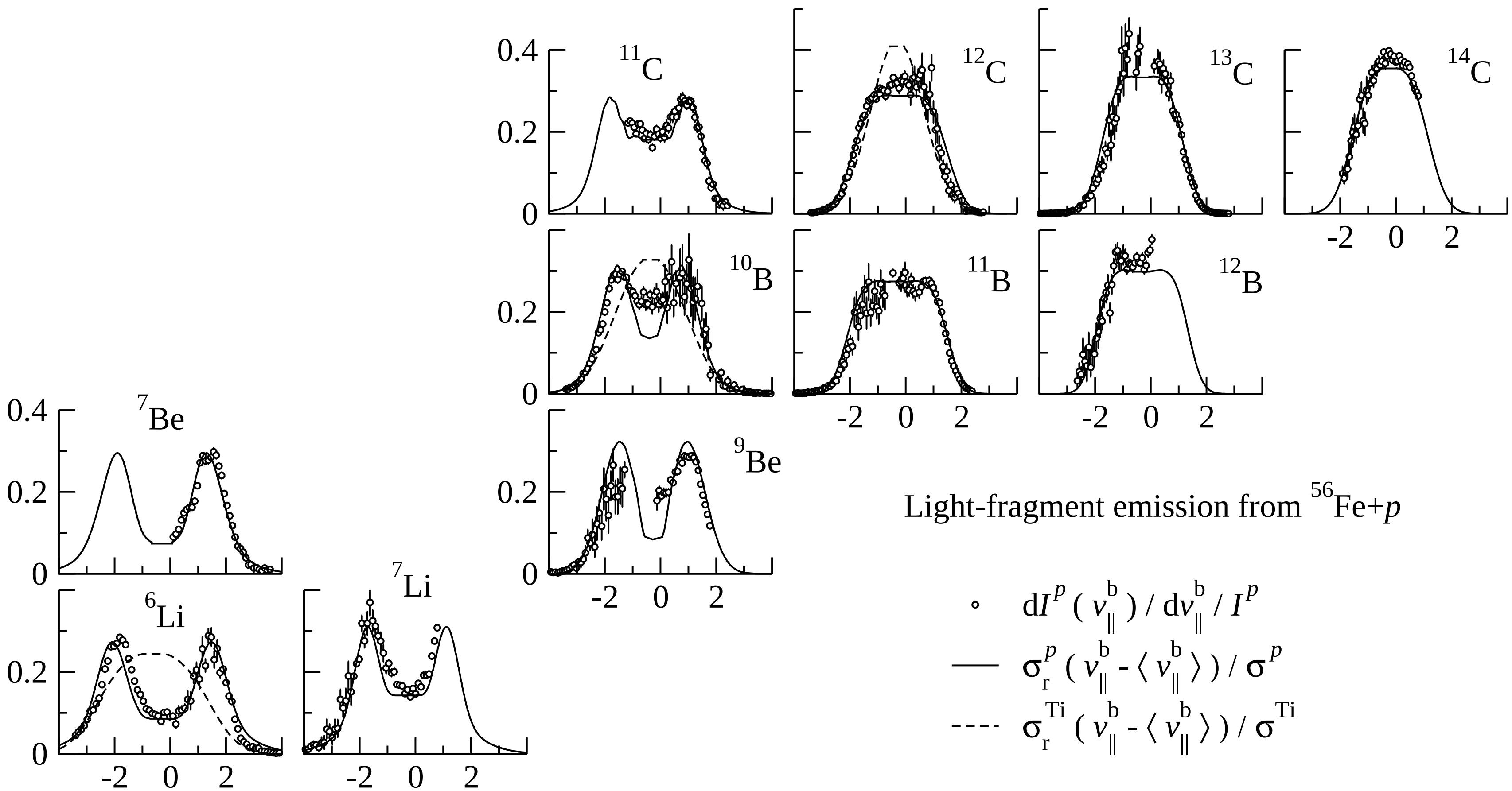

Figure 3.4: Velocity spectra of light residues produced in ^{56}Fe+$^{\mathrm{nat}}$Ti (upper diagram), and in ^{56}Fe+p at 1 A GeV (lower diagram), ordered on a nuclear chart. They are represented as a function of the velocity in the beam direction in the beam frame $v_\parallel^b$. Crosses and points indicate measured spectra $\mathrm{d}\mathcal{I}^{\mathrm{Ti}}/\mathrm{d}v_\parallel^b$ and $\mathrm{d}\mathcal{I}^p/\mathrm{d}v_\parallel^b$, respectively, defined according to eq. (3.4), and normalized to the unit. They represent all fragments transmitted through the FRS. Reconstructed velocity spectra σ_r^{Ti} and σ_r^p, defined according to eq. (3.5) and normalized to the unit are marked with dashed and solid lines, respectively. In the lower diagram, the reconstructed spectra for ^{6}Li, ^{10}B and ^{12}C emitted from ^{56}Fe+$^{\mathrm{nat}}$Ti are superimposed as dashed lines for comparison.

$\mathrm{d}\sigma/\mathrm{d}v$ vanishes at large v values and that, as a consequence, also the yield drops. By considering a large $v_{\|}$ value for which the yield is null, we can take a null $\mathrm{d}\sigma/\mathrm{d}v$ over the corresponding interval and start the procedure of reversion. This prescription for the starting point can also be extended to regions where the yield does not fade : for $v_{\|} \gg \widetilde{v}_{\perp}$ the length of the integration interval decreases as $\widetilde{v}_{\perp}^2/(2v_{\|})$, which becomes small compared to the characteristic variation length of $\mathrm{d}\sigma/\mathrm{d}v$. In this case, the latter can be assumed constant over the interval and its value deduced straightforward from eq. (3.4). The dependence of $\widetilde{v}_{\perp}$ on φ only slighly changes the procedure, while the scheme remains the same.

The yields measured for the forward emission ($v_{\|} > 0$) are expected to differ from those associated to the backward ($v_{\|} < 0$) emission. Nevertheless, in the ideal case of a perfectly isotropic emission with respect to the centre of mass, the resulting cross sections $\sigma(v_{\|} > 0)$ and $\sigma(v_{\|} < 0)$ restricted to only-forward and only-backward emission, respectively, should be identical. The difference $|\sigma(v_{\|} > 0) - \sigma(v_{\|} < 0)|$ can be an indication of the uncertainty introduced in the extraction of the cross section $\sigma(v)$ by the assumption of isotropic emission. The density of velocity vectors $\vec{v}$ in a plane containing the beam axis is presented in fig. 3.3.

We can now reduce the representation of the recoil-velocity distribution $\sigma(v)$ to one dimension, selecting only those velocities $\vec{v}$ aligned in the beam direction, and occupying only abscissae in the plots of fig. 3.3.

Due to our assumption of isotropy, we can define radial velocity distributions dividing the differential cross section $\mathrm{d}\sigma(v)/\mathrm{d}v$ associated to a given velocity v in the centre of mass by the spherical surface of radius v:

$$\sigma_r(v) = \frac{\mathrm{d}^3\sigma}{\mathrm{d}\vec{v}} = \frac{1}{4\pi v^2}\frac{\mathrm{d}\sigma}{\mathrm{d}v} \quad , \tag{3.5}$$

It should be remarked that either in the reference of the centre of mass or in the projectile frame, γ is close to the unit and consequently $\sigma_r(v)$ is directly related to the invariant cross section $\sigma_I(v)$. Indicating $m = \gamma m$ the mass of the particle, $\vec{p} = \gamma\vec{p}$ its momentum and E its total energy in the centre of mass frame (or in the projectile frame), we obtain the equality:

$$\sigma_r(v) = \frac{m^2\mathrm{c}^2}{m\mathrm{c}^2}\frac{\mathrm{d}^3\sigma}{\mathrm{d}\vec{p}} = \frac{1}{\mathrm{c}^2}E\frac{\mathrm{d}^3\sigma}{\mathrm{d}\vec{p}} = \frac{1}{\mathrm{c}^2}\sigma_I(v) \quad . \tag{3.6}$$

Also the planar cuts in velocity space $(v_{\|}^b, v_{\perp}^b)$ of fig. 3.3 are equivalent to invariant-cross-section plots [Babinet 1981].

As a technical remark, the advantage of inverse kinematics compared to direct-kinematics experiments should be pointed out. The registration of emission velocities close to the velocity of the centre of mass of the hot remnant are not prevented by any energy threshold. Thus, only in inverse kinematics we can clearly appreciate the gradual transition from a chaotic-dominated process, reflected in Gaussian-like invariant-cross-section spectra, to a Coulomb- (or eventually expansion-) dominated process, producing a hollow around the centre of mass. This characteristic signature we exploit resembles the investigation of relative velocity correlations between two fragments [Wang 1999] in full-acceptance experiments for analysing decay times. In that case, the probability to detect two almost simultaneously emitted particles in space with small differences in direction is suppressed due to the mutual Coulomb interaction.

A systematic study of the spectra of lithium, beryllium, boron and carbon is presented in fig. 3.4 and compared with the observed velocity distributions. In the ^{56}Fe+$^{\mathrm{nat}}$Ti reaction, all spectra show a bell shape. In the ^{56}Fe+p spallation, the double-humped distribution appears clearly for isotopes with mass lower than twelve units. The shape of the velocity spectra depends mostly on the mass rather than on the charge, and chains of isotopes belonging to the same elements show a transition from a bell shape toward a double-humped spectrum with decreasing mass. This transition is not always gradual but, as revealed by the neighbouring ^{11}C and ^{12}C in the lower panel of fig. 3.4, sometimes seems to be rather abrupt.

A specific discussion should be dedicated to the velocity spectra measured for the ^{136}Xe+p and ^{136}Xe+$^{\mathrm{nat}}$Ti systems. In fig. 3.5 a series of experimental spectra $\mathrm{d}\mathcal{I}(v_{||})/\mathrm{d}v_{||}$ normalized to the unit is shown for twenty isotopes having $N = Z + 1$ (these isotopes where measured with the best statistics). All spectra, both for ^{136}Xe+p and ^{136}Xe+$^{\mathrm{nat}}$Ti , can be described by the superposition of the two different shapes, the first double humped, the second Gaussian-like, the width and the integral of which varies according to the specific isotope. All spectra associated to heavy residues have a Gaussian shape. Gaussian spectra are narrow for isotopes of mass close to the projectile, associated to evaporation production. They widen for light residues, which are associated to more complex emission mechanisms. This characteristic Gaussian shape, still evident in the spectrum of ^{45}Ti, produced in ^{136}Xe+$^{\mathrm{nat}}$Ti , evolves gradually in an asymmetric distribution, which is the result of the folding of many Gaussian shapes having different mean values: this is the case of the series of isotopes ranging from ^{45}Ti down to ^{25}Mg, produced in the ^{136}Xe+$^{\mathrm{nat}}$Ti system. More negative mean values of the Gaussian components are related to smaller integrals. The resulting shape could be represented by a Gaussian function convoluted with an exponential tail. The folding represents the spread in the mean recoil in the collision. The presence of the second shape, constituted by two wide largely spaced Gaussian-like humps, characterizes the lightest isotopes produced in ^{136}Xe+p . The greatest part of the integral of the spectra of ^{7}Li and ^{9}Be is related to the two-humped shape. This contribution gradually vanishes (around ^{31}P). Also the system ^{136}Xe+$^{\mathrm{nat}}$Ti manifests the presence of the two-humped shape for isotopes lighter than ^{15}N. This was not the case for ^{56}Fe+$^{\mathrm{nat}}$Ti , where no trace of this contribution was manifested. Thanks to the large spacing between the two humps (due to the effect of Coulomb repulsion from a heavy nucleus, close to Xe in mass), the system ^{136}Xe+p shows clearly the superposition of the Gaussian-like and two-humped contribution (see isotopes ranging from ^{13}C to ^{21}Ne). The high resolution of the spectra even shows that the central Gaussian-like component is shifted in forward direction with respect to the two-humped component. This feature is rather surprising. More negative mean-recoil values are generally associaed to more violent reactions due to larger frictional effects in the collision. On the other hand, the central component recalls a volume multifragment emission, that could reflect very violent collisions, while the side component should be related to low-multiplicity fragment emission, which reflects less violent collisions. In this case, the central component should be related to a larger frictional effect and be

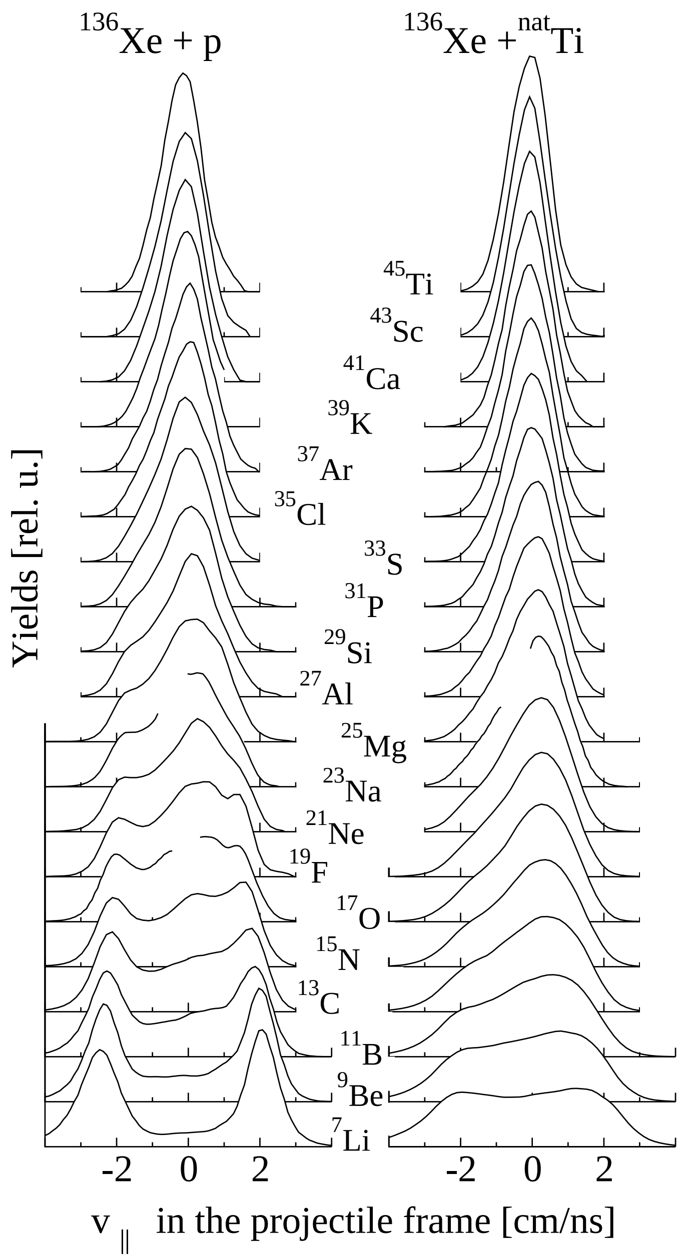

Figure 3.5: Experimental velocity spectra nomalized to the same uintegral, measured for a series of isotopes having $N = Z + 1$ in the systems ^{136}Xe+p (left) and ^{136}Xe+$^{\mathrm{nat}}$Ti (right).

therefore shifted backward with respect of the side component. We observe the opposite effect. A similar "highly unusual feature" was observed by N.T. Porile and collaborators in 1979 at Fermilab, by bombarding ^{238}U with 400 GeV protons. In this experiment, in direct-kinematic, a larger amount of fragments was registered at backward than at forward in the laboratory frame. It was concluded that this effect appears uniquely at very high energies and it was interpreted as the effect of nuclear shock waves. It should be remarked that in our experiment we do not observe forward emitted fragments (corresponding to backward emitted fragments in direct kinematics). All velocity spectra manifest backward emission in average. Only when the distribution is disentangled in Gaussian-like and two-humped components we can observe a larger back-shift for the latter component, increasing for lighter fragments, while the former component maintains its mean value close to the projectile velocity. This is the first time that such a feature is measured in ion-proton collisions in the 1 A GeV incident-energy range. The forward peaking of the emission was measured in ion-ion collisions with the FRagment Separator [Ricciardi 2003] and related to the "blast" effect induced on the spectators by the fire-ball.

3.2 Nuclide cross section

The formation cross sections are directly obtained by integration of $\mathrm{d}\sigma(v)/\mathrm{d}v$. In the appendix C, table C.1 collects the isotopic cross sections for the production of light residues, from lithium up to oxygen, measured in this work for the reaction ^{56}Fe+p and ^{56}Fe+$^{\mathrm{nat}}$Ti and the whole set of cross-sections for the systems ^{136}Xe+p and ^{136}Xe+$^{\mathrm{nat}}$Ti . The distributions of the formation cross sections evaluated for the two systems ^{56}Fe+p and ^{56}Fe+$^{\mathrm{nat}}$Ti at 1 A GeV are presented in fig. 3.6 for different light elements as a function of the neutron number and in fig. 3.7, on the chart of the nuclides. in fig. 3.8 the isotopic production is presented on a nuclide chart for ^{136}Xe+p and ^{136}Xe+$^{\mathrm{nat}}$Ti at 1 A GeV. The extension of the production appears rather similar for both the titanium-induced and the proton-induced reactions and, in particular, despite the expected difference in excitation energy reachable in the collisions with the two targets, the cross-section distributions of the residues associated to the same projectile do not manifest drastic differences in their features. A more quantitative revelation of this similarity is presented in fig. 3.9, where the mass distributions are compared. The difference in the shape of the mass spectra is significant only for the intermediate masses: the cross section of the residues of ^{56}Fe+p decreases from $A = 30$ to $A = 18$ by about one order of magnitude, while we observe only a slight decrease by about a factor of two for ^{56}Fe+$^{\mathrm{nat}}$Ti. The difference in the slope of the mass spectrum is even more significant for the nuclides ranging from $A = 100$ to $A = 50$, produced with a ^{136}Xe projectile. The data reveal that higher excitation energy introduced by the interaction with titanium, with respect to proton-induced spallation, results in decreasing the slope of the mass-spectra in the IMF-range and depleting the cross section for heavy residues in favour of an enhanced production of light fragments. However, the portion of the mass spectra corresponding to light-particle emission follows a very similar exponential slope for both systems.

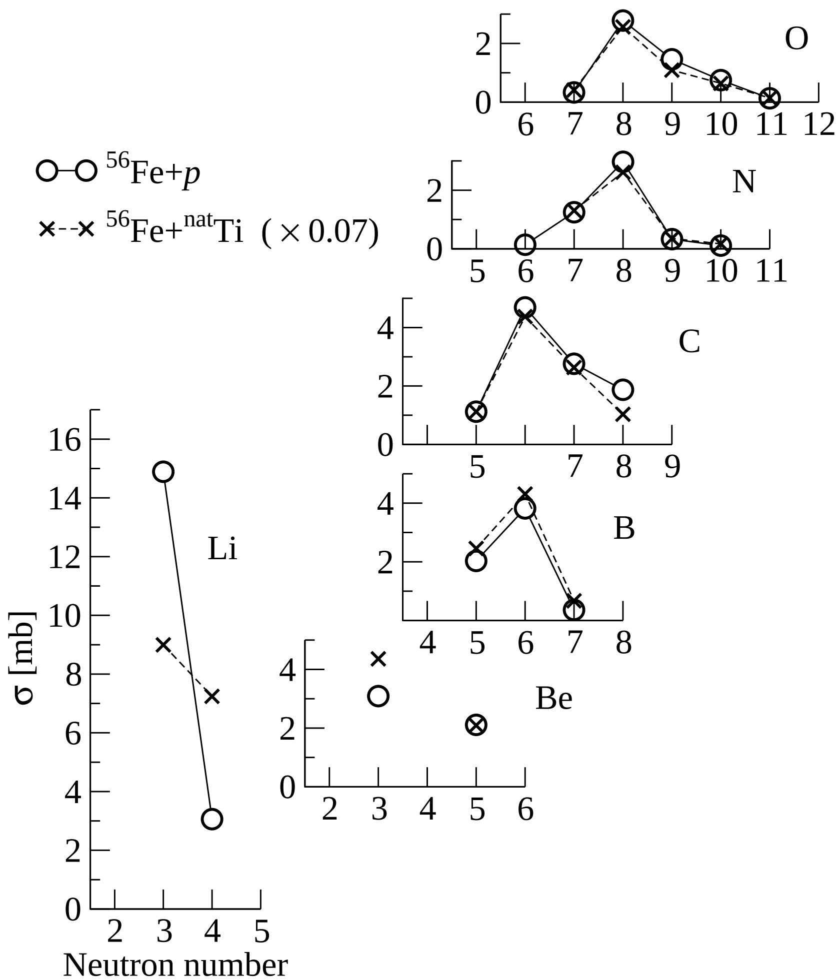

Figure 3.6: Experimental isotopic production cross sections of some light elements for the reactions ^{56}Fe+p and ^{56}Fe+^{nat}Ti at 1 A GeV. The cross sections related to the latter system are scaled of a factor 0.07. Numerical values are collected in table C.1.

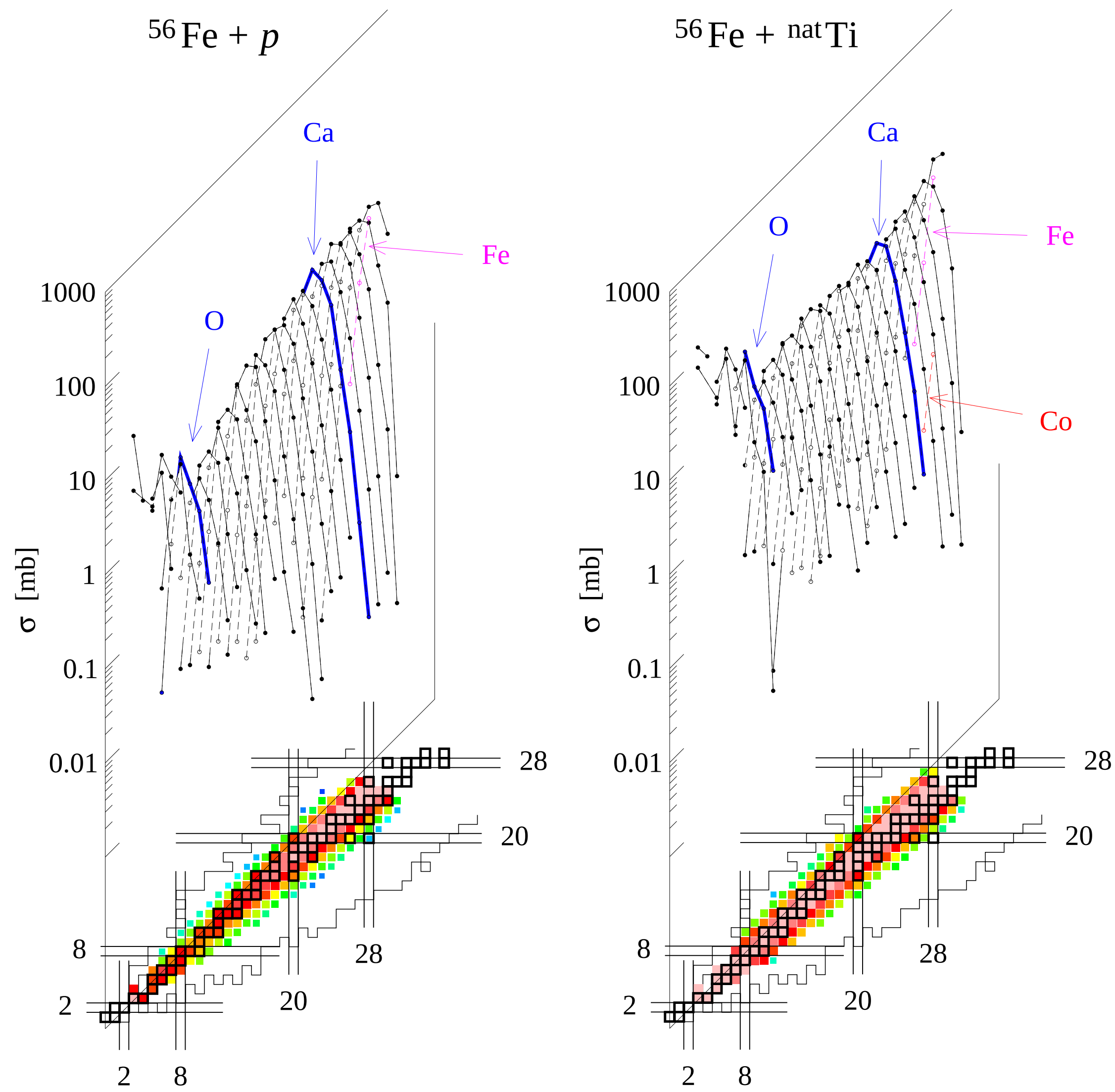

Figure 3.7: Isotopic production cross sections shown on a chart of the nuclides for the reactions ^{56}Fe+p and ^{56}Fe+$^{\mathrm{nat}}$Ti at 1 A GeV. The values for ^{54}Mn in ^{56}Fe+p and for ^{53}Cr in ^{56}Fe+$^{\mathrm{nat}}$Ti were obtained from systematics.

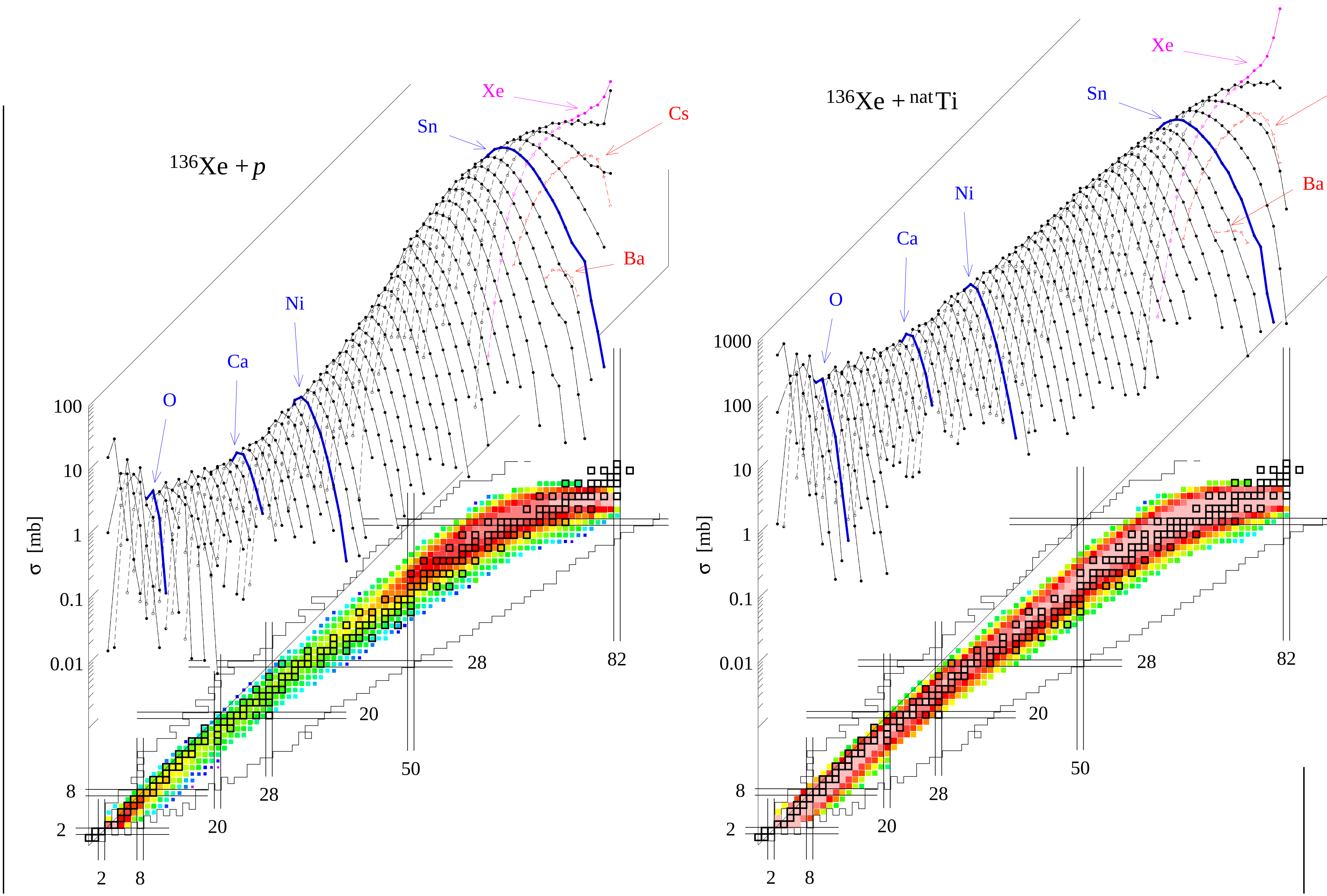

Figure 3.8: Isotopic production cross sections shown on a chart of the nuclides for the reactions ^{136}Xe+p and ^{136}Xe+$^{\mathrm{nat}}$Ti at 1 A GeV.

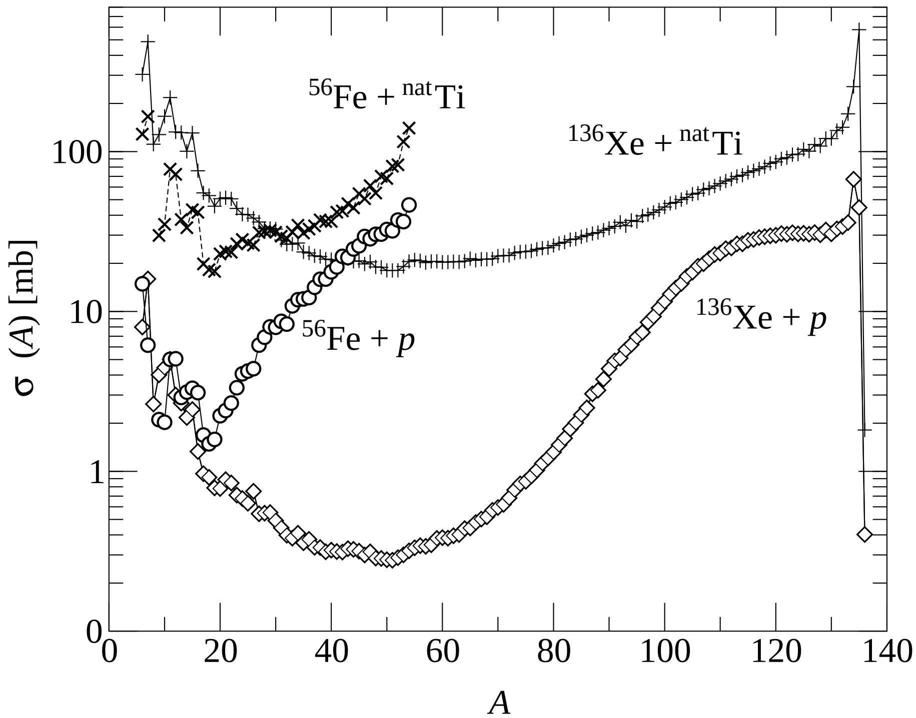

Figure 3.9: Experimental production cross sections as a function of the mass number. The statistical uncertainties are lower than 10%. The systematic uncertainties evolve from 10% for the heavy residues close to the projectile to 20% for the light fragments.

Chapter 4

The reaction mechanism

Contents

4.1 Systematics of kinematical features 50

4.1.1 Absolute-velocity spectra 51

4.1.2 Kinetic-energy spectra 54

4.2 Nuclear-model calculations 57

4.2.1 Calculation of the excitation energy of the hot collision remnants 57

4.2.2 Sequential fission-evaporation decay 60

4.2.3 Fast break-up 65

In the previous section, the full velocity distributions were reconstructed from the data and employed to obtain the residue formation cross sections for the reactions induced by the proton and titanium target, respectively. Though, the cross sections did not yield any unambiguous distinction between the reactions with the two targets that, indeed, should result into rather different deexcitation pictures on the basis of the different thermal excitations reached in the two systems. On the contrary, the particularity of the proton-induced spallation compared to the titanium-induced fragmentation arises strikingly when the kinematics of the light-particle emission is investigated. Thus, when we compare the ^{56}Fe+p and ^{136}Xe+p systems to the ^{56}Fe+$^{\mathrm{nat}}$Ti and ^{136}Xe+$^{\mathrm{nat}}$Ti systems, respectively, on the basis of the recoil velocity, we find that substantially distinct mechanisms should be involved in the light-fragment emission. In the fragmentation reaction induced by the titanium target, all the residues are emitted according to a bell-shape velocity spectrum. A long sequential decay would produce this kind of shape; in this process, neutrons, protons and clusters are in fact emitted with different angles with equal probability. Nevertheless, due to the high excitation of the hot fragments gained in such a violent collision, and due the exponential increase of the cross section of the light residues with the mass loss, we are in favour of a multifragmentation picture to depict the dominant deexcitation process. In this case, the hot source is expected to undergo a fast expansion and successively form several fragments. In this scenario [Bondorf 1995], the emission velocity of a light residue could vary largely according to different parameters: the partitioning in the multifragmentation event, the expansion of the source before the break-up phase, and the position where the tracked fragment is formed with respect to the other fragments. Also this process would result in a velocity spectrum with a bell shape centred at the mean recoil velocity, equal to the shape we observe. On the contrary, when light fragments originate from the ^{56}Fe+p and ^{136}Xe+p systems, the reaction dynamics leads to the population of one most probable emission shell in the velocity space, around the centre of mass. This is the case of ^{6}Li, produced in ^{56}Fe+p , as shown in fig. 3.3. Only a forward and a backward portion of the emission shell could be measured as selected by the conical cut that the spectrometer determined: this fully explains the double-humped velocity spectra obtained in the measurement, as shown in fig. 2.7 and in the reconstructed spectra shown in fig. 3.4. The velocity distributions of the light fragments generated in the proton-induced reaction carry the unambiguous signature of a strong Coulomb repulsion in the emission process. This observation evidently excludes that the light fragments could be the final residues of a long sequential evaporation chain. The strong Coulomb component in the emission process rather reflects the dominating influence of a very asymmetric split of the source.

4.1 Systematics of kinematical features

On the basis of the ensemble of experimental data on the production cross section and on the emission velocity of the residues, we devote this section to discuss the reaction phenomenology. In accordance to the vast literature dedicated to ion-ion fragmentation (explored in the reviews [Bondorf 1995, Richert 2001]), we can safely relate the ^{56}Fe+$^{\mathrm{nat}}$Ti and ^{136}Xe+$^{\mathrm{nat}}$Ti reactions to the formation of highly excited systems, the decay of which is commonly interpreted as a multi-body instantaneous disassembly. In the following, we will refer to the ^{56}Fe+$^{\mathrm{nat}}$Ti and ^{136}Xe+$^{\mathrm{nat}}$Ti collisions as a guideline for comparing to a fragmentation scenario. We will rather concentrate on the reaction mechanism of the proton-induced collision, which points to competitive types of decay at the same time.

From a first analysis, the main characteristics of the deexcitation of the ^{56}Fe+p and ^{136}Xe+p systems, recalling a strong Coulomb repulsion, evocate a binary decay process. In general, more than one kind of reaction could lead to a binary decay. Either the system breaks apart directly following the entrance channel. This is the characteristic of transfer reactions. Almost like in elastic scattering the projectile and the target nuclei keep essentially their kinematical properties, they just exchange a few nucleons. In this case, the kinetic energy and the angular distribution keep memory of the entrance channel and cannot be parameterised by a global systematics. Or they merge to a combined system, thermalise, and then decay in two parts. In this case, the kinetic energy and the angular distribution does not keep any memory of the entrance channel, except that the angular momentum of the system has some trivial consequences on the angular distribution. Thus, when a compound nucleus is formed, the kinetic energy released can be parameterised by an empirical universal description. We might notice that other processes like deep-inelastic reactions, or fast fission are in between these extremes. On the other hand, other relevant features, like the high production yields for both light and about half-projectile-mass residues, could evocate the character of a fast decay, in line with the scenario of a sudden disassembly of the source depicted for the ^{56}Fe+$^{\mathrm{nat}}$Ti and ^{136}Xe+$^{\mathrm{nat}}$Ti systems. The high incident energy imposes that only two among all the scenarios we mentioned may be taken into consideration: either the asymmetric split of a compound nucleus, or a fast break-up.

Our first attempt will be to test the pertinence of the experimental data on the emission velocities with a general systematics. Afterward, we will discuss the intricacy of the several possible contributions to the spectral shape of the kinetic-energy distributions, and the difficulty to extract insight on the excitation energies involved in the reaction directly from the measurement.

4.1.1 Absolute-velocity spectra

A recurrent analysis of the Coulomb-repulsion aspects is the comparison of the distribution of absolute velocities of outgoing fragments $v = |\vec{v}|$ (where $\vec{v}$ is the corresponding velocity vector in the centre of mass of the hot remnant) with the systematics of total kinetic energy released in fission. We intend to follow this approach (e.g. [Wang 1999]) to test the compatibility of the light-fragment emission in ^{56}Fe+p with an asymmetric-fission picture. The FRagment Separator is particularly efficient in measuring recoil velocities, because the magnetic rigidity of the residues is known with high precision (see section 2.4). Indeed, the identity of the mother-nuclei is hidden in the complexity of the interaction processes related to high-energy collisions, like the intra-nuclear cascade and some evaporation events prior to the binary decay. The present new data are especially significant as they are the first measurement of the velocities of fragments issued of proton-induced splits of iron-like nuclei. On the other hand, fission velocities of residues of light nuclei have been widely investigated in fusion-fission experiments [Sanders 1999], with the advantage of excluding most of the ambiguities on the identification of the fissioning nucleus. Data on symmetric fission of nuclei close to iron, formed in fusion reactions were published by Grotowski et al. [Grotowski 1984] and were the basis for the revised kinetic-energy-release systematics of Viola [Viola 1985]. This systematics establishes a linear dependence of the most probable total kinetic en-

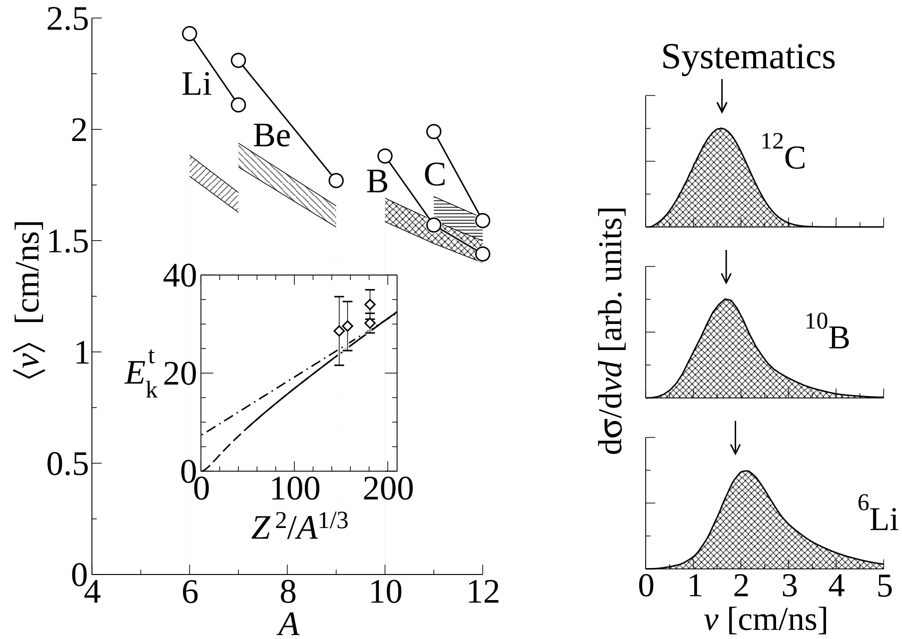

Figure 4.1: *Left panel* Mean absolute velocities in the reference frame of the centre of mass of the hot remnant, measured for residues of the ^{56}Fe+p system (open circles) and deduced from the systematics of Tavares and Terranova [Tavares 1992] (hatched bands). The width of the hatched areas results from the range of the possible mother nucleus from ^{46}Ti (lower values) to ^{56}Fe (higher values). In the insert, data points on the total kinetic energy released in a symmetric split of nuclei close to iron, measured by Grotowski et al. [Grotowski 1984] are compared to the systematics of Viola [Viola 1985] (dot-dashed line) and with the systematics of Tavares and Terranova [Tavares 1992] (solid line). *Right panel* Measured absolute-velocity spectra for the residues ^{6}Li, ^{10}B, and ^{12}C produced in the ^{56}Fe+p system. The arrows indicate the values obtained by the systematics of Tavares and Terranova.

ergy E_k^t released in a symmetric fission to the quantity $Z^2/A^{1/3}$, evaluated for the mother nucleus:

$$E_k^t = aZ^2/A^{1/3} + b \qquad , \tag{4.1}$$

where A and Z identify the fissioning nucleus and a and b are parameters fitted to the experimental data ($a = (0.1189 \pm 0.0011)$ MeV, $b = (7.3 \pm 1.5)$ MeV). More recently, new data obtained for the binary split of even lighter nuclei than iron inspired Tavares and Terranova [Tavares 1992] to revisit the systematics of Viola once more. The new systematics is close to the systematics of Viola for heavy nuclei down to $Z^2/A^{1/3} \approx 200$. As shown in the insert of fig. 4.1, iron-like nuclei constitute a turning point: for lower masses the function changes slope, so that the total kinetic energy released vanishes for Z approaching 0. As anticipated by Viola [Viola 1985], the expectation for a slope change around iron results by the effect of diffuseness of light nuclei in disturbing the formation of the neck, in the liquid-drop picture. The following relation was deduced:

$$E_k^t = \frac{Z^2}{aA^{1/3} + bA^{-1/3} + cA^{-1}} \qquad , \tag{4.2}$$

where a b and c are fitting parameters ($a = 9.39\text{MeV}^{-1}, b = -58.6\text{MeV}^{-1}, c = 226\text{MeV}^{-1}$).

Since the systematics is valid for symmetric splits only, a term should be added to extrapolate to asymmetric splits, when two fragments are formed with masses m_1, m_2, mass numbers A_1, A_2, and charges Z_1, Z_2, respectively. Following the hypothesis of non-deformed spheres at contact (as also imposed in [Tavares 1992]), the Coulomb potential is proportional to the product of the charges of the fission fragments Z_1Z_2, divided by the distance of their centres, which varies with $A_1^{-1/3} + A_2^{-1/3}$. The conversion from the symmetric to asymmetric configuration is therefore :

$$\frac{E_k^t}{E_{k,\text{symm}}^t} = \frac{Z_1Z_2/\left(A_1^{1/3} + A_2^{1/3}\right)}{\left(\frac{Z}{2}\right)^2 \Big/ \left[2\left(\frac{A}{2}\right)^{1/3}\right]} \qquad . \tag{4.3}$$

It should be remarked that the possible presence of a neck is not included in this simple relation that, therefore, is a good approximation for light systems only. From the momentum conservation and the introduction of the reduced mass $\mu = m_1m_2/(m_1 + m_2)$, we can relate the total kinetic energy to the velocity v_1 of the fragment A_1 by the relation $E_k^t = m_1^2v_1^2/2\mu$. Introducing the latter form of E_k^t in the relations (4.3), and substituting the total kinetic energy released in symmetric fission with the corresponding value given by the systematics E_{syst}^t, we obtain the conversion

$$\frac{v_1^2}{E_{\text{syst}}^t} = 2^{11/3}\ \frac{\mu}{m_1^2}\frac{A^{1/3}}{A_1^{1/3} + A_2^{1/3}}\frac{Z_1Z_2}{Z^2} \qquad . \tag{4.4}$$

Following the strategy of previous publications, e.g. [Wang 1999], for the same light residues we compare the centroids of the measured absolute velocity spectra to the predicted velocities in fission events; the latter are deduced from the systematics of total kinetic energy released in fission by applying the relation (4.4). In the right side of fig. 4.1 we observe that, while the most probable absolute velocity does not diverge considerably from the systematics (assumed for ^{56}Fe as mother nuclei), the spectra of lighter fragments exhibit a long exponential tail for very high velocities. As a consequence of the asymmetry of the absolute velocity spectra with respect to a Gaussian distribution, the experimental centroids lie above the fission systematics, as shown in the left side of fig. 4.1. The hatched bands represent the range in velocity due to an assumed variation of the mother nucleus from ^{46}Ti (lower velocities) up to the projectile (higher velocities). In previous works (e.g. [Barz 1986, Wang 1999, Karnaukhov 1999]) such tails to very high velocities, reflected in the divergence from the systematics, were related to the emission from an expanding system in its initial expansion stage.

4.1.2 Kinetic-energy spectra

Directly obtained from the absolute-velocity spectra, the distributions of kinetic energy E_k offer another representation of the kinematics, where some more classic features could be searched for. In fig. 4.2 similarities and differences in kinetic-energy spectra associated with proton and titanium target nuclei are illustrated for ^{56}Feprojectiles. The tails to high emission velocities (fig. 4.1, right panel) lead to long tails in the kinetic-energy spectra and characterize both systems. We interpret it as a general indication that the collision generated very high excitation energy

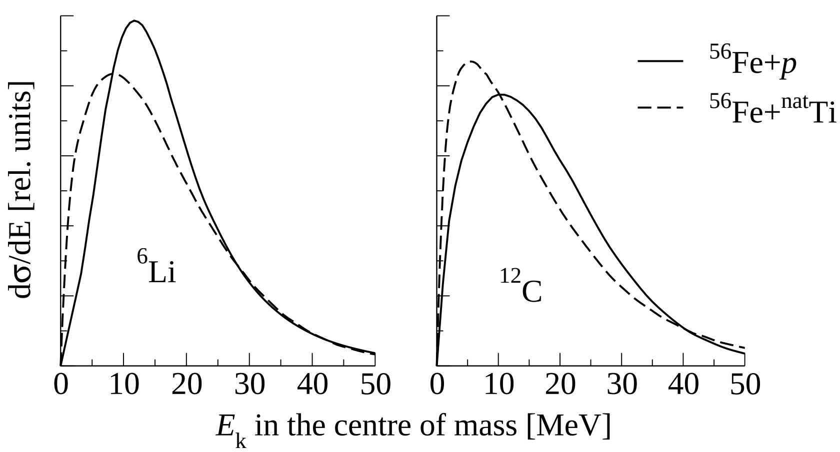

Figure 4.2: Kinetic-energy spectra in the centre of mass of the emitting source obtained from the reconstructed experimental velocity distributions in the case of emission of ^{6}Li and ^{12}C, respectively. The spectra are compared for the ^{56}Fe+p system (solid lines) and for the ^{56}Fe+^{nat}Ti system (dashed lines). All spectra are normalized to the same area. The smooth distributions result from a spline fit procedure to the data.

in the system. It would be tempting to even deduce the thermal properties of the system. In this case, with particular concern for the ^{56}Fe+p and ^{136}Xe+p systems, we could draw assumptions on the probability for break-up channels. Unfortunately, even if in some studies the nuclear temperature was deduced from the inverse slope parameter [Kotov 1995], the mixing up of several effects in the observed kinematics yields serious ambiguities in the extraction of thermal properties of the source. We can list at least eight of the combined effects describing the observed spectral shapes.

1. The presence of a Coulomb barrier results in the deviation of the spectral shape from a Maxwell-Boltzmann distribution (the maximum moves to higher values).

2. The transmission through the barrier is ruled by a Fermi function with an inflection point at the barrier and not by a discontinuous step function. This effect introduces a widening of the spectrum.

3. As a result of the initial stage of the collision, an ensemble of several possible sources with different Z and A are related to different Coulomb barriers. The folding of different Coulomb barrier peaks results in a broader hump.

4. If emitted nuclei undergo further evaporation events, the spectrum widens.

5. The temperature of the hot source acts on the recoil momenta of the emitted fragments. If at least major disturbing effects like the variation of the emitting source, the Fermi momentum in the hot fragmenting nucleus, described below, and the transmission through the barrier were negligible, it would be possible to deduce the temperature of the equilibrated fragmenting system from the inverse slope parameter fitted to the tail of the high side of the energy spectrum of the residues.

6. The Fermi momentum of particles removed in the collision with protons or abraded in the interaction with the titanium target produces a momentum spread that could be evaluated according to Goldhaber's formalism [Goldhaber 1974].

$$\sigma^2_{p_F} = \sigma^2_F \frac{A_i(A - A_i)}{A - 1} \quad , \tag{4.5}$$

where A is the mass of the hot remnant, A_i is the mass of the emitted cluster and σ_F is the Fermi-momentum spread. The momentum spread deriving from the Fermi-momentum spread produces a distribution of momenta of the centre of mass of the remnants in the projectile frame. In deducing the energy spectra of the residues in the frame of the centre of mass of the remnant, the spread related to the Fermi-momentum could not be eliminated as the mass of the remnants are unknown. As a result, the Fermi-momentum contributes both to widening the spectrum and incrementing the tail for high energies. Quoting from Goldhaber [Goldhaber 1974], when a thermalised system with a temperature T and mass A emits a cluster of mass A_i, the momentum spread of the fragment spectrum is

$$\sigma_p^2 = \mathrm{m_0 k} T \frac{A_i(A - A_i)}{A} \quad , \tag{4.6}$$

where $\mathrm{m_0}$ is the nuclear mass unit and k is Boltzmann's constant. The momentum spread σ_{p_F} related to the Fermi momentum adds to the momentum spread induced by the reaction. This means that, just reversing the previous relation, the additional contribution to the temperature related to the Fermi momentum is equal to the apparent temperature

$$T_{p_F} = \frac{\sigma_{p_F}^2}{\mathrm{m_0 k}} \frac{A}{A_i(A - A_i)} \quad . \tag{4.7}$$

As it was remarked in early studies [Westfall 1978], the extraction of the nuclear temperature from the measured energy spectra of the residues is therefore a dangerous procedure (a recent discussion of the problem of the Fermi motion is presented in [Odeh 2000]).

7. Multifragmentation events could be accompanied by the expansion of the nuclear system. Nuclei emitted in the initial instant of the expansion would populate the high-energy tail of the spectrum. This is the case for very excited systems [Siemens 1979].

8. The multiplicity of intermediate-mass fragments simultaneously emitted might be reflected in the maxima. According to previous investigations [Oeschler 1900], a drop in the maximum energy of the outgoing fragments in a simultaneous disintegration of the source indicates higher average multiplicity of intermediate-mass fragments: this is related to the larger number of participants in the redistribution of the kinetic energy.

The last of the enumerated contributions to the energy spectra is evident in fig. 4.2. In the proton-induced collision, the position of the maximum corresponds to larger kinetic energy than in the case of the titanium target. This might be related to higher multiplicity of intermediate-mass fragments for the ^{56}Fe+$^{\mathrm{nat}}$Ti (or ^{136}Xe+$^{\mathrm{nat}}$Ti) system.

From the analysis of velocity and energy spectra we conclude that no clear evidence of the action of a fission barrier could be found. Either fission channels are not favoured, or other processes obscured them, like additional evaporation stages or the contribution of many mother nuclei rather different in mass. The most relevant result is the manifestation of high-velocity tails, which we interpreted as possible indications of a preequilibrium expansion phase.

4.2 Nuclear-model calculations

We had some hints that very highly excited systems are formed even in the proton-induced interaction, but we could not extract quantitative values directly from the experiment. We could not recognise the presence of a fission barrier, but a more complete analysis is required to exclude that solely compound-nucleus decays are sufficient to explain the light- fragment production. Thus, we wish to carry out a complete reconstruction of the whole reaction process and compare the ensemble of experimental results with the calculations.

Henceforth, we will restrict to the ^{56}Fe+p and ^{136}Xe+p systems. In particular, we will discuss two possible descriptions for the dominant process of light-fragment formation: either a series of fission-evaporation decays from a compound nucleus, or a fast break-up of a diluted highly excited system, in line with a multifragmentation scenario. To fix the initial conditions for the two decay models, we previously need to calculate mass, charge and excitation-energy distributions of hot remnants, as these quantities are not observable in the experiment.

4.2.1 Calculation of the excitation energy of the hot collision remnants

The initial non-equilibrium phase of the interaction ^{56}Fe+p or ^{136}Xe+p was described in the framework of the intranuclear cascade-exciton model developed by Gudima, Mashnik and Toneev [Gudima 1983]. The model describes the interaction of an hadron or a nucleus traversing a heavy ion, considered as a finite open system, composed of two degenerate Fermi gases of neutrons and protons in a spherical potential well with diffuse surface. The interaction, pictured as a cascade of quasi-free nucleon-nucleon and pion-nucleon collisions, produces high-energy ejectiles, that leave the system, and low-energy particles that are trapped by the nuclear potential. The cascade progresses until all the ejectiles with sufficient kinetic energy to overcome the nuclear potential (the propagation of which is treated in terms of Boltzmann transport equation) have left the nucleus. As many holes as the number of intranuclear collisions are produced in the Fermi gas. The number of trapped particles and the number of holes (or excitons, without distinction) determines the excitation energy of the so-called “composite nucleus”.

Hot remnants are often treated as equilibrated or partially equilibrated systems, both in the case of compound-nucleus formation and at a freeze-out state. Thus, an additional thermalization process might be necessary to describe the transition from the initial non-equilibrium phase of the collision to the equilibrium phase governing the decay. Following the hypothesis of the preequilibrium exciton model, the intranuclear cascade continues to develop through the composite nucleus by a sequence of two-body exciton-exciton interactions, until equilibrium is attained.

Two kinds of decay characterize the composite nucleus: either the transition to a more complicated exciton state, or the emission of particles into the continuum. While in Griffin's model [Griffin 1966] all decays are equiprobable, successive developments proposed more elaborate descriptions of the competition between decay modes. In our calculation we adopted a model inspired to Blann's preequilibrium exciton model [Blann 1971], and based on the formalism developed by Sudov and collaborators [Sudov 1993]. The initial state of the residual nucleus is determined by the sum of the energies of the holes and particles trapped in the nuclear potential, in the instant that coincides to the stopping time of the intranuclear cascade. The subsequent thermalization process describes the evolution in time of the probability of populating a state with a given number of excitons, taking into account particle-hole

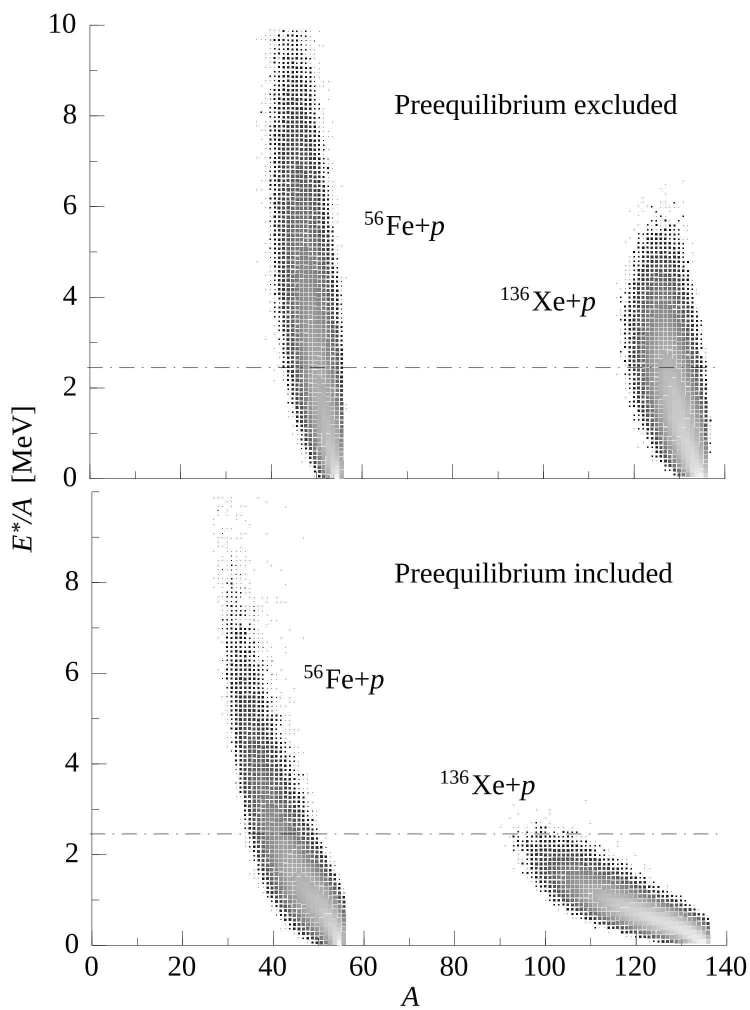

Figure 4.3: Hot-fragment distributions generated in the intranuclear cascade [Gudima 1983], in the case of exclusion (left) and inclusion (right) of a preequilibrium stage [Blann 1971], for the ^{56}Fe+p system (top) and the ^{136}Xe+p system (bottom). The horizontal straight line defines the excitation energy per nucleon that corresponds to a temperature of 5 MeV.

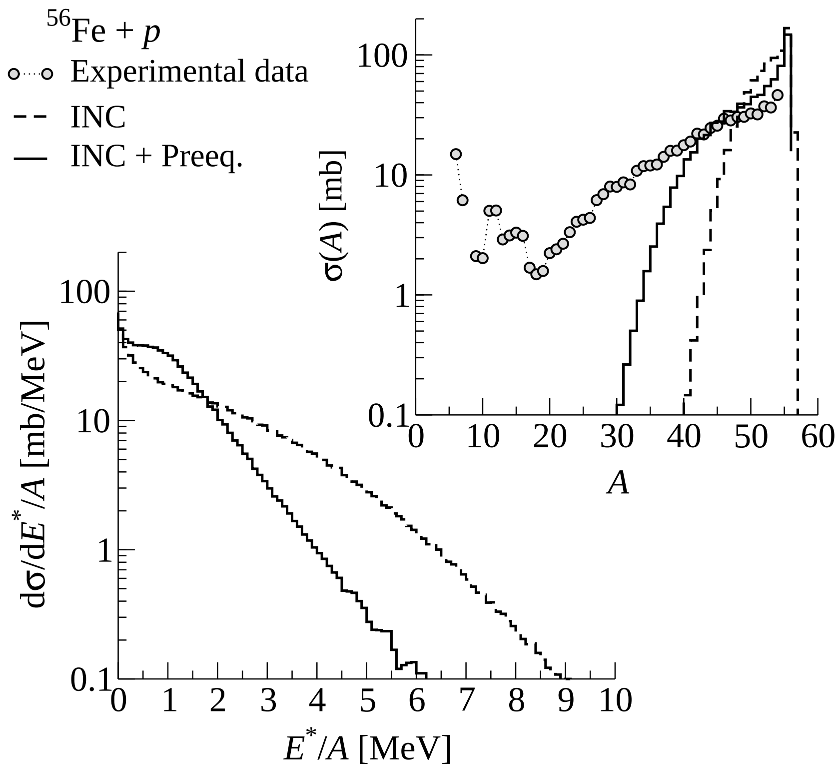

Figure 4.4: Calculated production of the hot fragments after the intranuclear cascade (modelled according to [Gudima 1983]) and a preequilibrium stage (simulated according to [Blann 1971]), for the ^{56}Fe+p system. The cross sections of the hot fragments are shown as a function of the excitation energy per nucleon E^*/A of the source (bottom-left) and the mass number (top-right). The mass distribution of cross sections of the hot fragments is compared to the experimental final-residue production.

annihilation, exciton creation, and particle-emission rates [Blann 1971, Sudov 1993]. Complex particles can be also emitted, and the associated emission-rate is determined as the probability of particle coalescence inside the nucleus in coordinate space (and not in momentum space as in coalescence models [Butler 1963] that are often adopted in the description of deep-inelastic nuclear reactions; coordinate-space coalescence is more similar to pick-up models [von Egidy 1987]). The effect of preequilibrium is to let the number of excitons increase until the creation of excitons is counterbalanced by the particle-hole annihilation, and the number of excitons attains asymptotically its value at equilibrium. At this stage the nucleus is thermalised and the preequilibrium process terminates.

In fig. 4.3 we present a calculation of the hot-fragment distribution generated in the intranuclear cascade for the ^{56}Fe+p and ^{136}Xe+p systems with and without the inclusion of a preequilibrium stage, respectively. More quantitatively, in fig. 4.4 the projections of the distribution in the case of ^{56}Fe+p are shown as a function of the excitation-energy-to-mass ratio and mass. We observe that preequilibrium is particularly effective in evacuating part of the excitation energy and widening the distribution as a function of the mass. The hot-fragment mass distribution is compared to the measured production of the final residues, in order to indicate the extension of the deexcitation process. In the case of ^{56}Fe+p (see fig. 4.3 and 4.4), when preequilibrium is suppressed, the energy per nucleon available for the deexcitation largely exceeds 2.5 MeV, a value that corresponds to the temperature of around 5 MeV, for a fully thermalised system. In this case, the multifragmentation regime is accessible. If preequilibrium is included, the average excitation of the system extends still right up to the expected threshold for a freeze-out state. In the case of ^{136}Xe+p (see fig. 4.3) the excitation energy of the system seems to be sufficient for accessing the multifragmentation regime only when preequilibrium is suppressed. Preequilibrium is more efficient in decreasing the excitation energy in ^{136}Xe+p that in ^{56}Fe+p . The physical reason for this remarkable difference can be related to the size of the system. A property of systems with larger mass is to have a higher level density: as the levels are closer in energy the number of excitons at equilibrium is higher in systems of larger size. As a consequence, in ^{136}Xe+p , preequilibrium progresses for a longer time than in the ^{56}Fe+p system, resulting in a larger number of emitted ejectiles and in a greater reduction of the excitation energy. The final hot-fragment distribution obtained for ^{136}Xe+p after preequilibrium is largely below 2.5 MeV and no multifragmentation channels are expected for the decay. In the following, we will conclude that the preequilibrium stage represents a difficulty in our description. Its inclusion in the reaction model is consistent in the case of ^{56}Fe+p , while it should be suppressed in order to obtain a better agreement with the measured data of ^{136}Xe+p . In our calculation we might have not been specific enough in adopting Blann preequilibrium exciton model independently of the type of deexcitation scenario. In this respect, when the conditions of the interaction lead to multifragmentation, the evolution of the composite nucleus is more complicated, as the system is supposed to expand. In the course of the expansion process, an intense disordered exchange of charge, mass and energy among its constituents is expected. The density of nuclear matter evolves to a more dilute state, the freeze-out, at which breakup occurs. Sophisticated thermal-expansion models were specifically developed to describe this thermalization process [Karnaukhov 1999, Avdeyev 1998].

According to this previous step of the calculation, oscillations in direction of breakup channels might be possible at these excitation energies and they are expected to be still in competition with compound-nucleus decay. We will proceed to evaluate the extent of this competition by the use of deexcitation models.

4.2.2 Sequential fission-evaporation decay

In order to describe the deexcitation process in the framework of sequential fission-evaporation decays, we applied the code GEMINI [Charity 1988]. Within GEMINI a special treatment based on the Hauser-Feshbach formalism is dedicated to the emission of the lightest particles, from neutron and proton up to beryllium isotopes. The formation of heavier nuclei than beryllium is modelled according to the transition-state formalism developed by Moretto [Moretto 1975]. All asymmetric divisions of the decaying compound nuclei are considered in the calculation of the probability of successive binary-decay configurations. The total-kinetic-energy release in fission originally parameterised according to the systematics of Viola [Viola 1985], eq. (4.1),was replaced by the systematics of Tavares and Terranova [Tavares 1992], formulated according to the relation (4.2), and extrapolated for asymmetric splits by the use of the conversion (4.4).

We simulated the decay of two possible ensembles of hot remnants, those issued directly from the stage of intranuclear cascade, and those which lost part of excitation energy and mass in a preequilibrium phase. The resulting distributions of final residues are almost indiscernible, revealing that the intermediate-mass fragments (especially those around oxygen) are not especially sensitive to the variation of average excitation energy of the system. It might be also pointed out that, when very hot fragments are allowed to decay by solely fission-evaporation channels, many nucleons and some light clusters are liberated at the very beginning of the deexcitation, before eventually forming an intermediate-mass fragment by fission. When the preequilibrium phase is suppressed, this preliminary emission could constitute

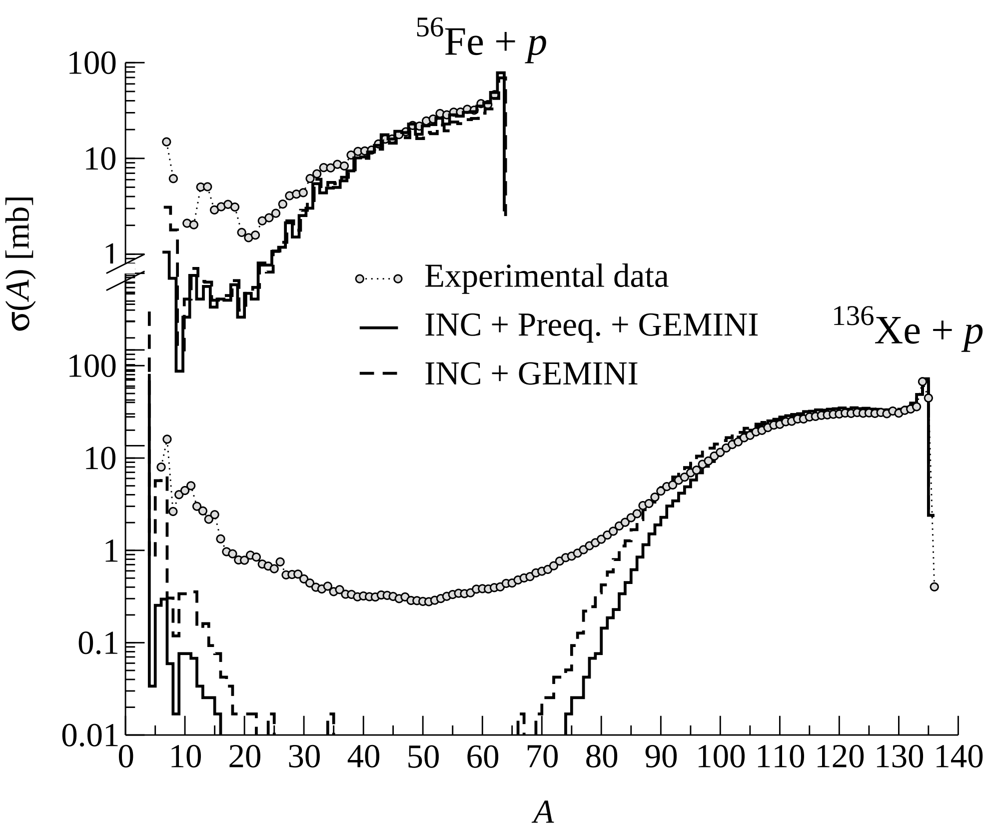

Figure 4.5: Comparison of the measured mass distributions as a function of the mass number for the systems ^{56}Fe+p and ^{136}Xe+p with the results of GEMINI.

a compensating process. In average, the relation between energy loss and mass loss could be similar in the two processes, and lead to analogous results. The difference is only conceptual, as the preequilibrium acts on a system still evolving toward thermalization, and particle evaporation is connected to a completely thermalised system. Only lithium and beryllium revealed a visible enhancement in the yields with the increase of average excitation energy.

The result of the model calculation, compared with the measured cross sections is presented in fig. 4.5. The evaluation of the heavy-residue cross sections is consistent with the experimental data, but a sizable underestimation of the production fails to reproduce the intermediate-mass region. Especially the production of the residues populating the characteristic hollow in the mass distribution reveals to be generally underestimated by the calculation. To complete the comparison, we turn now back to the first key observable found in our experimental investigation: the velocity spectra of light fragments. In the first row of fig. 4.6 the experimental spectra of ^{6}Li, ^{10}B, ^{11}C and ^{12}C produced in ^{56}Fe+p are shown, together with their velocity reconstruction (solid line). Within GEMINI, all decays are decorrelated in time and when more fragments are produced they do not interact in the same Coulomb field. Binary compound-nucleus emission is connected with a restricted range of heavy sources close to the projectile mass, reflected in the small width of the Coulomb peaks, as shown in the second row of fig. 4.6. This feature characterizes only the formation of the lightest fragments and disappears with increasing mass of the residues. The calculations presented in the second row of fig. 4.6 should not be compared to the experimental data. The effect of the Coulomb repulsion involved in the deexcitation and disentangled from the smearing effect of the intra-nuclear cascade and preequilibrium emission can be appreciated in the third row of fig. 4.6, where the reference frame has been fixed to the centre of mass of the initial system formed at the beginning of the fission-evaporation process. In the calculation, the transformation of the two Coulomb peaks into one single wide hump occurs for lower masses than experimentally observed. The model generates one single hump in the longitudinal velocity spectra of light fragments when a longer evaporation cascade is involved, and characterized by mainly alpha and nucleon emission. Moreover, the total width of the calculated spectra is narrower than observed.

A schematic view of the evaporation process is shown in fig. 4.7. The fission-evaporation processes as modelled by GEMINI result in one or more deexcitation branches leading from one hot remnant to one or more intermediate-mass fragments. We select all branches where a given residue is formed as an end-product and we count the number of deexcitation steps n_{tot} for each of those specific chains. In one fission-evaporation chain, an intermediate-mass fragment could be emitted and form the given end-product by further deexcitation steps. In such a process we do not follow the deexcitation of the complementary partner. As an extreme case, when the given end-product is emitted promptly by the hot remnant, we count one step ($n_{tot} = 1$). Following the branch leading to a given end-product we identify the emission stage i, where the greatest absolute-velocity component is registered. The difference of mass ΔA_i between the parent nucleus A_i and the daughter is associated

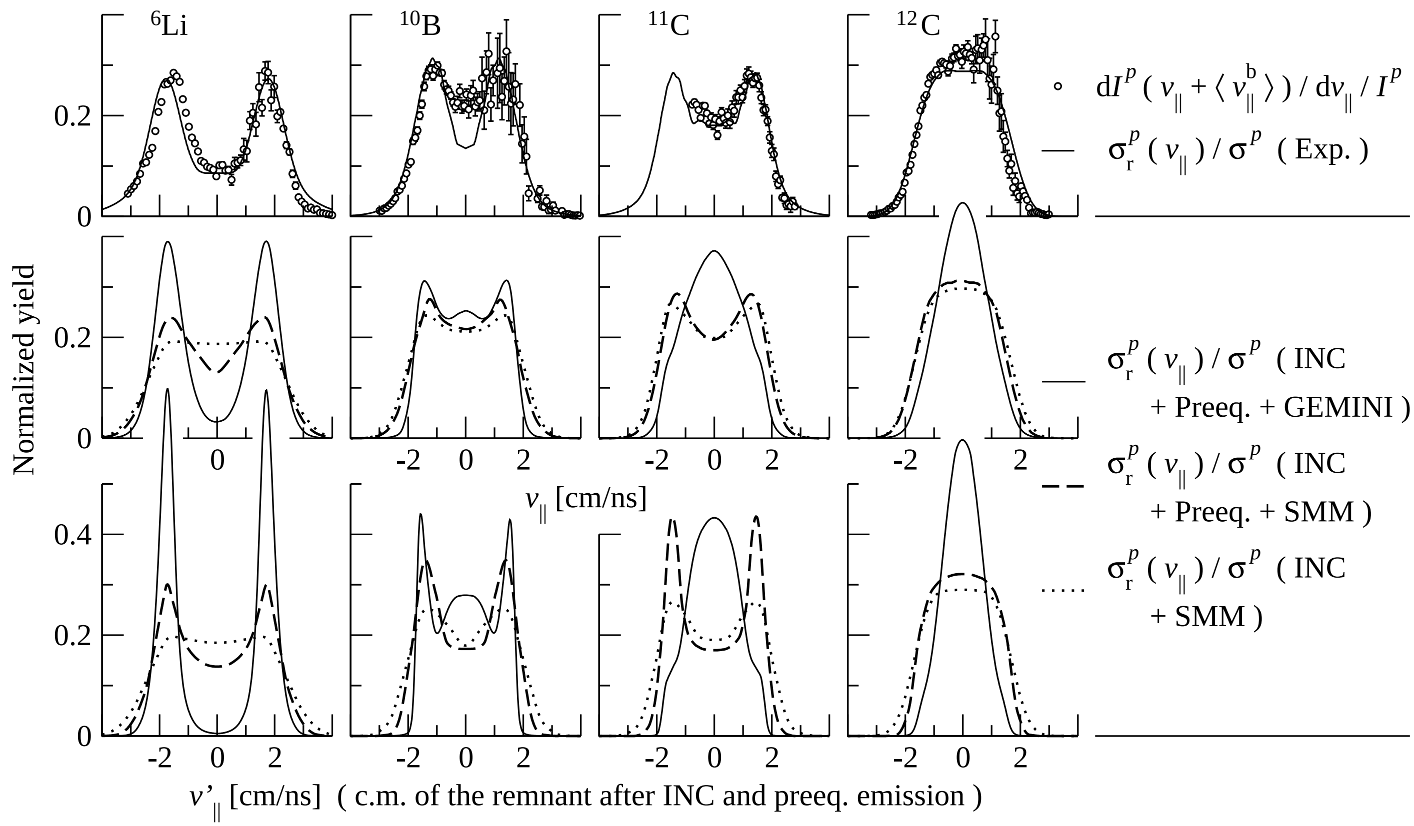

Figure 4.6: *First row:* Experimental velocity spectra (circles) and reconstructed velocity spectra (solid line) for the reaction $^{56}Fe+p$. Each spectrum is drawn in the reference frame corresponding to the measured average velocity value of the fragment considered. (This frame corresponds to the "Centre of mass" frame of the reaction product drawn in figure fig. 2.9) *Second row:* Calculated velocity spectra obtained by GEMINI or SMM following INC and the preequilibrium stage, and from SMM following directly INC. Each spectrum is drawn in the reference frame corresponding to the calculated average velocity value of the fragment considered. *Third row:* Velocity recoil introduced by the GEMINI or SMM phase alone (recoils by INC and preequilibrium stages not included). All spectra are normalized to the unit.

to this specific step. The accumulation of counts on the diagonal lines of the upper diagrams show that ^{6}Li and ^{10}B are formed as end-products mainly at the step i. It is also evident that ^{6}Li and ^{10}B are mostly emitted by heavy mother nuclei A_i. On the contrary, the emission of ^{12}C is mainly described by a band where ΔA_i is smaller that the end-product, and is decorrelated from A_i. The lower plots give indications about the length of the evaporation cascade. The number n_i corresponding to the emission stage i is correlated to the total number of evaporation steps n_{tot}. ^{6}Li is emitted almost always promptly from the hot remnant. On the other hand, the emission of ^{12}C accounts in general for more steps; since often $n_i < n_{tot}$, the greatest absolute velocity component is usually imparted in the emission of a heavier residue, that leads to the formation of ^{12}C by successive evaporation of mainly protons and neutrons. Within GEMINI the binary decay of an iron-like nucleus is governed by an inverse-U-shaped potential leading to a U-shaped mass distribution of the products from a binary decay in one step between A = 0 up to the mass of the initial decaying nucleus. A very asymmetric split is favoured compared to a less asymmetric one by a lower barrier. The temperature has an influence on the U-shaped mass distribution. While the barriers are practically independent of the nuclear temperature (neglecting sophisticated descriptions, where there might be a slight reduction of the barriers with the temperature), the ratio of the yields depends on the excitation energy, or the corresponding temperature T. This dependence evolves approximately like $Y/Y' \approx exp\{-(B-B')/T\}$, where Y', Y are the yields for the most asymmetric and less asymmetric split, respectively, and B', B the corresponding barriers. This is related to the behavior of the slope of the entropy

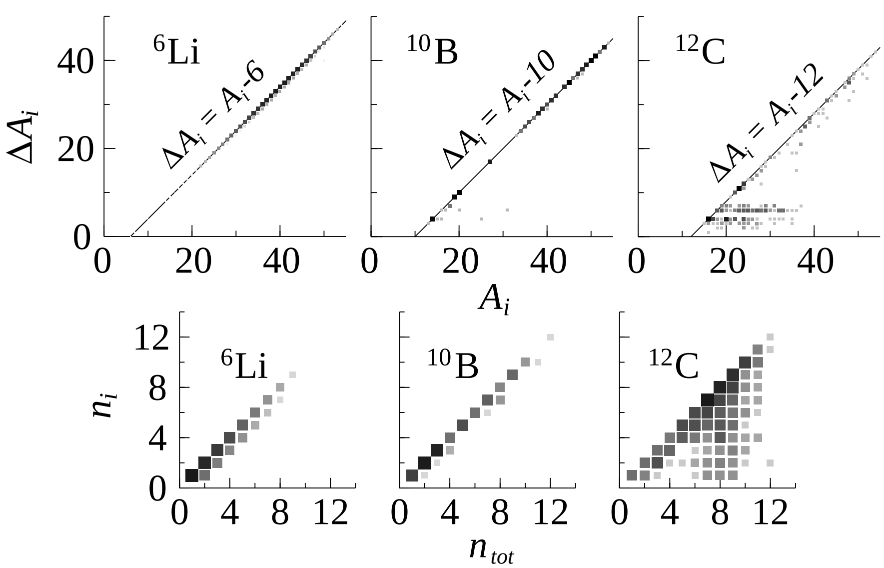

Figure 4.7: Comparison of evaporation features for ^{6}Li, ^{10}B and ^{12}C in ^{56}Fe+p as described by GEMINI. In a sequence of n_{tot} fission-evaporation steps, i denotes the step when the greatest velocity component was gained by the residue. n_i, A_i and ΔA_i are the corresponding step number,mother nucleus and mass difference between the mother and daughter nuclei, respectively. See text for details.

$S = \ln(\rho)$ (Where ρ is the compound-nucleus level density) as a function of the excitation energy E^* as a $\sqrt{E^*}$ function. This means that it is relatively more probable to emit heavier fragments at higher excitation energies. At lower energies, the emission of protons and neutrons is dominant. The emission of alpha particles plays a specific role due to the strong binding of ^4H. Therefore, the emission of alpha particles is favoured, and comparable with the emission of protons and neutrons. Over the whole binary-decay chain, the emission of intermediate-mass fragments (IMFs) is a rare process. This leads to the following scenario: The emission of IMFs occurs most probably at higher excitation energies. Following the deexcitation chain, the probability for the emission of IMFs decreases strongly with decreasing excitation energy. A second emission of an IMF is very unlikely because of two reasons: firstly, the emission of an IMF is a rare process, thus the emission of two IMFs has already this small probability squared. Secondly, the emission of a second IMF is even less probable, because the excitation energy has already decreased. In particular, within GEMINI two fragments are formed with the same temperature in a binary decay and the energy is divided according to the mass split.

The scenario that we have depicted is reproduced in fig. 4.7 and it can be resumed by the following features:

1. If an IMF is emitted, this is the only IMF in this specific deexcitation chain, with high probability.

2. This IMF is predominantly emitted at the beginning of the deexcitation chain, from a compound nucleus rather close to the hot remnant.

3. The excitation energy of the fragment is proportional to its mass. Thus, light fragments might have such low an excitation energy that they are formed below the particle-emission threshold and do not undergo any further particle emission.

4. If the emitted IMF is excited above the particle-emission threshold, it will evaporate mostly protons and neutrons further on. This will bring the nucleus near to or on the evaporation-residue corridor (near N=Z for these light nuclei).

4.2.3 Fast break-up

We imputed the underestimation of intermediate-mass fragment formation to an incomplete description of the most highly excited decaying systems when solely fission-evaporation deexcitation was considered. In this respect, we turned to the Copenhagen-Moscow statistical multifragmentation model (SMM) [Botvina 1985a, Bondorf 1995], that is the extension of the standard statistical evaporation-fission picture toward high excitation energies, treated by adding the fast simultaneous

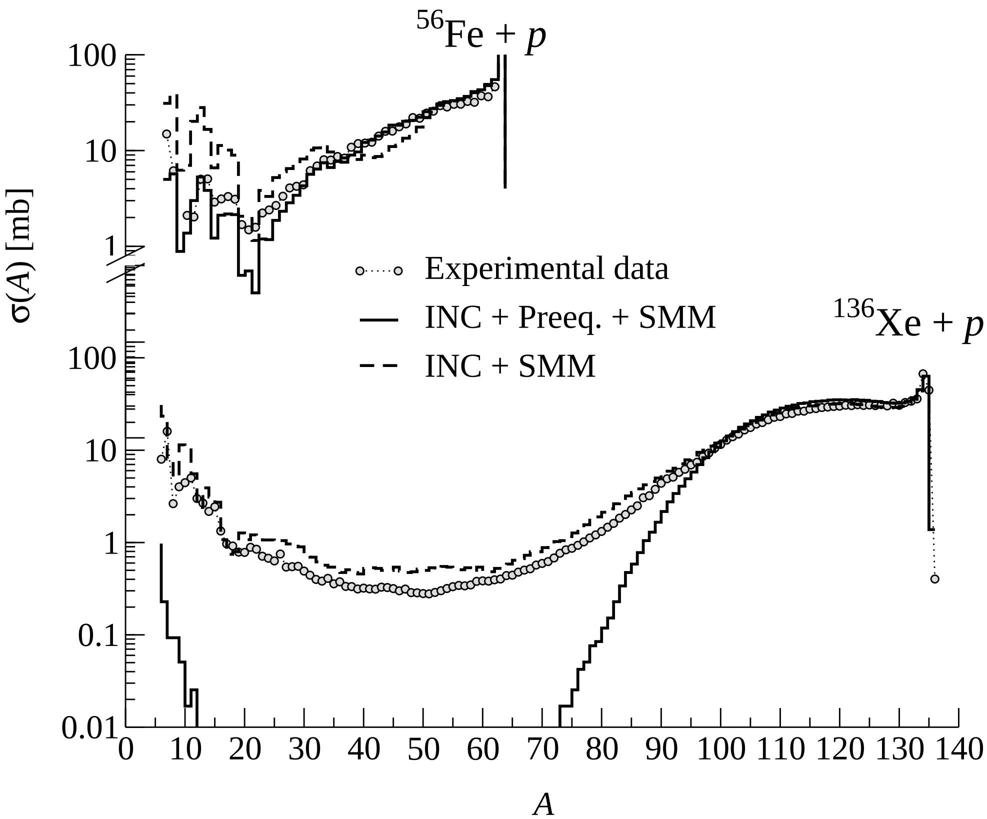

Figure 4.8: Comparison of the measured mass distributions as a function of the mass number for the systems ^{56}Fe+p and ^{136}Xe+p with the results of SMM.

disassembly of the system as a possible decay channel. The hybrid model of intranuclear cascade followed by SMM was already applied in previous studies of proton-induced reactions [Botvina 1985b, Botvina 1990] for the description of similar experimental data. In the framework of SMM, the evaporation from the compound and compound-like nuclei is included and, therefore, at low excitation energies, if the channels with production of compound-like nuclei dominate, SMM gives results similar to GEMINI. In particular, the statistical cluster evaporation is treated within the Weisskopf formalism, extended to the emission of nuclei (in their ground state or available excited states) up to ^{18}O [Botvina 1987]. On the other hand, when very high excitation energies are reached in the collision, the system is assumed to be diluted and to have attained the freeze-out density ρ_b. In previous studies [Bondorf 1985] ρ_b was calculated to evolve as a function of the excitation energy per nucleon toward an almost asymptotic value equal to 1/3 of the ground-state density ρ_0 for high excitation energies ($E^*/A > 5$ MeV). In the present calculation, an energy-dependent free volume is used to determine the probability for different break-up partitions. On the other hand, for the calculation of the Coulomb interaction among fragments the freeze-out density ρ_b is introduced as a fixed quantity, equal to the asymptotic value $\rho_b = \rho_0/3$. According to the physical picture, when the region of phase (spinodal) instability is reached, at least partial thermodynamic equilibrium is expected and the fragment formation takes place according to chaotic oscillations among different break-up configurations, from event to event. In SMM, within the total accessible phase space, a microcanonical ensemble of all break-up configurations, composed of nucleons and excited intermediate-mass fragments governs the disassembly of the hot remnant. The probability of different channels is proportional to their statistical weight. Several different break-up partitions of the

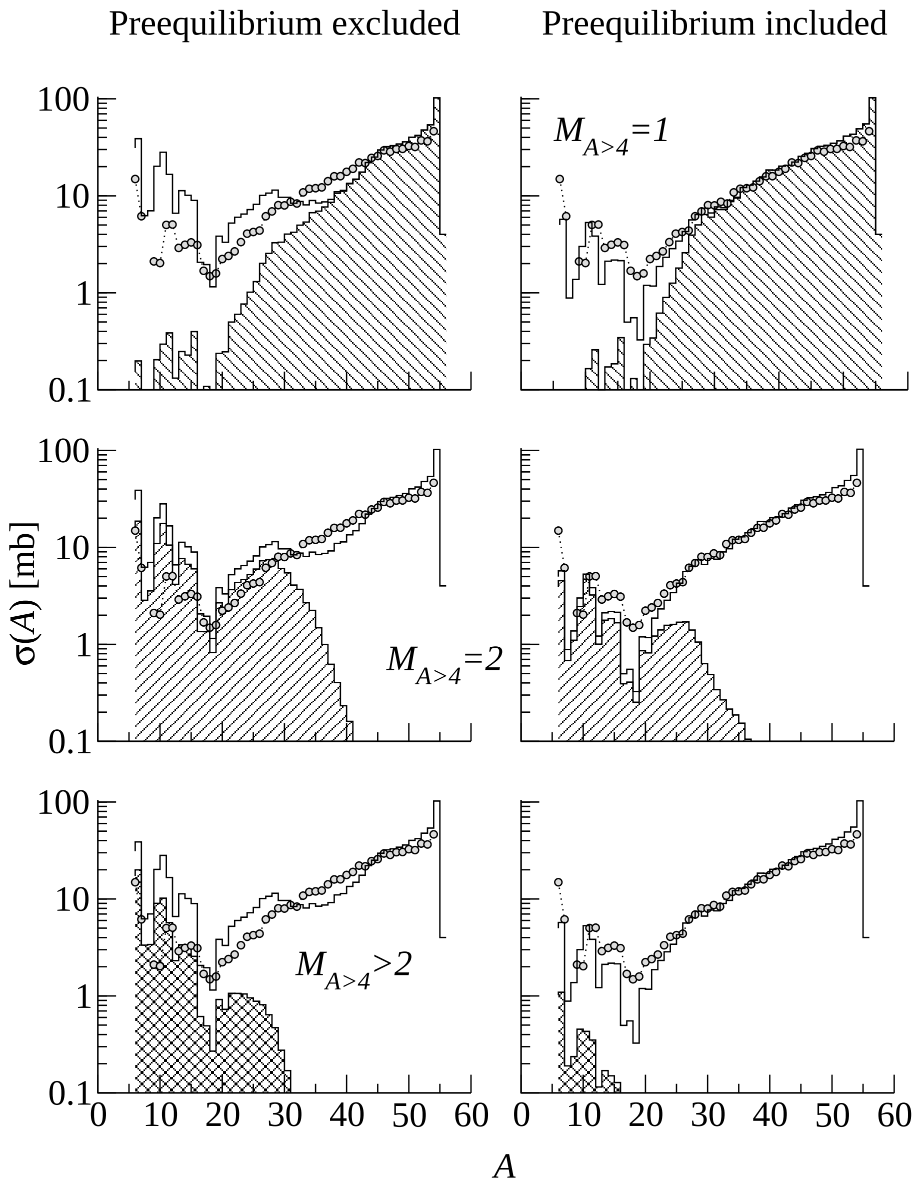

Figure 4.9: The hatched areas represent portions of the residue production calculated with SMM for the ^{56}Fe+p system, subdivided according to different multiplicities of intermediate-mass fragments (having $A>4$). The total production measured experimentally (circles) and calculated (solid line) is superimposed for comparison. The calculation disregards preequilibrium in the left diagrams and includes preequilibrium in the right diagrams.

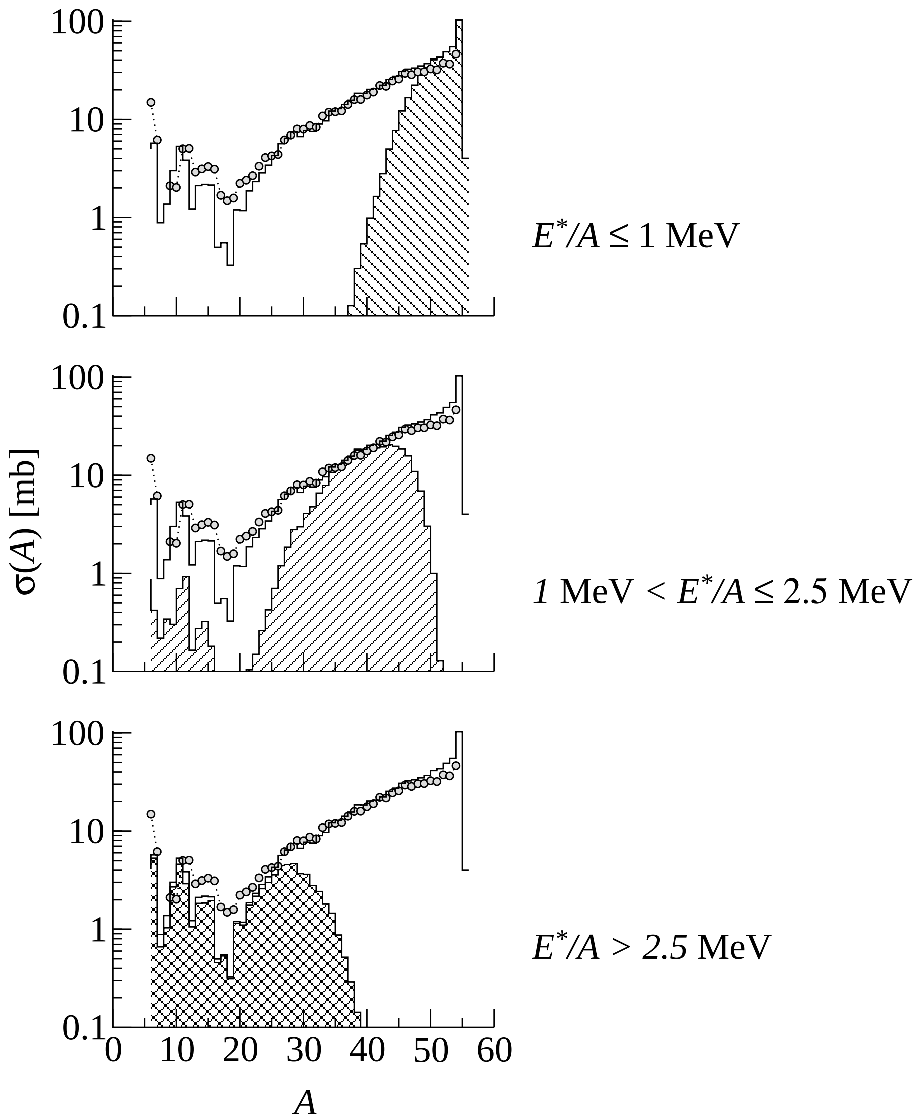

Figure 4.10: Different portions (hatched areas) of the residue production calculated with SMM for the ^{56}Fe+p system are selected according to different ranges in the excitation energy per nucleon E^*/A of the source. The calculation is performed only for the case of inclusion of preequilibrium. The total production measured experimentally (circles) and calculated (solid line) is superimposed for comparison.

system are possible.

In fig. 4.8, the calculation based on SMM reveals to better describe the reaction in comparison to GEMINI. It should also be observed that the production of intermediate-mass fragments is sensitive to the excitation energy of the source. A more detailed view on the reconstruction of the ^{56}Fe+p reaction mechanism is presented in fig. 4.9, where the multiplicities involved in the fragment formation are investigated. The major cross sections are fully determined by evaporation decays. This is true for the calculation where preequilibrium is included. On the contrary,

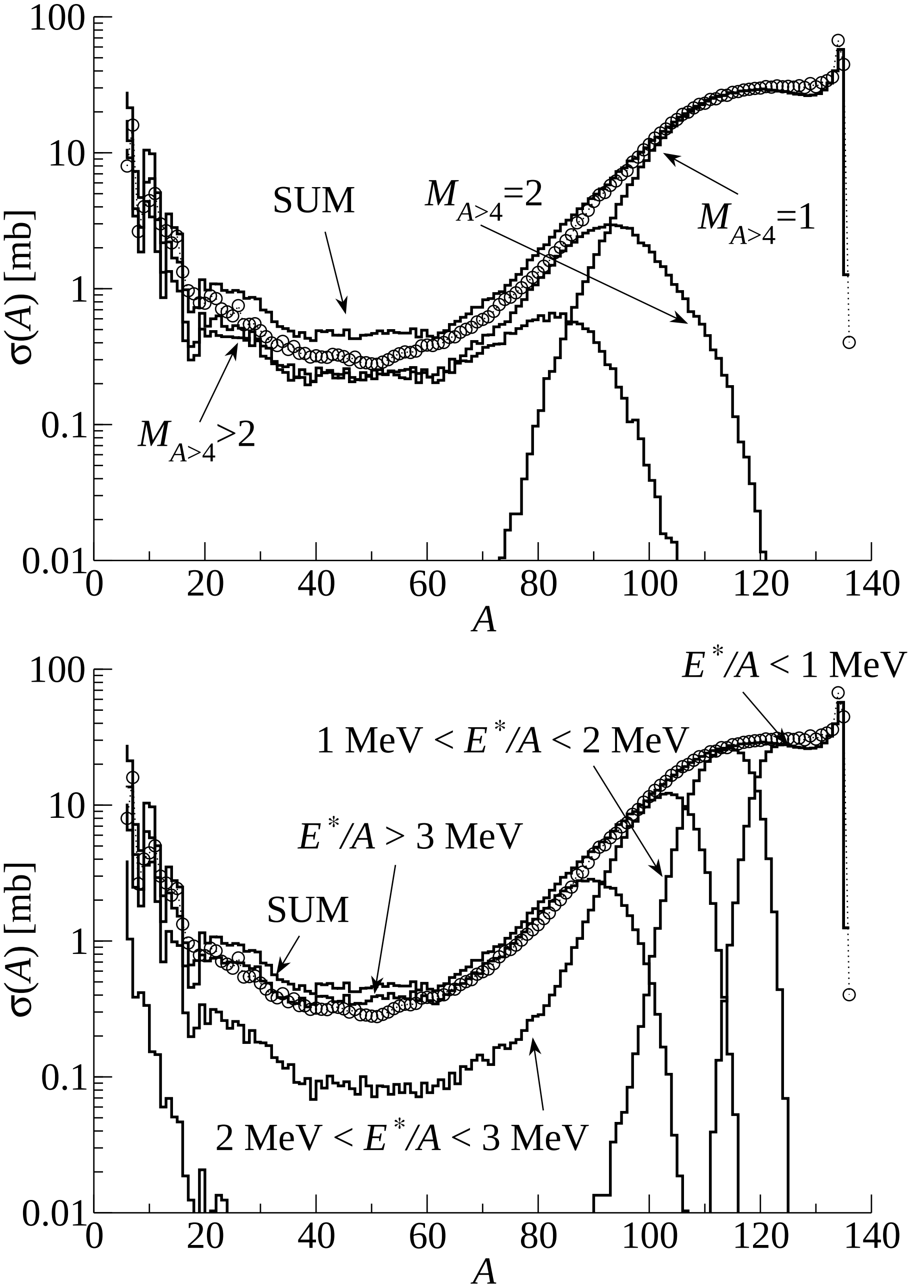

Figure 4.11: Different portions of the residue production calculated with SMM for the ^{136}Xe+p system are selected according to different multiplicities of intermediate-mass fragments having $A>4$ (top) and according to different ranges in the excitation energy per nucleon E^*/A of the source (bottom). The calculation is performed only for the case of where the preequilibrium is excluded. The total production measured experimentally (circles) and calculated (solid line) is superimposed for comparison.

when preequilibrium is excluded, a depletion of the heavy evaporation residues arises as a result of the excessive enhancement of higher-multiplicity modes (cluster emission and multifragmentation). According to the calculation, intermediate-mass fragments are almost totally produced in break-up decays where two fragments, eventually accompanied by alpha particles and nucleons are formed. We indicate these decay modes with $M_{A>4} = 2$, where $M_{A>4}$ stands for the multiplicity of fragments with $A>4$ issued of the disassembly of the hot remnant. Multifragmentation channels where three or more fragments with greater mass than alpha are formed ($M_{A>4} > 2$) have a minor contribution in the decay of the thermalised system but, when preequilibrium is disregarded, their incidence is in strong competition with lower multiplicity modes. We can extend the investigation to the excitation energies connected to the production of fragments with different masses. According to the calculation presented in fig. 4.10 for the ^{56}Fe+p system (now performed only including the preequilibrium phase), intermediate-mass fragments are almost all formed in the decay of highly excited remnants, with excitation energy per nucleon above 2.5 MeV.

The case of ^{136}Xe+p differs from ^{56}Fe+p . The mass distribution is consistently reproduced without any inclusion of preequilibrium. As discussed in section 4.2.1, its inclusion lowers the distribution of excitation energy of the hot fragments below the threshold to access any break-up decay. Similarly to fig. 4.9 and fig. 4.10, also for ^{136}Xe+p we present a calculation of the different multiplicity and excitation-energy contributions to the final production cross section: as shown in fig. 4.11, according to the calculation the production of intermediate-mass fragments is fully dominated by break-up decays with multiplicities $M_{A>4} = 2$ and $M_{A>4} > 2$ at energies exceeding about 2.5 MeV. We might remark that the experimental data are sufficiently well reproduced by adding the components $M_{A>4} = 1$ and $M_{A>4} = 2$, as it was the case for ^{56}Fe+p when preequilibrium was excluded. The further addition of the component $M_{A>4} > 2$ results in slightly too high yields. In this calculation preequilibrium was totally disregarded but the too highly populated component $M_{A>4} > 2$ might indicated that a preequilibration stage is still needed. We can conclude that a consistent description of the production of fragments could be found with the present approach, provided the modelling of the preequilibrium stage is further improved. A dynamic description, based on an expansion model, might be more appropriate.

An experimental indication of how multiplicity is related to the excitation energy is suggested by fig. 3.9 and the upper diagram of fig. 4.12, where the ratio of the sum of the individual production cross section in the two reactions ^{56}Fe+p and ^{56}Fe+$^{\mathrm{nat}}$Ti and the total cross-section ratio are compared. The latter is calculated according to the model of Karol [Karol 1975]. The production cross-section ratio scales with the total cross-section ratio only in the region of higher masses, presumably coming from more peripheral collisions, while it deviates for lighter masses. The deviation must be related to the different mean multiplicities in the two reactions: lighter masses are more populated in the ^{56}Fe+$^{\mathrm{nat}}$Ti reaction, and great part of this increase might be related to higher multiplicities. The observation of the gradual increase of multiplicity with the excitation of the system, verified in the calculation of different yield spectra associated to different energy ranges of hot remnants, could be followed further when extending to the ^{56}Fe+$^{\mathrm{nat}}$Ti reaction. As pictured in the lower plots of fig. 4.12, this behaviour is predicted by calculations with SMM. In this respect, the light-residue production characterizing the ^{56}Fe+p system might just be interpreted as the early onset of the process that will govern the decay of the ^{56}Fe+$^{\mathrm{nat}}$Ti system.

To conclude this section on model calculations, we focus once more on the velocity spectra of the light fragments shown in fig. 4.6. We already discussed the difficulty to combine the wide shapes of the velocity spectra and their mean values with a fission barrier. We inferred that the extensions of the velocity distributions to very high velocities might reflect higher kinetic energies than an asymmetric fission process could release. Consistently with this expectation, on the basis of model calculations we could connect the production of light residues to very high excitation energies of the source. Above around 2.5 MeV of excitation energy per nucleon, the process of light-residue production is still presumably dominated by binary decays, but the contribution of disintegration in more fragments is not excluded. In this case, parts of the distribution corresponding to smaller velocities should be more populated than in a purely binary split. In the representation of fig. 4.6, this contribution would fill more central parts of the spectra when lower asymmetry characterizes the break-up partition. In a statistics of events where three about-equal-size fragments are produced simultaneously, the velocity spectrum of any of

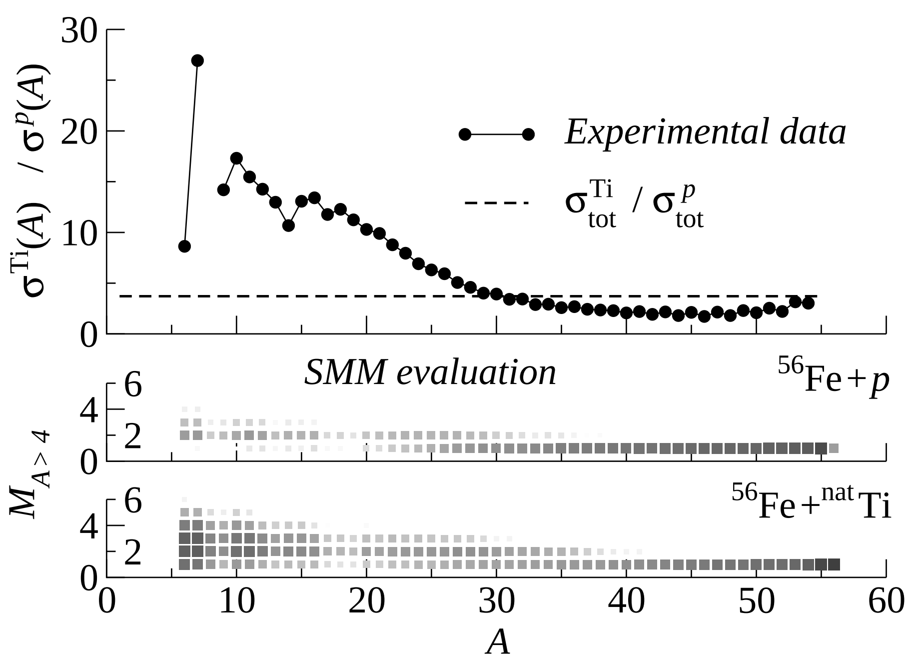

Figure 4.12: *Upper part.* Experimental data on the production cross-sections ratio as a function of the mass number for the reaction ^{56}Fe+$^{\mathrm{nat}}$Ti versus the reaction ^{56}Fe+p. The data are compared with the ratio of total nuclear cross sections for the two reactions, calculated according to the model of Karol [Karol 1975]. *Lower part.* SMM calculation of the probability for the formation of a residue as a function of the mass number and the multiplicity. The multiplicity is intended as the number of projectile-like residues heavier than an alpha particle produced in one collision.

them will be Gaussian-like. If three fragments are produced, of which two are considerably lighter than their heavy partner, the velocity spectra σ_r of the two light ejectiles will be double humped. Another contribution in populating lower velocities could be associated to different break-up configurations, where the partner or the partners of the light residue have different masses. In this case, the spectrum is the folding of several binary-like components characterized by different spacing between the two maxima and different widths around the maxima, all this resulting in the superposition of two (backward and forward) triangular-like distributions that could eventually merge in a general bell-shape. We might also consider standard evaporation cooling down the break-up residues, emitted in some excited states. In this case, the secondary "slow" emission process operates outside of the common Coulomb field of the fragmenting remnant, and would produce a general widening of the spectrum around its maxima. As portrayed in the second row of fig. 4.6, SMM describes very consistently the experimental spectra. In the third row the effect of the Coulomb interaction and eventually the expansion is illustrated by referring to the centre of mass of the system formed right after the intra-nuclear cascade and the preequilibrium, if included. SMM calculates the Coulomb interaction between fragments by placing them inside the freeze-out volume ρ_b. Contrarily to GEMINI, it takes into account different positions of the fragments, including two-body and many-body partitions. Some multifragmentation channels may resemble a two-body process even at relatively high excitation energy. These channels can also include additional small fragments which may look like evaporation ones. However, these additional small fragments can essentially change the Coulomb interaction in the volume and the thermal energy in the system, and influence the kinetic energies of the main two fragments. The binary character characterizing the experimental results is properly reproduced and the velocity distributions calculated with SMM are wider than those obtained from GEMINI. As shown in fig. 4.13, the gradual

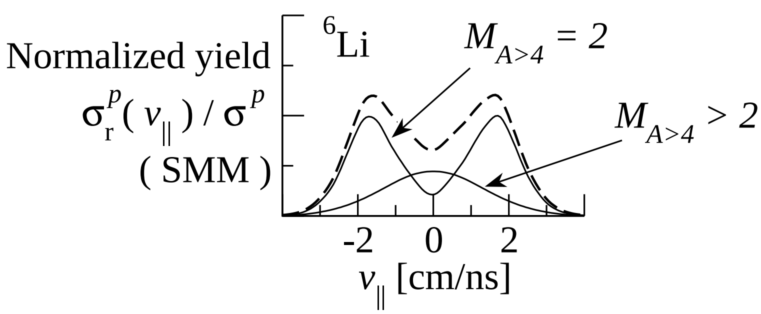

Figure 4.13: Contribution of different multiplicity channels (A>4) to the velocity spectrum of ^{6}Li produced in ^{56}Fe+p , as calculated by SMM. The representation is the same as in the second column of fig. 4.6.

filling of the centre of the spectra could be related to different break-up configurations and to possible multibody disintegration. As shown in the fig. 3.5, the decomposition of the velocity spectra in two-humped and one-humped components populating the sides and the centre of the distribution, respectively, was an experimental evidence in the ^{136}Xe+p system. In the ^{56}Fe+p system this decomposition is not experimentally observable, but it is the result of the model calculation. In the ^{56}Fe+p system, the abrupt change of shape in passing from ^{11}C to ^{12}C (correctly reproduced by SMM) might be related to the more favoured evaporation channel toward the formation of ^{12}C, that could collect several different decay processes and evaporation decays from neighboring nuclei. A specific discussion of this detail is one of the conclusions of the chapter 5 This preferential decay toward ^{12}C smears out any binary character of the spectrum. As the break-up configuration varies with the mass and the charge of the end-product, it varies also with the excitation energy available for the disassembly of the hot remnant. This was evident in fig. 4.9, where we compared the production cross sections of the residues, and it is also evident in fig. 4.6, by analysing the velocity spectra. It is evident that the suppression of the preequilibrium in the ^{56}Fe+p system induces a smearing effect on the spectra. This effect is dramatic for ^{6}Li as the double-humped spectrum is completely smeared out in one large single hump with a flat top, and it becomes similar to the velocity spectrum of ^{6}Li produced in the even more excited ^{56}Fe+ $^{\mathrm{nat}}$Ti system.

Chapter 5

Structural effects in the nuclide distribution of the residues of highly excited systems

Contents

5.1 A schematic explanation 78

5.2 Reflection of the nuclear-structure effects in the emission velocity spectra. 79

Nuclear structure is extensively studied in relation to mean-field properties, by analyzing nuclear masses, binding energies, shell effects or deformation. Additional insight on nuclear structure is carried by other frequently investigated observables; among these are the yields of the residues in low-energy fission. In this case, the fragment distribution reveals an enhanced production of the even elements, which gradually vanishes with increasing reaction energy. The disappearance of this staggering with the excitation energy seemed to constrain the study of nuclear structure to systems with low excitation energies. Though, some experiments dedicated to different and more violent reactions, like spallation or fragmentation, revealed similar structures in the yields of the residues [Ricciardi 2004a]

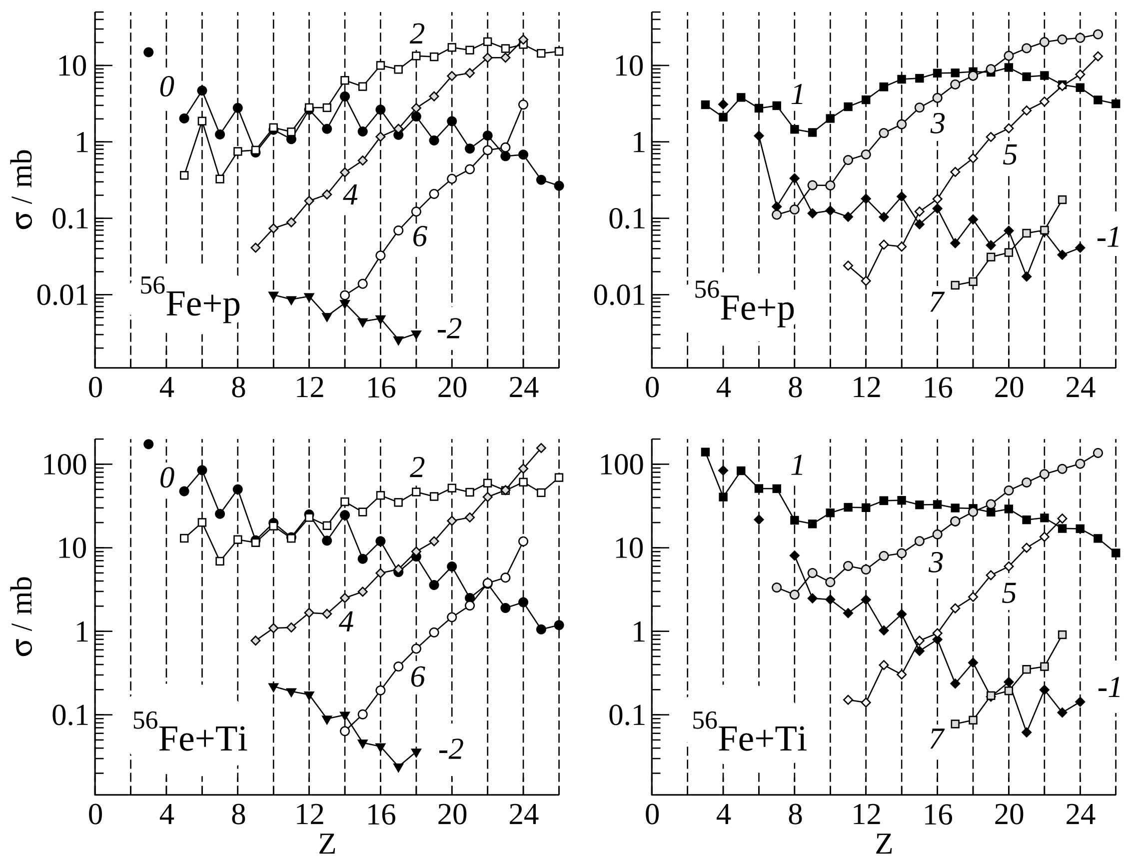

Figure 5.1: Experimental cross sections of ^{56}Fe+p (top) and ^{56}Fe+^{nat}Ti (bottom) for even-mass residues (left) and odd-mass residues (right), respectively. The cross sections are ordered in chains according to given N-Z values. The values of N-Z are marked in the figure, next to the corresponding chains.

The systems investigated in this work, ^{136}Xe+p , ^{136}Xe+$^{\mathrm{nat}}$Ti , ^{56}Fe+p , ^{56}Fe+$^{\mathrm{nat}}$Ti constitute a very complete systematics of structural effects in the isotopic distributions of highly excited systems. The residues of ^{56}Fe+p , ^{56}Fe+$^{\mathrm{nat}}$Ti are especially interesting because they extend both on the proton-rich side and on the neutron-rich side of the nuclide chart. We will therefore focus mainly on these two systems.

In fig. 5.1 the cross sections are presented ordered according to different chains of isotopes with given N-Z, for even (left) and odd (right) masses, respectively. It is evident that even-mass isotopes manifest an enhanced production of even elements all along the different chains. The staggering is maximum for symmetric nuclei (N=Z), and it gradually smooths down for more asymmetric isotopes. The case of odd masses is more complex: proton-rich isotopes (the chain N-Z=-1) show an enhanced production of even elements, while the staggering reverses in favour of an enhanced production of odd elements for neutron-rich nuclei. The ^{56}Fe+^{nat}Ti system, introducing appreciably higher excitation energy than the ^{56}Fe+p system on the average, shows higher cross sections, but identical features in the staggering along the chains of given N-Z. From this comparison, and from the extension to other measured highly excited systems (see [Ricciardi 2004a] and the collection of other systems manifesting nuclear-structure effects listed therein), we conclude that the observed structure effect does not depend on the increase of excitation energy, and it reveals to be a general property of spallation and fragmentation residues.

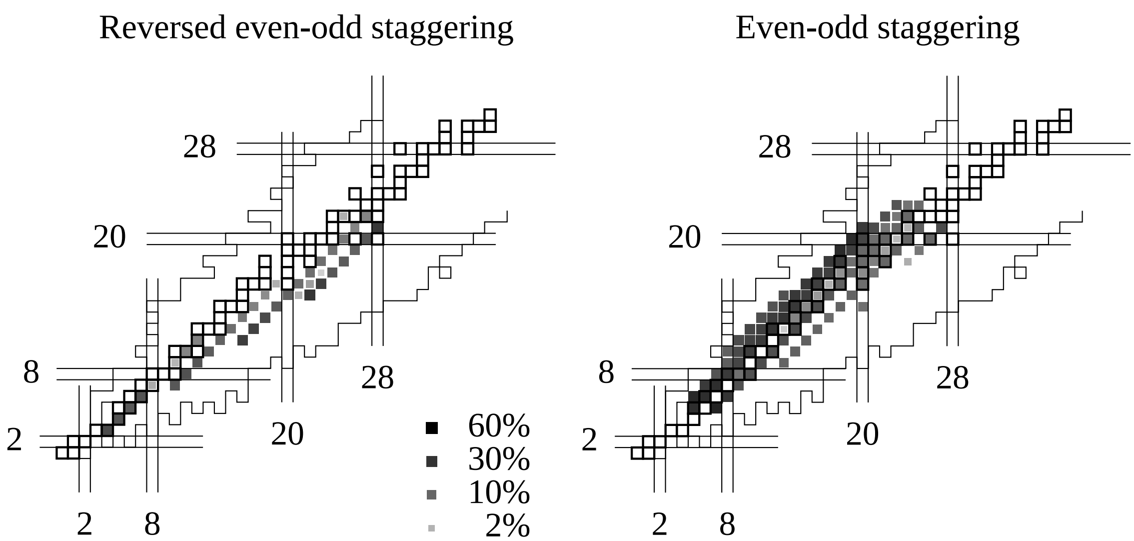

Figure 5.2: Analysis of the strength of the staggering by the formalism of Tracy, applied to chains of isotopes with given $N-Z$ values, produced in ^{56}Fe+p .

In addition, it should be pointed out that the strength of the staggering is remarkably high. As shown in fig. 5.2, a study based on Tracy's analysis [Tracy 1972] reveals a strenght higher than 50% for the even-odd staggering of the N=Z chain, and up to 20% for the odd-even staggering of the odd-mass neutron-rich nuclei. This is to be compared to the even-odd staggering that characterizes the low-energy fission yields, measured to reach a strength of around 40% at maximum [Steinhaeuser 1998]. Another interesting aspect is the much higher production of alpha-multiple nuclei (i.e. the huge staggering along the N=Z chain). This could be understood as an effect of the lower binding of odd-odd symmetric nuclei due to the effect of the Wigner term.

5.1 A schematic explanation

A simple statistical evaporation model, where the nuclear level densities are calculated according to the Fermi-gas model [Strutinski 1958] would be sufficient to reproduce all the features observed in the yields, in first order [Ricciardi 2004a]. This could seem to be in contradiction with the counterbalancing of the pairing gap in the nuclear masses and in the level densities. On the contrary, in each evaporation step, the probability of the possible decay channels does not only reflect in the level densities of the daughter nucleus, but also depend on the number of excited levels of the mother nucleus that could decay into the daughter. The excited levels available for the decay extend from the separation energy of the daughter nucleus down to the separation energy of the mother nucleus, increased of the Coulomb barrier in the case of charged-particle emission. The separation energy of the mother nucleus corresponds to the ground state of the daughter nucleus. This is sketched in fig. 5.3, where the levels of some isotopes are distributed on their mass-excess parabolae. Let us consider the case of an odd-mass nucleus decaying into an even-mass nucleus. A series of even-mass isotopes (^{30}Al, ^{30}Si, ^{30}P, ^{30}S) show a smooth

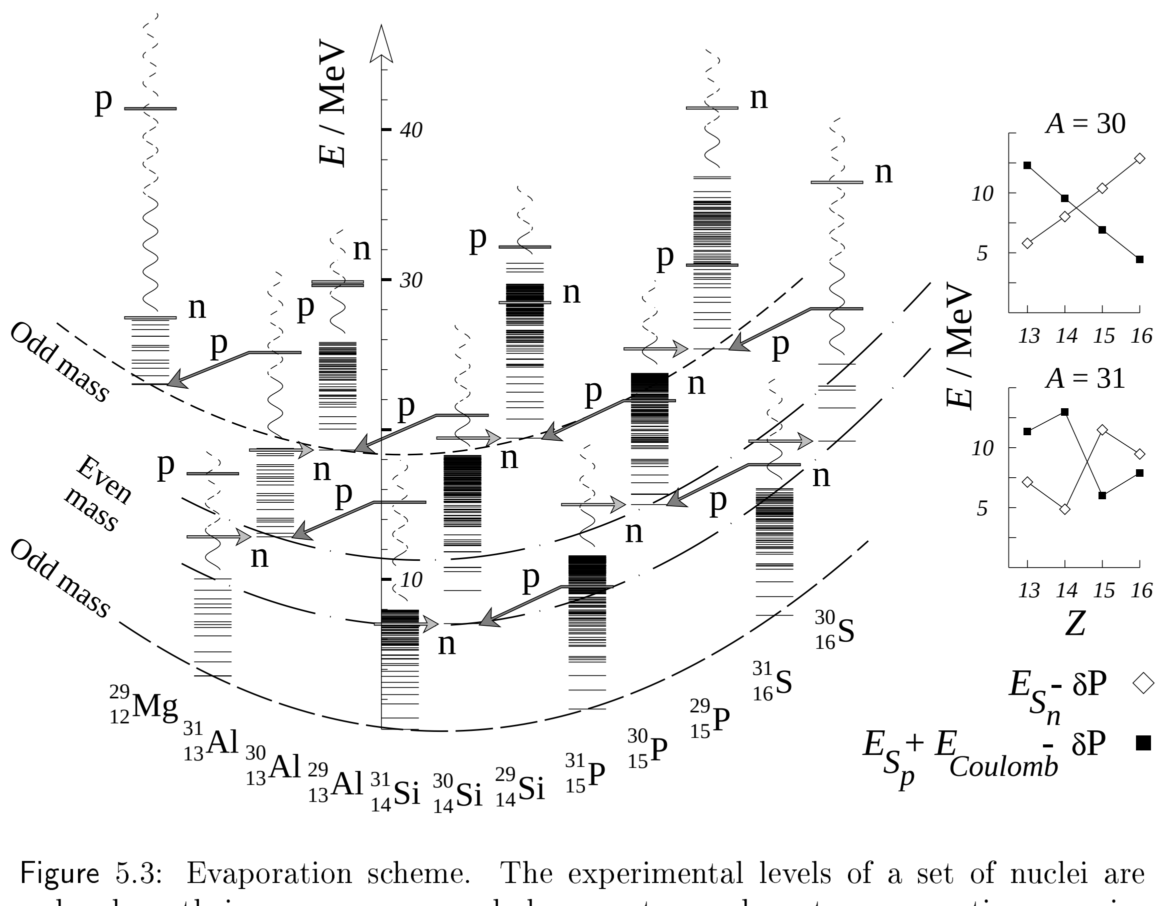

Figure 5.3: Evaporation scheme. The experimental levels of a set of nuclei are ordered on their mass-excess parabolae. proton and neutron separation energies are marked with "p" and "n", respectively. On the right, the proton (S_p) and neutron (S_n) separation energies, shifted by the pairing gap δP, are presented for $A = 30$ and $A = 31$.

variation of the separation energies as a function of the element, once shifted by the pairing gap δP. The absence of staggering in the separation energies is reflected in a smooth variation of the level density for the even-mass nuclei as a function of the element. Nevertheless, due to the pairing gap, odd-mass nuclei decaying into even-even daughters (^{30}Si or ^{30}S) have more excited levels available for the decay with respect to odd-mass nuclei decaying into odd-odd daughters (^{30}Al or ^{30}P). At the very end of the evaporation process, the decay in the ground state of the daughter nucleus becomes so relevant to determine the overproduction of even-even nuclei compared to odd-odd ones. A slightly different discussion should be dedicated to the formation of odd-mass residues (^{29}Mg, ^{29}Al, ^{29}Si, ^{29}P). As the ground states of odd-mass nuclei are all ordered along the same mass parabola, the restoring of the structure in the production yields should be determined by the separation energy that shows up as an even-odd staggering in both, proton and neutron separation energies, however with different signs, depending on the neutron excess. In odd-mass neutron-rich nuclei (^{29}Mg, ^{29}Al) the neutron separation energy, that is lower than the proton separation energy, determines the choice of the most probable evaporation channel. Thus, the residues will reflect the structure of the neutron separation energy favouring the production of odd elements. Contrarily, the yields of odd-mass proton-rich nuclei (^{29}Si, ^{29}P) reflect the structure of the proton separation energy favouring the production of even elements.

5.2 Reflection of the nuclear-structure effects in the emission velocity spectra.

The main conclusion of this chapter is that the strong nuclear-structure features manifested by the whole isotopic production is an effect of standard proton and neutron evaporation. As the restoring of nuclear-structure effects is explained by the decay on the ground state of the daughter nucleus, it should occur at the very end of the evaporation process. This implies that very few (at the limit, one) evaporation steps are enough to restore the full complexity of nuclear-structure effects. In the case of light-fragment production in ^{56}Fe+p , ^{136}Xe+p , ^{56}Fe+$^{\mathrm{nat}}$Ti , ^{136}Xe+$^{\mathrm{nat}}$Ti we excluded the possibility of a long evaporation chain involved in their formation. On the other hand, the manifestation of nuclear-structure features in the yields imposes to advocate very few, or at least one, evaporation steps following the fragment formation. We have therefore evidence that fragments issued from the disassembly of the hot remnants are formed above the particle-emission threshold. This consideration imposes that the main kinematical features, related to the shape of the velocity spectra, should not be attributed necessarily to the nuclei that we measure, but to slightly heavier fragments, which lost few nucleons after being formed. The velocity spectrum of a given isotope should therefore result from the superposition of more emission spectra related to the direct emission of the observed fragment, when formed below the particle-emission threshold, and to the emission of the heavier fragments. The contribution of nuclear-structure effects should determine the weights in this superposition. For instance, ^{11}C is less favoured than ^{12}C as an evaporation end-product. The velocity spectrum of ^{11}C formed in ^{56}Fe+p should be related almost directly to the formation of ^{11}C in the fragmentation of the hot source. If it is formed above the particle-emission threshold, it will decay further and contribute to the velocity spectra of lighter isotopes than ^{11}C. On the other hand, ^{12}C formed in ^{56}Fe+p is a preferential end-product in the evaporation and its velocity spectrum should reflect the contribution of several heavier fragments (N, O, for instance) that decayed further towards ^{12}C. Since in the ^{56}Fe+p system few mass units are enough to change the velocity spectrum from a two-humped shape to a Gaussian-like shape, few nucleon-evaporation steps should explain the difference in shape between ^{11}C and ^{12}C. In the case of ^{136}Xe+p this effect should be equally significant, but less evident in its manifestation as the spectral shapes evolve from two to one hump over a larger distribution of mass numbers.

Chapter 6

Temperature and isotopic composition

Contents

6.1 The neutron excess of the residues and the reaction mechanism . . . 82

6.2 The isospin thermometer . . . 84

6.3 Interpretation of the experimental results for the systems ^{56}Fe+p , ^{56}Fe+^{nat}Ti , ^{136}Xe+p , and ^{136}Xe+^{nat}Ti . . . 85

6.4 Calculations . . . 88

6.5 Comparison with other systems . . . 89

6.5.1 Systems with similar N/Z . . . 89

6.5.2 Systems with different N/Z . . . 91

The major results about the reaction mechanism have been investigated in the previous sections of this work, especially focusing on the light-fragment properties, like the emission velocities and the production cross sections. Due to the inclusive experimental approach, other characteristics like the fragment multiplicity and the particle correlation, are not accessible directly and we had to deduce them from model calculations. In particular, from the analysis of the light particles we could not obtain any experimental estimation of the possible temperature involved in the reaction scenario. On the other hand, by concentrating on the whole residue production, we can take advantage of the high resolution of the spectrometer in separating the masses and discuss possible relations between the isotopic properties of the residues and the thermal properties of the fragmenting system.

6.1 The neutron excess of the residues and the reaction mechanism

The collection of former data on the isotopic fragment distribution of spallation and fragmentation reactions constitutes a large survey on neutron excess of the reaction products and their connection to the excitation energy deposited in the system during the collision. As an example, fig. 6.1 offers a survey on the isotopic production obtained with different processes. We can relate the neutron excess of the reaction products to the excitation energy required for their formation. In the production measured for ^{238}U+p at 1 A GeV [Armbruster 2004] (upper nuclear chart in fig. 6.1) mainly two regions are populated. We distinguish the evaporation residues populating the proton-rich side from the projectile down to the region of lead; the ridge of the distribution extends along a path ending up in the residue-corridor [Taieb03]. The rest of the production is dominated by fission; the fission production can be still decomposed in two overlapping components [Bernas 2002]. The main production is related to high-energy symmetric fission and results in mostly neutron-rich nuclides. Even more neutron rich are the isotopes formed in asymmetric low-energy fission. Also in the system ^{238}U+^{208}Pb at 1 A GeV [Enqvist 1999] the high-energy fission and the low-energy fission, the latter electromagnetic induced, can be identified (see central nuclear chart in fig. 6.1). In addition, it was possible to disentangle the fragmentation production from fission by analysing the velocity spectral shapes (method firstly proposed by T. Enqvist [Enqvist 1999]). The former component is presented in the lower nuclear chart in fig. 6.1. The examination of the fragmentation production indicates clearly that the isotopic composition evolves with the impact parameter. More peripheral collisions form residues aligned along the residue corridor, in the proton rich side of the nuclide distribution. The initial steps of the chain of sequential decays favours high neutron emission, and the mean value of the isotopic composition $\langle N\rangle/Z$ drops. When the excitation energy available for the evaporation process is sufficiently large, the chain of decays extends far enough so that proton and neutron emission have similar probability ($\mathrm{d}N/\mathrm{d}Z = \langle\Gamma_n/\Gamma_p\rangle$ [Charity 1998], where Γ_n and Γ_p are neutron and proton decay widths, respectively) and the residue corridor is reached. On the contrary, less peripheral collisions produce fragments in regions closer to the β-stability line (i.e. the stationary point for the binding energy $B(Z)$ for A fixed, $\mathrm{d}B(Z)/\mathrm{d}Z\mid_A = 0$), much more neutron rich than the residue corridor. It should be observed that, within the picture of an only-sequential evaporation process, smaller impact parameters, related to more violent

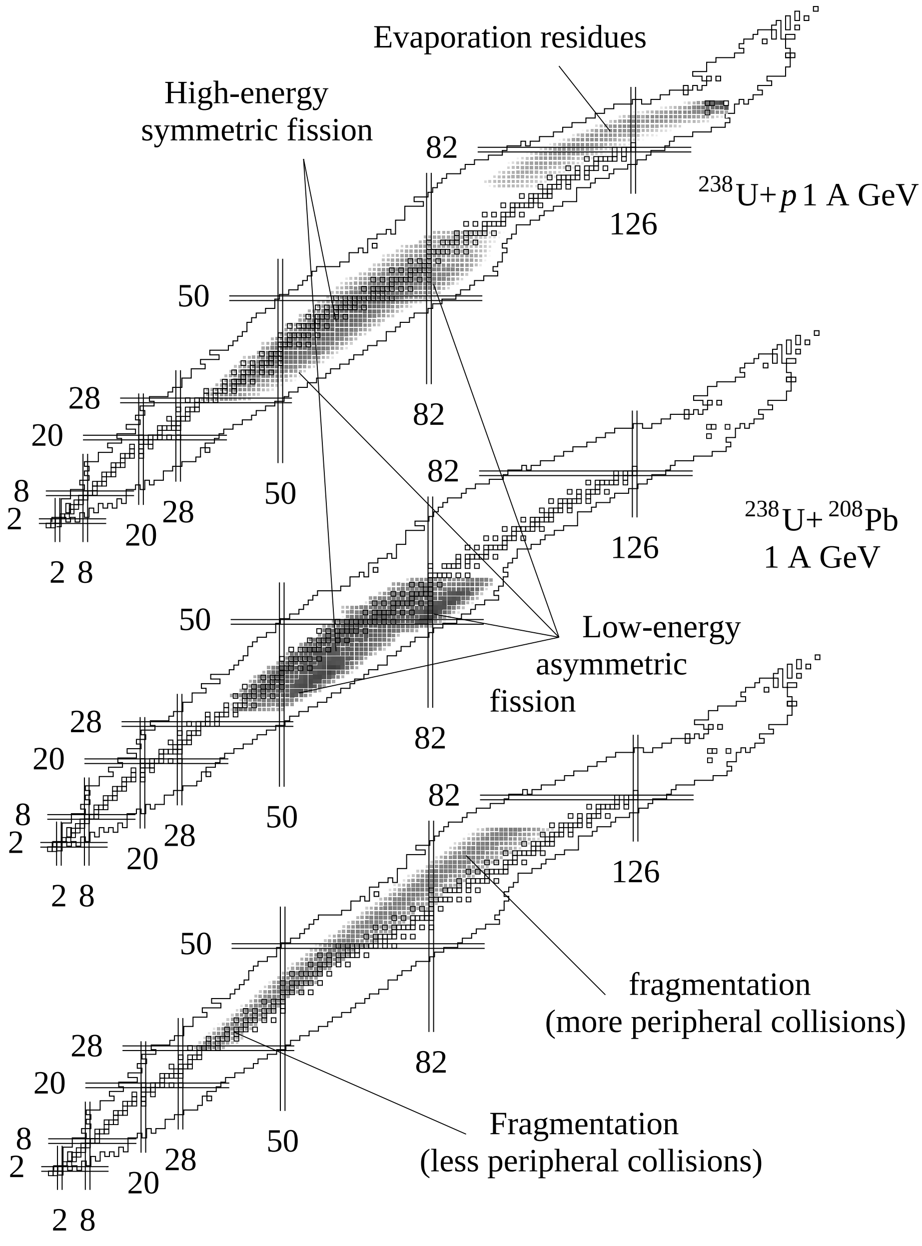

Figure 6.1: Isotopic production presented in nuclear charts for the systems ^{238}U $+p$ at 1 A GeV [Armbruster 2004, Bernas 2002, Taieb03] (top) and ^{238}U+^{208}Pb at 1 A GeV [Enqvist 1999] (centre and bottom). Regions associated to specific reactions are indicated.

collisions, should be related to a longer path towards the residue corridor (as far as it is not reaches) or along the residue corridor (when it is reached). The deviation from the residue corridor towards the β-stability, in favour of more neutron-rich isotopes would be in disagreement with this picture. The crossing of β-stability, as a result of the evolution of the isotopic composition along the evaporation chain would not even be possible. Nevertheless, fragmentation data related to peripheral collisions populating the neutron-rich side with respect to the β-stability were recently measured. The first data showing this feature were measured by V. Ricciardi for the reaction $^{238}\mathrm{U} + ^{\mathrm{Nat}}Ti$ at 1 A GeV [Ricciardi 2004b].

6.2 The isospin thermometer

In peripheral collisions, a deviation from the evaporation corridor for lighter elements was interpreted as a signature of multifragmentation decays [Schmidt 2002, Napolitani 2002a]. The multibody disassembly is in fact a very endothermic process and the excitation energy per nucleon of the fragments is necessarily smaller than the one introduced during the collision. The hot nucleus (A_0, Z_0), formed in the first fast stage of the reaction (the Abrasion or the intranuclear cascade) could break up according to several possible partitions [Bondorf 1995], consisting of more fragments (A, Z) characterized by the corresponding multiplicity. The energy E_f of a partition f is a function of the temperature T and the volume V of the system, and is equal to the total energy of the initial nuclear system E_0, reduced by the amount of energy E_0^{rot} spent in the rotational motion of the system. If we indicate by E_0^* and $E_0^{\mathrm{g.s.}}$ the excitation energy and the ground-state energy of the initial nuclear system, respectively, we can write

$$E_0 - E_0^{\mathrm{rot}} = E_0^*(T,V) + E_0^{\mathrm{g.s.}} = E_f(T,V) \quad . \tag{6.1}$$

The energy E_f is then distributed among the internal energy of the fragments $E_{A,Z}^{\mathrm{int}}(T^2,V)$, the clusterization energy $E_{A,Z}^{\mathrm{clu}}(V)$, the rotational energy $E_{A,Z}^{\mathrm{rot}}(T,V)$, the transitional energy $E_{A,Z}^{\mathrm{tr}}(T,V)$, and the total Coulomb energy $E_f^{\mathrm{C}}(V)$ (averaged over all possible fragment positions in the volume of the breaking-up system) so that

$$\begin{aligned} E_f(T,V) &= \sum_f E_{A,Z}^{\mathrm{tr}}(T,V) + \sum_f E_{A,Z}^{\mathrm{rot}}(T,V) + \sum_f E_{A,Z}^{\mathrm{int}}(T^2,V) \\ &+ \sum_f E_{A,Z}^{\mathrm{clu}}(V) + \sum_f E_{A,Z}^{\mathrm{g.s.}} + E_f^{\mathrm{C}}(V) \quad , \end{aligned} \tag{6.2}$$

where $\sum_f$ is the sum extended over all fragments (A, Z), considering their multiplicity $N_{A,Z}$. The excitation energy of one fragment (A, Z) issued from the break-up is

$$E_{A,Z}^*(T,V) = E_{A,Z}^{\mathrm{int}}(T^2,V) + E_{A,Z}^{\mathrm{clu}}(V) \quad , \tag{6.3}$$

Evidently, the excitation energy $E^*_{A,Z}(T,V)$ can be considerably smaller than $E^*_0(T,V)$. The difference of energy $E^*_0(T,V) - E^*_{A,Z}(T,V)$ explains the important reduction in the excitation energy available for the sequential-evaporation decay. It should be observed that it is no more possible to deduce any thermal characteristic of the initial system from those residues ending up in the residue corridor. On the other hand, when the condition $\mathrm{d}N/\mathrm{d}Z = \langle\Gamma_n/\Gamma_p\rangle$ is not reached, it is possible to easily trace back the sequential-evaporation process, provided that the isotopic composition $\langle N\rangle/Z$ of the hot residues is known. A good assumption is to impose that the isotopic composition of the hot fragments coincides with the one of the projectile. Both the fast stage of the collision (Abrasion or intranuclear cascade) and the break-up phase is not expected to change the isotopic composition remarkably [Botvina 2001]. The same temperature T is related to both the quantities $E^*_0(T,V)$ and $E^*_{A,Z}(T,V)$. Therefore, if we are able to deduce from the measured residue productions the distribution of excitation energies $E^*_{A,Z}(T,V)$, charges Z and masses A of the hot fragments, we have a tool to determine the nuclear temperature T. This concept was introduced by K-.H.Schmidt and M.V. Ricciardi and named *isospin thermometer* [Schmidt 2002, Ricciardi 2004b]. It inspired a recent experiment [Napolitani 2001b] and is now in course of study in a dedicated work [Henzlova 2004].

6.3 Interpretation of the experimental results for the systems ^{56}Fe+p , ^{56}Fe+$^{\mathrm{nat}}$Ti , ^{136}Xe+p , and ^{136}Xe+$^{\mathrm{nat}}$Ti .

In fig. 6.2 we study the evolution of the mean neutron-number-to-charge ratio as a function of the element for all the systems analyzed in this work, ^{56}Fe+p, ^{56}Fe+$^{\mathrm{nat}}$Ti, ^{136}Xe+p, ^{136}Xe+$^{\mathrm{nat}}$Ti. In the region of charges close to the projectile, the proton-induced reactions result in slightly less neutron-rich residues. This effect is due to the higher efficiency of the intranuclear cascade driven by protons in heating up the system with respect to the titanium-induced abrasion. This side of the spectra, that we could refer to as the “main evaporation path”, is mostly related to heavy prefragments that decayed by solely evaporation from a compound nucleus (without experiencing any break-up), and is directed towards the residue corridor. The latter is not reached if the initial system is too neutron rich, as it is evident for ^{136}Xe, and not enough energy is invested in the evaporation channel due to the competition with multibody decay. A major experimental result is the general complete overlap between the proton-induced reaction products and the titanium-induced reaction products in the intermediate-mass region, far away from the evaporation corridor. Especially in the middle of the Z-distribution (see ^{136}Xe data, fragments from P to Zr) the data-points coincide. The deviation from the evaporation corridor is so large that even the β-stability line is crossed, and the lightest residues are neutron rich in average and not proton rich as it would result from a long evaporative sequence.

We interprete this side of the spectrum as a signature of the endo-thermical multifragmentation process that has the effect of disintegrating the system in a large distribution of hot fragments, from which several evaporation paths depart. These paths can not reach the evaporation corridor due to the loss of energy spent in the initial disassembly and they all end up on a "breakup-evaporation edge". The breakup-evaporation edges related to equal projectiles (^{136}Xe or ^{56}Fe) are indistinguishable: This very new experimental finding is an indication that in the 1

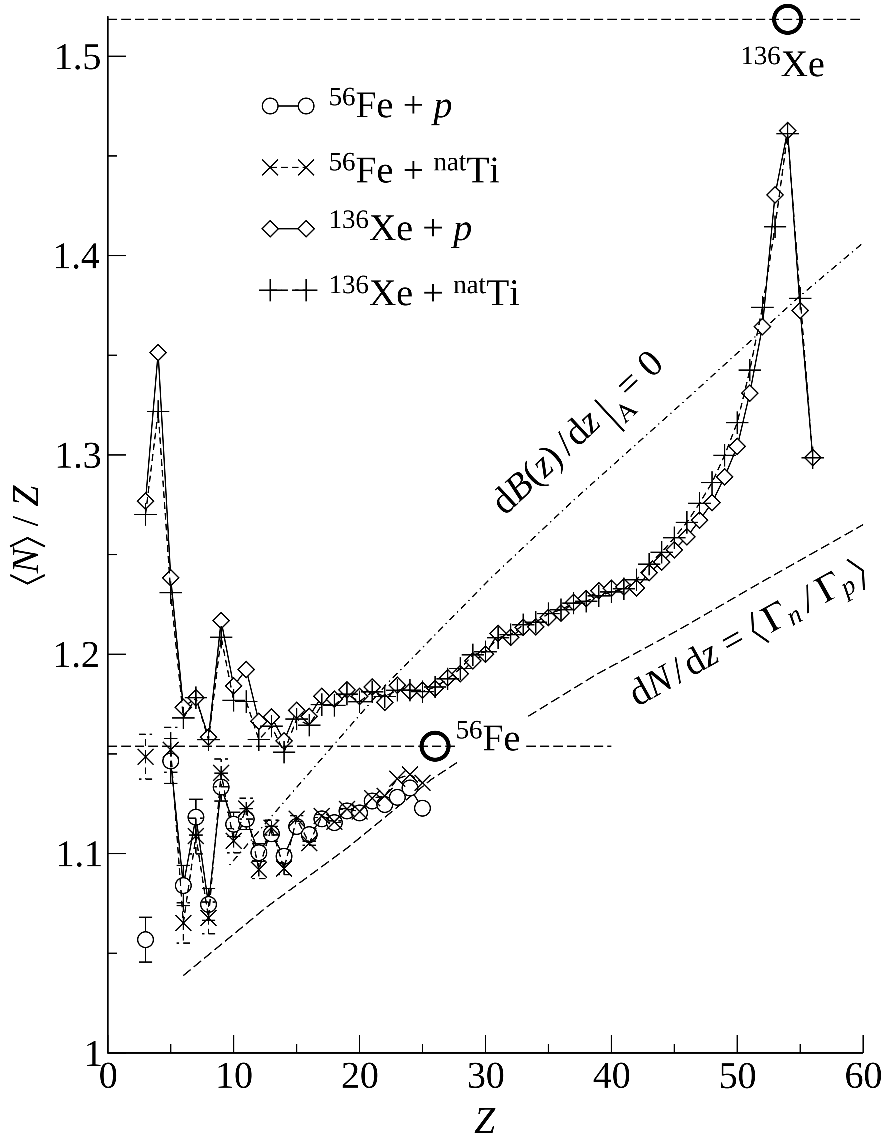

Figure 6.2: Experimental mean isotopic component measured for ^{56}Fe+p , ^{56}Fe+$^{\rm nat}$Ti , ^{136}Xe+p , and ^{136}Xe+$^{\rm nat}$Ti . The horizontal dashed lines indicate the N/Z value of ^{56}Fe and ^{136}Xe . The dot-dashed curve indicates the β-stability ($\mathrm{d}B(Z)/\mathrm{d}Z \ |_A = 0$). The dashed curve indicates the residue corridor ($\mathrm{d}N/\mathrm{d}Z = \langle \Gamma_n/\Gamma_p \rangle$).

A GeV incident-energy range the break-up process operates identically independently on the entrance channel, for both the peripheral ion-ion collisions and for p-induced reactions. In particular, we can expect that the mean excitation energies $E^*_{A,Z}$ of the hot fragments are almost identic for the ^{136}Xe+p and ^{136}Xe+$^{\mathrm{nat}}$Ti (or ^{56}Fe+p and ^{56}Fe+$^{\mathrm{nat}}$Ti) systems. On the contrary, the two types or reactions are considerably different: mass and charge distribution of the fragments (A, Z) are different, as we conclude from the experimental mass spectra. Reasoning in terms of a multifragmentation scenario, we could deduce that the partitions f are selected according to different distributions of probabilities in the ^{136}Xe+p and ^{136}Xe+$^{\mathrm{nat}}$Ti (or ^{56}Fe+$^{\mathrm{nat}}$Ti and ^{56}Fe+p): the difference in the more probable partitions is reflected in the fragment multiplicity and, therefore, in the mass spectra, but not in the mean isotopic component of the distribution. It is evident that we are supposing the possibility to extend the multifragmentation process to cases where large asymmetries are present in the configuration of the break-up partition. We already came to such a conclusion as a result of our study on invariant cross sections in chapter 4, where we investigated the emission kinematics involved in the formation of light fragments. In that framework we concluded that proton-induced collisions in the 1 A GeV incident energy range can induce an asymmetric split of the hot remnant, where one heavy fragment is produced together with fragments of considerably smaller sizes. According to this interpretation, the heavy residues in the P-to-Zr range produced in the ^{136}Xe+p reaction would therefore coincide with the heavy partner advocated for explaining the spectral shapes of the emission velocities of the light fragments. The similarities with the ^{136}Xe+$^{\mathrm{nat}}$Ti system with respect to the isotopic composition of the residues induces us to extend the same conclusion to peripheral ion-ion relativistic collisions. We could expect that at relativistic energies peripheral ion-ion collisions and proton-ion collisions lead to the same kind of deexcitation process, where the nucleus disassembles in more pieces according to an asymmetric partition. In ^{136}Xe+$^{\mathrm{nat}}$Ti and ^{56}Fe+$^{\mathrm{nat}}$Ti systems peripheral collisions seem in fact to coincide with the main features of the systems ^{136}Xe+p and ^{56}Fe+p. Nevertheless, in ^{136}Xe+$^{\mathrm{nat}}$Ti and ^{56}Fe+$^{\mathrm{nat}}$Ti also smaller impact parameters contribute to the final production and the difference between the two systems should result mainly in the total amount of thermal energy introduced in the system. This is reflected in the mass distribution (or, more precisely, in the magnitude but not in the shape of the mass distribution, that is similar for the two systems) and in the shape of the emission-velocity distributions (or in the fragment multiplicity).

It should be remarked that recent theoretical investigations [Nörenberg 2002] do not consider very asymmetric partitions as favoured channels. Fragmentation resulting from bulk instability is expected to be driven by density waves, the modes of which (a calculation was proposed by Norenberg [Nörenberg 2002]) should favour the formation of almost-equal-size fragments. This kind of instability is anyhow not accessible at our excitation energies (hot spherical nuclei formation driven by bulk instability occurs at around $T \gtrsim 9$ MeV) and it is mostly related to compression. Multifragmentation resulting from surface instability is accessible at our energy range, but it leads mainly to quadrupole deformations, resulting in symmetric-fission-like splits.

6.4 Calculations

We do not go into the details of the reaction dynamics and the nature of the instability involved. We rather make one additional effort to deduce, on a purely statistical basis, one more characteristic: the nuclear temperature T involved in the disassembly of the hot remnant. For this purpose we rely on the *isospin-thermometer* method, by tuning the temperature T of the break-up partitions $f(T, V)$, in order to reproduce the correct $\langle N \rangle / Z$ distribution [Schmidt 2002].

A simple approach is to introduce a "temperature threshold" in a complete abrasion-ablation code [Gaimard 1991]. The hot fragment distribution is calculated in the abrasion stage. We obtain a distribution of sources with different excitation energies. We can impose that when the temperature deduced by the compound-nucleus excitation energy exceeds 5 MeV, the source splits in fragments of smaller size with

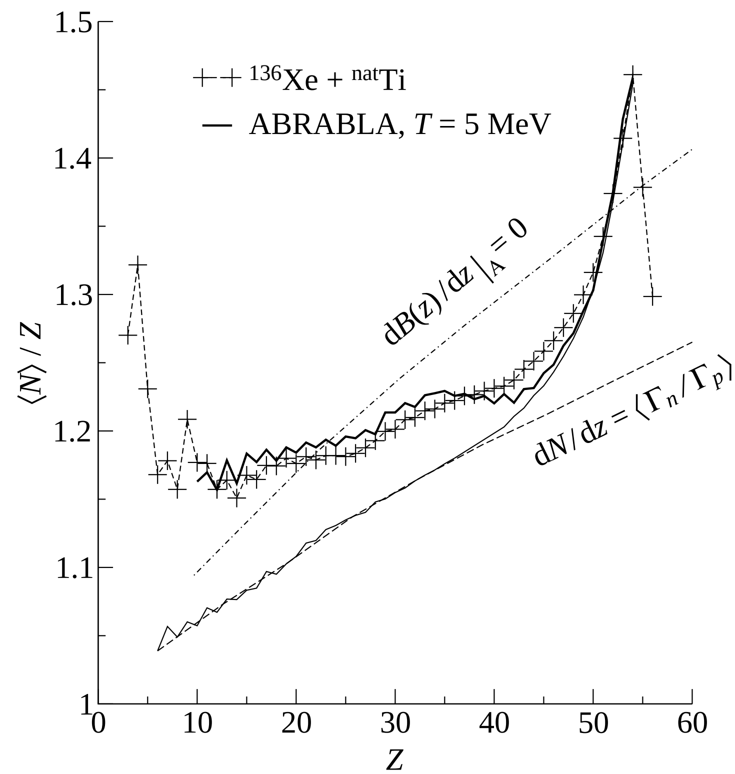

Figure 6.3: Experimental data of ^{136}Xe+^{nat}Ti compared with a calculation performed with ABRABLA [Gaimard 1991] by imposing a temperature threshold at 5 MeV, in correspondence of which the hot nucleus decomposes in smaller fragments. The fragments successively decay from an initial excitation energy equal to 5 MeV. The thin solid line merging with the residue corridor is an ABRABLA calculation evaluated excluding any temperature threshold and by imposing solely proton and neutron emission from a distribution of abrasion fragments, calculated for ^{136}Xe+^{nat}Ti at 1 A GeV. Dashed and dashed-dotted lines are defined in fig. 6.2.

the condition of keeping constant the mean isotopic composition. Fragments form at a temperature of 5 MeV. The choice of the partition configuration is treated on the basis of a parametrization optimized in order to reproduce the residue cross section with correct magnitude. However, as we remarked above, the partition configuration does not influence the $\langle N\rangle/Z$ observable. This calculation should be intended as a test for a possible characteristic temperature of the break-up process.

The result is remarkably promising and it is shown in fig. 6.3, where we see that the inclusion of a temperature threshold has the effect of increasing the $\langle N\rangle/Z$ of the residues and producing a deviation from the distribution obtained with a purely-evaporative-decay model. These calculations add one more information to our picture: the possible presence of a characteristic temperature as a main feature ruling the whole nuclide production. This is evident from the proper reproduction of the experimental $\langle N\rangle/Z$ spectrum when equal temperature is imposed as an initial condition for the evaporation of all break-up fragments, independently of their size. This was also a major conclusion of similar calculations dedicated to the study of the ^{238}U+^{208}Pb system [Schmidt 2002, Napolitani 2002a].

6.5 Comparison with other systems

6.5.1 Systems with similar N/Z

From the previous examination of experimental results we found that the observable we study, the isotopic-composition along the breakup-evaporation edge is independent of the mass and charge distribution of the fragments (A, Z), of the fragment multiplicity and of the impact parameter (at relativistic incident energies). As confirmed by the previous calculations, it depends exclusively on the initial temperature T of the fragmenting system and on its isotopic composition $\langle N\rangle/Z$. The latter statement can be reinforced by comparing the $\langle N\rangle/Z$ spectrum obtained for ^{136}Xe+p and ^{136}Xe+^{nat}Ti with previous experimental data, measured for systems with similar isotopic composition. It is therefore tempting to build up a collection of different systems, all characterized by similar N/Z. Fortunately, previous experiments exist, where a ^{208}Pb projectile was measured (^{208}Pb is only slightly more neutron rich than ^{136}Xe).

As shown in fig. 6.4, the data of ^{208}Pb+p [Enqvist 2001b] overlap with the data of ^{208}Pb+d [Enqvist 2001a], that overlap with the data of ^{208}Pb+^{nat}Ti [Enqvist 2001b], and the latter overlap consistently with the new data of ^{136}Xe+p and ^{136}Xe+^{nat}Ti. Systems with different mass and equal N/Z differ only for the main evaporation path. All main evaporation paths converge to a single breakup-evaporation edge like rivers reaching the coast. The characteristic of the main evaporation paths (the rivers!) is that two successive evaporation steps could lie on the same path. For instance, the evaporation corridor has the same characteristic. On the contrary, the breakup-evaporation edge (the coast!) is the average of all the final steps of all evaporation paths. We interpret the overlap of the breakup-evaporation edges as another manifestation of the same physics characterizing the plateau of the caloric curve. This reflects the existence of an apparently identic temperature driving the liquid-gas phase transition in the ^{136}Xe+p and ^{136}Xe+$^{\mathrm{nat}}$Ti (or ^{56}Fe+p and ^{56}Fe+$^{\mathrm{nat}}$Ti) systems.

In fig. 6.4 we can also appreciate the excellent agreement with a calculation. An homogeneous distribution of hot fragments with average isotopic composition equal to the one of ^{136}Xe is extended over the mass range $10 < A < 100$. This distribution crudely simulates the hot fragment produced after the disassembly of any system with the same $\langle N \rangle / Z$ of ^{136}Xe. These fragments are let decay by

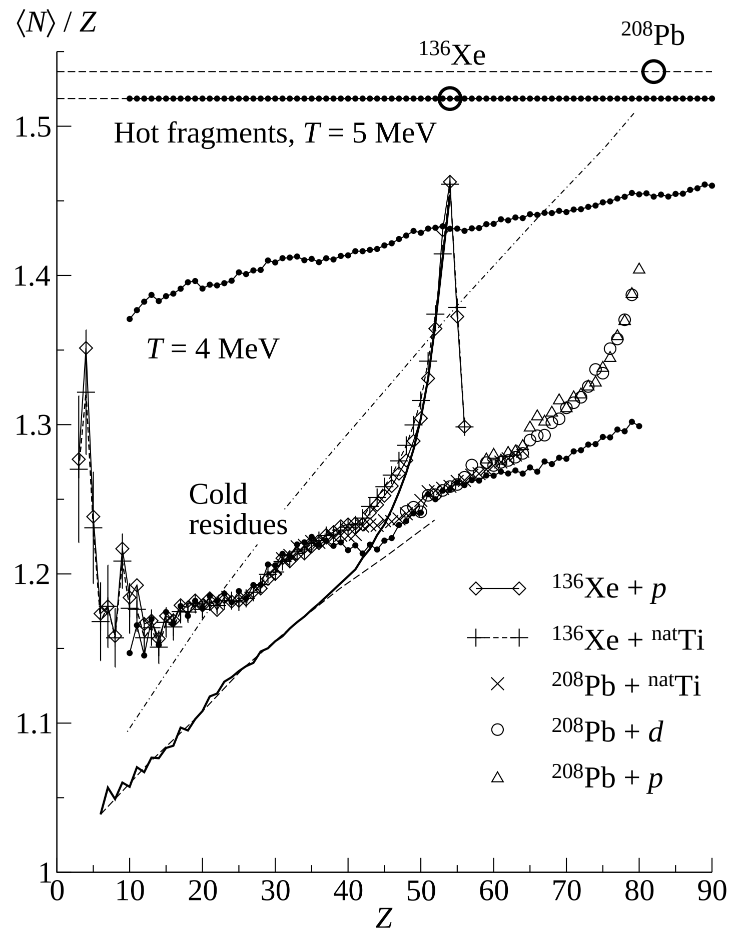

Figure 6.4: Experimental data of ^{136}Xe+$^{\mathrm{nat}}$Ti and ^{136}Xe+p compared with previous measurements: ^{208}Pb+p [Enqvist 2001b], ^{208}Pb+d [Enqvist 2001a], ^{208}Pb+$^{\mathrm{nat}}$Ti [Enqvist 2001b]. Three stages of a calculation are overlapped: the inial hot-fragment distribution ($T = 5$)MeV, intermediate evaporation stages for $T = 4$, and breakup-evaporation edge for the final nuclides. The β-stability and residue corridor are indicated as in fig. 6.2.

solely evaporation from an initial temperature of 5 MeV. The evaporation process is treated including consistently the nuclear structure effects, such as pairing and shell effects [Gaimard 1991, Junghans 1998]. we observe the emerging of shell and pairing effects (the latter characterized by a favoured evaporation towards even elements in average) in the final distribution, that lands correctly on the measured breakup-evaporation edge for the $\langle N \rangle / Z$ of ^{136}Xe$\sim^{208}$Pb. This result seem to be rather consistent with other measurements of the plateau of nuclear caloric curves [Natowitz 2002]. It should be remarked that, even if the limiting temperature is expected to vary with the mass of the breaking system, this variation is large only for the lightest masses ($A < 60$ [Natowitz 2002]).

6.5.2 Systems with different N/Z

As shown in fig. 6.5, other data were collected for projectiles with different $\langle N \rangle / Z$. Unfortunately, they are all rather difficult to exploit. ^{56}Fe is too light and dominated by nuclear-structure effects. ^{129}Xe [Reinhold 1998] was very accutately measured, but only along the initial part of the main evaporation path, ^{86}Kr [Weber 1992] was measured with too large uncertainty (not shown in fig. 6.5) as it was one of the first experiments at the FRagment Separator. Finally, only ^{238}U has been measured completely but still, due to the strong competition with fission, the procedure of disentangling the fragmentation component introduced some scattering in the data points, and the proximity of the isotopic composition of ^{238}U and ^{208}Pb results in a doubtful comparison. A clear understanding will come from the study of a proton-rich isotope like ^{124}Xe, that was recently measured and is now being analyzed [Henzlova].

The general impression that we deduce from the whole collection of data is that different breakup-evaporation edges exist as a function of the isotopic composition of different projectiles. In fig. 6.5 the lines serve only to guide the eyes. (The line marking ^{136}Xe -^{208}Pb was fitted to the experimental breakup-evaporation edge. The others lines are simply scaled with respect to the ^{136}Xe -^{208}Pb -line).

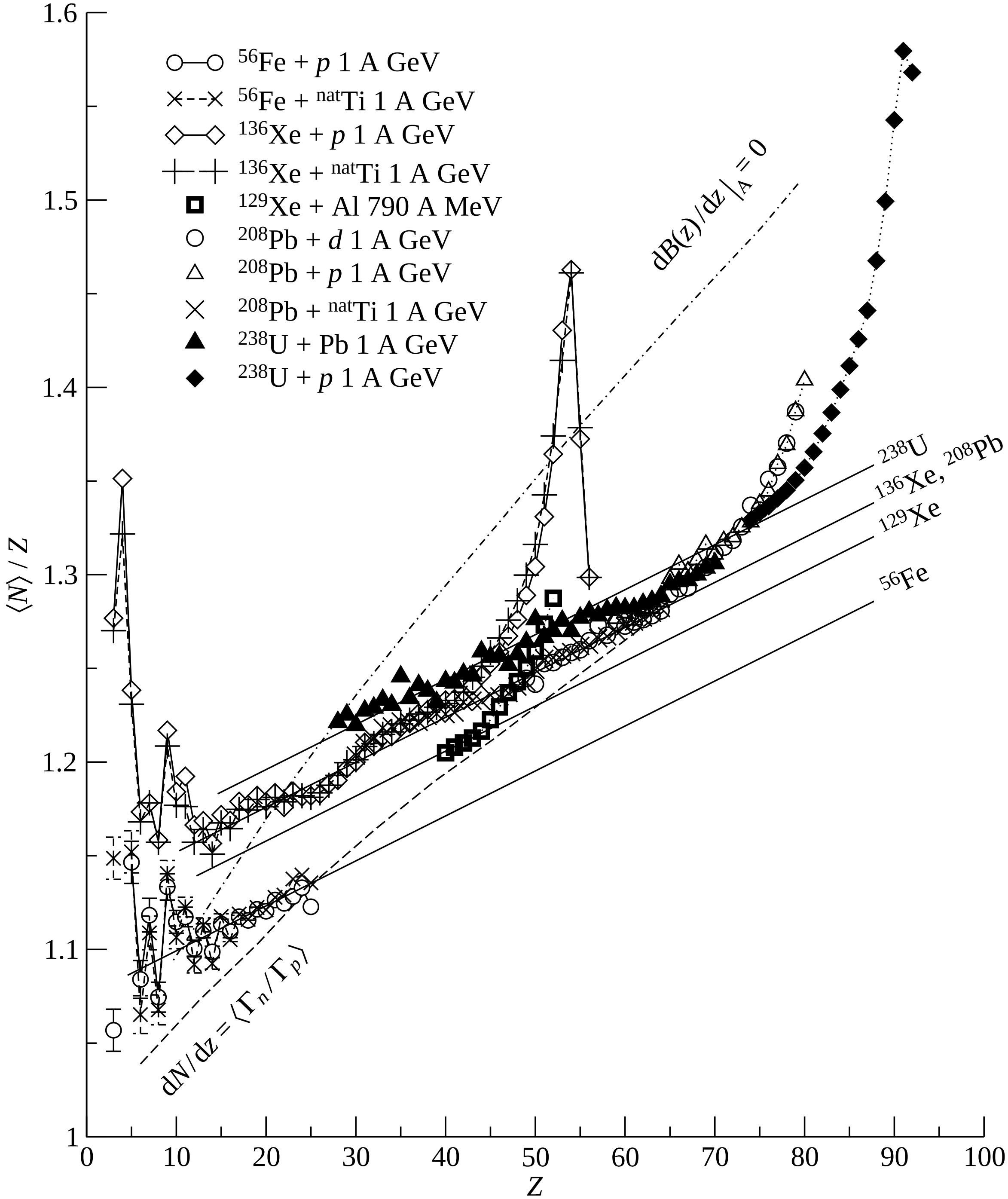

Figure 6.5: Full collection of experimental measurement for systems with different N/Z. ^{136}Xe+p , ^{136}Xe+^{nat}Ti , ^{136}Xe+^{nat}Al [Reinhold 1998], ^{208}Pb+^{nat}Ti [Enqvist 2001b], ^{208}Pb+d [Enqvist 2001a], ^{208}Pb+p [Enqvist 2001b], ^{238}U+p [Taieb03], ^{238}U+^{208}Pb [Enqvist 1999]. An ordering as a function of the $\langle N \rangle/Z$ is the result of the comparison. Dashed and dashed-dotted lines are defined in fig. 6.2. The solid lines serve only to guide the eyes.

Chapter 7

Conclusion

The mechanisms of fragment emission from four systems, ^{56}Fe+p, ^{56}Fe+$^{\mathrm{nat}}$Ti, ^{136}Xe+p, ^{136}Xe+$^{\mathrm{nat}}$Ti at 1 A GeV, have been investigated. ^{56}Fe+$^{\mathrm{nat}}$Ti and ^{136}Xe+$^{\mathrm{nat}}$Ti were regarded as a baseline for very high-energy processes (multifragmentation). We focused mainly on the proton-induced reactions. The certain understanding that we could attain from the analysis of the ^{56}Fe+p an ^{136}Xe+p systems is that light residues are produced in the decay of highly excited remnants. Furthermore, from a more quantitative discussion, we inferred that the emitting source should also be heavy and close to the projectile mass. The magnitude of the Coulomb repulsion, together with the very high formation yields, even suggested that an asymmetric break-up process, hardly connected to asymmetric fission or statistical cluster emission, might be the favoured channel of light-residue production. These findings were derived from experimental observables like the isotopic cross sections measured for the whole ensemble of the residues, and the velocity distributions of the emitted fragments in the projectile frame along the beam axis. Especially the shape of the velocity spectra offered us a microscopic insight into the mechanisms of light-particle emission. In analysing the features of the velocity spectra, we failed in describing the kinematics within a general systematics of fission total-kinetic-energy release. A complete simulation of the whole reaction process, where sequential fission-evaporation decays govern the deexcitation, could not consistently describe the gross experimental features of the decay.

We suggested that the characteristics of the kinematics and the production of light residues could carry indications of fast asymmetric splits. A description of the complete reaction process, including channels of fast break-up decays revealed to be more adapted in depicting the decay of the most highly excited remnants, and was compatible with the high yields for light residues and the complex shapes of the velocity spectra. Encouraged by this consistency and, first of all, on the basis of previous theoretical and experimental results (see references in the section 4), we suggested that protons at incident energies of 1 A GeV traversing heavy ions can introduce very high thermal excitation energy per nucleon in the system, even above 2.5 MeV. Such a thermal excitation could lead to attain freeze-out conditions. to fission-evaporation decays enters in competition with break-up decay. When the excitation energy is just sufficient to access break-up channels, partitions with low multiplicity of intermediate-mass fragments and high asymmetry are favoured: the decay results mainly in the simultaneous formation of one heavy residue, with mass close to the hot remnant, and one or more light clusters and nucleons. As an extreme case, two fragments rather asymmetric in mass may be formed in the same fast break-up process. The formation of light fragments in the ^{56}Fe+p and ^{136}Xe+p reactions could be explained by this picture.

The examination of the isotopic component offered even further insights. Analyzing nuclear-structure effects in the nuclide production we also inferred that fragments are formed above the particle-emission threshold and few nucleons emitted by the fragments are responsible for generating the complex even-odd staggering observed in the yields and some drastic changes of shape in the velocity spectra of neighboring nuclei. Finally, we found that the ridge of the isotopic production, and the mean neutron enrichment of the residues do not depend on the entrance channel, but is only related to the isotopic composition of the system. This independence can be interpreted as a manifestation of the plateau of the nuclear caloric curve. On the basis of this observable, we could find signatures of the phase transition in systems like ^{56}Fe+p and ^{136}Xe+p at 1 A GeV, excited slightly above the threshold for accessing multifragmentation. These signatures could be as well extended to the formation of heavy nuclides, that might be associated to rather asymmetric break-up configurations.

Appendix A

General equations of motion of charged particles in the Fragment-Separator

A.0.3 The motion of a charged particle in a magnetic field

In general, the motion of a charged particle in an electromagnetic field is described by the Lorentz force:

$$\frac{\mathrm{d}\vec{p}}{\mathrm{d}t} = q\left(\vec{E} + \vec{v} \wedge \vec{B}\right) \quad ,$$

where q, $\vec{p}$ and $\vec{v}$ are the charge, the momentum and the velocity of the particle respectively, $\vec{E}$ and $\vec{B}$ are the electric and magnetic fields respectively. The electric component gives the acceleration of the particle and the magnetic component corresponds to the bending. Since we are interested in the beam optics, we will assume $\vec{E}$ equal to 0 and consider the bending term only:

$$\frac{\mathrm{d}\vec{p}}{\mathrm{d}t} = q\vec{v} \wedge \vec{B} \quad , \tag{A.1}$$

In accordance with figure A.1, we consider a particle "p_0" with momentum $\vec{p}_0$ travelling along a trajectory s_0, with a curvature radius $\rho(s_0)$, under the effect of a magnetic field $\vec{B}(s_0)$. s_0 is the equilibrium trajectory defined by the equal competition between the Lorentz force and the centrifugal force, expressed by the relation A.2.

$$B(s_0)\rho(s_0) = \frac{p_0}{q} \quad . \tag{A.2}$$

Henceforth we will consider the particle "p_0" and its trajectory s_0 as a reference. With respect to this reference, we describe a new trajectory s travelled by a particle

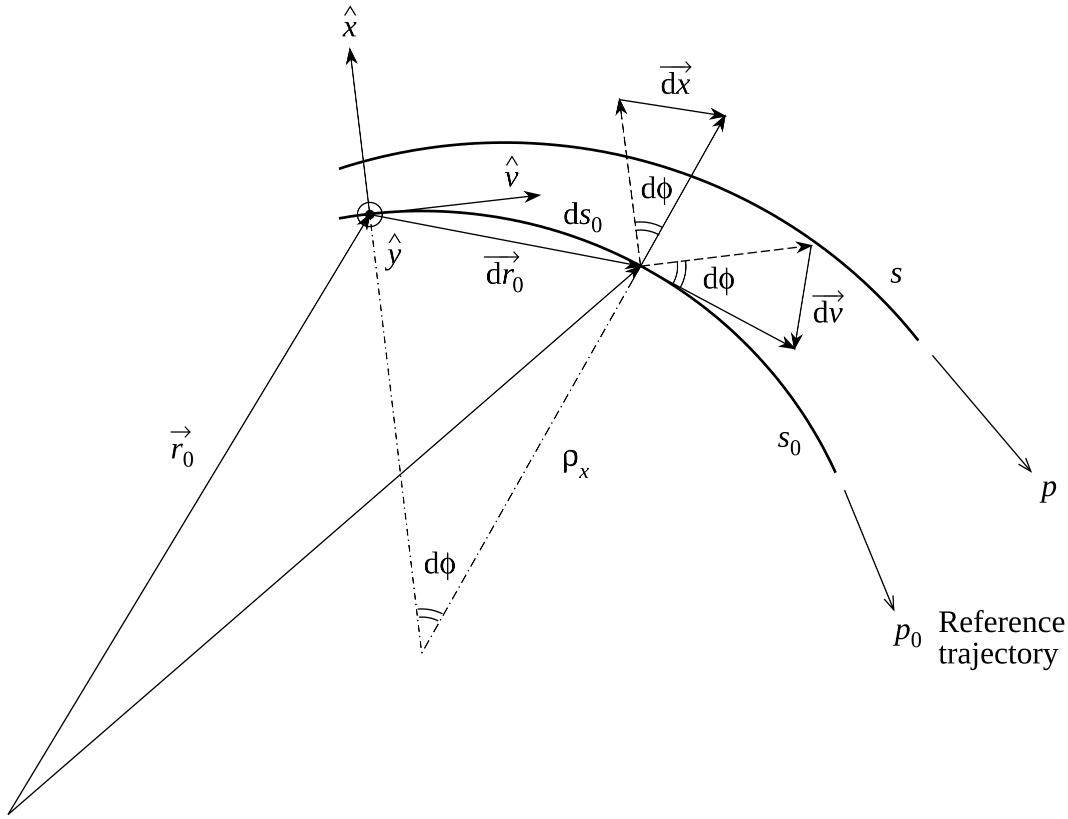

Figure A.1: Trajectory of a charged particle in a magnetic field

"p", with momentum $\vec{p}$, velocity $\vec{v}$, and position $\vec{r}$ in the laboratory frame. Some general kinematical relations for the particle "p" are

$$\vec{v} = \frac{\mathrm{d}\vec{r}}{\mathrm{d}t} = \frac{\mathrm{d}s}{\mathrm{d}t}\frac{\mathrm{d}\vec{r}}{\mathrm{d}s} = v\frac{\mathrm{d}s_0}{\mathrm{d}s}\frac{\mathrm{d}\vec{r}}{\mathrm{d}s_0} = \frac{v}{s'}\vec{r'} \quad , \tag{A.3}$$

$$\vec{p} = m\gamma\vec{v} = m\gamma\frac{v}{s'}\vec{r'} \quad , \tag{A.4}$$

where the prime represents a derivative with respect of the path length s_0. The motion can be described by the following set of derivatives:

$$\frac{\mathrm{d}\vec{v}}{\mathrm{d}t} = \frac{\mathrm{d}^2\vec{r}}{\mathrm{d}t^2} = \frac{\mathrm{d}}{\mathrm{d}t}\left(\frac{v}{s'}\vec{r'}\right) = \frac{\mathrm{d}s}{\mathrm{d}t}\frac{\mathrm{d}}{\mathrm{d}s_0}\left(\frac{v}{s'}\vec{r'}\right) = \frac{v^2}{s'^2}\left(\vec{r''} - \frac{s''}{s'}\vec{r'}\right) \quad , \tag{A.5}$$

$$\frac{\mathrm{d}\vec{p}}{\mathrm{d}t} = m\gamma\frac{\mathrm{d}\vec{v}}{\mathrm{d}t} = m\gamma\frac{v^2}{s'^2}\left(\vec{r''} - \frac{s''}{s'}\vec{r'}\right) = \frac{pv}{s'^2}\left(\vec{r''} - \frac{s''}{s'}\vec{r'}\right) \quad . \tag{A.6}$$

Introducing eq. A.5 and eq. A.6 into eq. A.1 we obtain the equation of motion of the particle "p' in the magnetic field $\vec{B}(s)$

$$\vec{r''} - \frac{s''}{s'}\vec{r'} = s'\frac{q}{p}\left(\vec{r'} \wedge \vec{B}\right) \quad . \tag{A.7}$$

We need some further passages to reduce this relation to a suitable equation of motion. If we introduce the transverse-motion unit vector $\hat{x}$ and the velocity unit vector $\hat{v}$, directed from a point of s_0 we can deduce from geometrical considerations (considering $\mathrm{d}\phi$ infinitesimally small):

$$\mathrm{d}\hat{x} = \mathrm{d}\phi\hat{v}\ , \qquad \mathrm{d}\hat{v} = -\mathrm{d}\phi\hat{x}\ , \qquad \mathrm{d}\vec{r_0} = \mathrm{d}s_0\hat{v}\ , \tag{A.8}$$

$$\mathrm{d}s_0 = \mathrm{d}\phi\rho_x \qquad . \tag{A.9}$$

Dividing the differentials A.8 by $\mathrm{d}s_0$ (defined in A.9) and defining the horizontal curvature as

$$k_x = 1/\rho_x \quad ,$$

we obtain the derivatives

$$\hat{v}' = -k_x\hat{x}\ , \quad \hat{x}' = k_x\hat{v}\ , \quad \vec{r_0'} = \hat{v} \quad . \tag{A.10}$$

The particle trajectory can be described as a deviation from the design trajectory s_0:

$$\vec{r}\left(x, y, s_0\right) = \vec{r_0}\left(s_0\right) + x\hat{x}\left(s_0\right) + y\hat{y}\left(s_0\right)$$

Deriving with respect to s_0 and introducing the equalities A.10 we obtain:

$$\vec{r'} = \left(1 + k_x x\right)\hat{v} + x'\hat{x} + y\vec{y'} + y'\hat{y} \tag{A.11}$$

$$\vec{r''} = \left(k_x' x + 2k_x x'\right)\hat{v} + \left(x'' - k_x - k_x^2 x\right)\hat{x} + y\vec{y''} + 2y'\vec{y'} + y''\hat{y} \tag{A.12}$$

Since all bending magnets of the Fragment Separator deflect the beam on the horizontal plane, we can impose that $\hat{y}' = \hat{y}'' = 0$ and write

$$\vec{r'} = \left(1 + k_x x\right)\hat{v} + x'\hat{x} + y'\hat{y} \tag{A.13}$$

$$\vec{r''} = \left(k_x' x + 2k_x x'\right)\hat{v} + \left(x'' - k_x - k_x^2 x\right)\hat{x} + y''\hat{y} \tag{A.14}$$

The magnetic field $\vec{B}$ can be decomposed into $\vec{B} = B_x\hat{x} + B_y\hat{y}$ and the vector product in eq. A.7 can be written:

$$\vec{r'} \wedge \vec{B} = \begin{vmatrix} \hat{v} & \hat{x} & \hat{y} \\ 1 + k_x x & x' & y' \\ 0 & B_x & B_y \end{vmatrix} = \left(x'B_y - y'B_x\right)\hat{v} - \left(1 + k_x x\right)B_y\hat{x} + \left(1 + k_x x\right)B_x\hat{y} \tag{A.15}$$

We express the equation (A.7) with respect to the horizontal and vertical component, by writing

$$\vec{r''}\hat{x} - \frac{s''}{s'}\vec{r'}\hat{x} = s'\frac{q}{p}\left(\vec{r'} \wedge \vec{B}\right)\hat{x}\ , \tag{A.16}$$

$$\vec{r''}\hat{y} - \frac{s''}{s'}\vec{r'}\hat{y} = s'\frac{q}{p}\left(\vec{r'} \wedge \vec{B}\right)\hat{y} \quad . \tag{A.17}$$

Substituting $\vec{r'}$ and $\vec{r''}$ with the expression A.13 and A.14, respectively, these relations can be also written in the form

$$x'' - k_x - k_x^2 x - \frac{s''}{s'}x' = -s'\frac{q}{p}\left(1 + k_x x\right)B_y\ , \tag{A.18}$$

$$y'' - \frac{s''}{s'}y' = s'\frac{q}{p}\left(1 + k_x x\right)B_x \quad , \tag{A.19}$$

or

$$x'' - \frac{s''}{s'}x' = (1 + k_x x)\left(k_x - s'\frac{q}{p}B_y(s)\right) , \tag{A.20}$$

$$y'' - \frac{s''}{s'}y' = (1 + k_x x)\left(s'\frac{q}{p}B_x(s)\right) . \tag{A.21}$$

These equations constitute the law of motion of a particle with momentum p, travelling along the trajectory s. Evidently, it is sufficient to impose $p = p_0, s = s_0$ and $x = y = 0$ to obtain the equation of motion A.2, for the reference particle "p_0".

A.0.4 The dispersion function

In the following we will only consider the horizontal component of the equation of motion. We can write eq. A.20 in terms of "momentum deviation", that is defined as

$$\delta \doteq \frac{p - p_0}{p_0} = \frac{\Delta p}{p_0} .$$

The horizontal component of the equation of motion can be written in the form

$$x'' - \frac{s''}{s'}x' = (1 + k_x x)\left(k_x - s'(1 - \delta)\frac{q}{p_0}B_y\right) , \tag{A.22}$$

where the momentum deviation δ has been introduced by the following approximation, valid for $\delta^2 << 1$:

$$p = p_0\,(1 + \delta) \approx \frac{p_0}{1 - \delta} . \tag{A.23}$$

In addition, we can approximate the path length variation to the first order by imposing

$$ds \approx ds_0 + xd\phi = \rho_x d\phi + xd\phi = (\rho_x + x)\,d\phi = (\rho_x + x)\,k_x ds_0 = (1 + k_x x)\,ds_0$$

or

$$s' = \frac{ds}{ds_0} = 1 + k_x x . \tag{A.24}$$

By substituting s' with the relation A.24 and neglecting the term $(s''/s')x'$ we obtain

$$x'' = (1 + k_x x)\left[k_x - (1 + k_x x)(1 - \delta)\frac{q}{p_0}B_y\right] , \tag{A.25}$$

B_y can be approximated by a magnetic field expansion. The difference of $(q/p_0)B_y$ from $(q/p_0)B_{y_0}$ (the latter is expressed in equation of motion A.2, for the reference particle) can be approximated by two terms varying linearly with x and y, respectively

$$\frac{q}{p_0}B_y \approx k_x + \chi_y x - \chi_x y , \tag{A.26}$$

where we defined:

$$\chi_y \doteq \frac{q}{p_0}\left(\frac{\mathrm{d}B_y}{\mathrm{d}x}\right)_0 , \chi_x \doteq \frac{q}{p_0}\left(\frac{\mathrm{d}B_x}{\mathrm{d}x}\right)_0 \quad . \tag{A.27}$$

Thus, the horizontal component of the equation of motion can now be written

$$x'' = (1 + k_x x)\left[k_x - (1 - \delta + k_x x - \delta k_x x) \cdot (k_x + \chi x - \chi_x y)\right] \quad . \tag{A.28}$$

Neglecting terms in x^2, xy in the following passages, we obtain

$$x'' = (1 + k_x x)(k_x - k_x - \chi x + \chi_x y + \delta k_x + \delta \chi x - \delta \chi_x y - {k_x}^2 + \delta {k_x}^2 x) \quad , \tag{A.29}$$

or

$$x'' + \left(\chi - \delta\chi + {k_x}^2 - \delta {k_x}^2\right) x + (\delta \chi_x - \chi_x)\, y = \delta k_x \quad , \tag{A.30}$$

We can neglect also the terms $\delta\chi, \delta {k_x}^2, \delta\chi_x$ and reduce the horizontal component of the equation of motion to the simplified form:

$$x'' + \left(\chi + {k_x}^2\right) x = \delta k_x + \chi_x y \quad . \tag{A.31}$$

Applying a similar series of approximations (and approximating B_x according to the magnetic field expansion $(q/p_0)B_x \approx \chi_x x + \chi_y y$), we can write the vertical component of equation of motion in the form:

$$y'' - k_0 = \chi_x x \quad . \tag{A.32}$$

The term $\chi_x y$ produces a coupling between horizontal and vertical motion: in a beam line skew quadrupoles (i.e. quadrupoles tilted with an angle of 45°) have the role to introduce this effect. Since in the FRS no skew quadrupoles are used we impose that this effect is negligible, and we can write the following linearised and simplified equation of motion for a particle travelling on the horizontal plane:

$$x'' + \left(\chi + \frac{1}{\rho^2}\right) x = \frac{\delta}{\rho} \quad . \tag{A.33}$$

Considering the displacement relatively to the momentum deviation, we can define the "dispersion function" as

$$D\left(s_0\right) = \frac{x\left(s_0\right)}{\delta} \quad . \tag{A.34}$$

Thus, the equation (A.33) can be modified into

$$D'' + \left(\chi\left(s_0\right) + \frac{1}{\rho^2\left(s_0\right)}\right) D = \frac{1}{\rho\left(s_0\right)} \quad . \tag{A.35}$$

We should remark that the equation (A.35) is verified for regions where the beam doesn't cross any particle detector, diagnostic device, or any other layer of matter, otherwise it's still a good approximation.

Inserting the dispersion function in (A.2) we can find a very useful equation:

$$B(s_0)\rho(s_0) = \frac{p_0}{q} = \frac{p_0}{\Delta p}\frac{\Delta p}{q} = \frac{1}{\delta}\frac{\Delta p}{q} = \frac{D}{x}\frac{\Delta p}{q} \quad ,$$

or

$$B(s_0)\rho(s_0)\frac{x}{D} = \frac{p}{q} - \frac{p_0}{q} = B(s)\rho(s) - B(s_0)\rho(s_0) \quad ,$$

or

$$B(s)\rho(s) = B(s_0)\rho(s_0)\left(1 + \frac{x\,(s_0)}{D\,(s_0)}\right) \quad . \tag{A.36}$$

A.0.5 The transfer matrix for a series of optical elements

In the previous section we derived the equation of motion on the horizontal plane in the two equivalent forms:

$$x''\,(s_0) + \xi\,(s_0)\,x\,(s_0) \;=\; \frac{\delta}{\rho\,(s_0)} \quad , \tag{A.37}$$

$$D''\,(s_0) + \xi\,(s_0)\,D\,(s_0) \;=\; \frac{1}{\rho\,(s_0)} \quad , \tag{A.38}$$

where:

$$\xi \doteq \left(\chi\,(s_0) + \frac{1}{\rho^2\,(s_0)}\right) \quad . \tag{A.39}$$

We can firstly consider the homogeneous equation, describing the motion of an on-momentum ($\delta = 0$) particle, oscillating around the central trajectory S_0. From the relation (A.37) we obtain the well known “Hill equation”:

$$x''\,(s_0) + \xi\,(s_0)\,x\,(s_0) = 0 \quad . \tag{A.40}$$

We might observe that the same equation holds for the motion of a pendulum in the case of small-oscillation approximation. We can find a base of solutions constituted of a “sine-like” solution S and a “cosine-like” solution C:

$$S'' + \xi\ S = 0 \quad ; \qquad C'' + \xi\ C = 0 \quad , \tag{A.41}$$

In order to be linearly independent, they should satisfy the condition

$$\mathcal{W} = \begin{vmatrix} C & S \\ C' & S' \end{vmatrix} \neq 0 \quad . \tag{A.42}$$

The derivative of the Wronsky determinant vanishes identically, in fact from (A.41):

$$\mathcal{W}' = CS'' - SC'' = -\xi\,(CS - SC) = 0 \quad .$$

Consequently, the initial condition at the origin $s_0 = 0$ determines $\mathcal{W}$ everywhere and we can impose:

$$C(s_0 = 0) = 1, \quad S(s_0 = 0) = 1 \quad ,$$
$$C'(s_0 = 0) = 1, \quad S'(s_0 = 0) = 1 \quad , \tag{A.43}$$
$$\tag{A.44}$$

$$\mathcal{W} = 1 \quad .$$

Adding two more initial conditions

$$x_0 = x(s_0 = 0) \quad ; \qquad x'_0 = x'(s_0 = 0) \quad ,$$

we can write the solution of (A.40) in the form:

$$\begin{aligned} x(s_0) &= x_0 C(s_0) + x'_0 S(s_0) \\ x'(s_0) &= x_0 C'(s_0) + x'_0 S'(s_0) \quad . \end{aligned} \tag{A.45}$$

Equivalently, we can write:

$$\begin{pmatrix} x(s_0) \\ x'(s_0) \end{pmatrix} = \mathcal{T}_{(0 \to s_0)} \begin{pmatrix} x_0 \\ x'_0 \end{pmatrix} \quad , \tag{A.46}$$

with

$$\mathcal{T}_{(0 \to s_0)} = \begin{pmatrix} C(s_0) & S(s_0) \\ C'(s_0) & S'(s_0) \end{pmatrix} \quad , \tag{A.47}$$

where $\mathcal{T}_{(0 \to s_0)}$ is the "Transfer matrix" that, multiplied for the position and the slope of the trajectory of the particle in the origin, gives the position and trajectory slope of the particle at the point s_0.

$\mathcal{T}_{(0 \to s_0)}$ characterizes the optical properties of the segment $\overline{0, s_0}$. A transfer line composed of n optical elements $\mathcal{T}_{(i \to i+1)}$ is described by the repeated matrix multiplication from element to element, resulting into the "total transfer matrix"

$$\mathcal{T} = \prod_{i=1}^{n} \mathcal{T}_{(i \to i+1)} \quad ,$$

The homogeneous solution of (A.37) can therefore be written in the form

$$\begin{pmatrix} x(s_0) \\ x'(s_0) \end{pmatrix} = \mathcal{T} \begin{pmatrix} x_0 \\ x'_0 \end{pmatrix} \quad . \tag{A.48}$$

We can now introduce the momentum dispersion about the reference momentum p_0: in this case the particles will travel oscillating about a new equilibrium trajectory shifted with respect to the design path s_0.

We should consider the inhomogeneous equation A.38 and impose the initial condition

$$D_0 = D_0' = 0 \quad ,$$

assuming that particles with different momenta are not spatially separated at the beginning. In the case of the FRagment Separator this condition is a very reasonable approximation, since particles are generated as reaction products from a target placed at the beginning of the optic line. Our approximation is to consider both the beam-spot in the target plane and in the target dimensionless. We can verify that a particular solution is:

$$D_{par} = S\left(s_0\right) \int_{s_0}^{s} \frac{C\left(\sigma\right)}{\rho\left(\sigma\right)} \mathrm{d}\sigma - C\left(s_0\right) \int_{s_0}^{s} \frac{S\left(\sigma\right)}{\rho\left(\sigma\right)} \mathrm{d}\sigma \tag{A.49}$$

In fact:

$$\begin{aligned}
D'_{par} &= S \int_{s_0}^{s} \frac{C'}{\rho} \mathrm{d}\sigma - C \int_{s_0}^{s} \frac{S'}{\rho} \mathrm{d}\sigma \\
D''_{par} &= S \int_{s_0}^{s} \frac{C''}{\rho} \mathrm{d}\sigma - C \int_{s_0}^{s} \frac{S''}{\rho} \mathrm{d}\sigma + \frac{1}{\rho} \left(CS' - SC'\right) \\
&= -\xi S \int_{s_0}^{s} \frac{C}{\rho} \mathrm{d}\sigma + \xi C \int_{s_0}^{s} \frac{S}{\rho} \mathrm{d}\sigma + \frac{1}{\rho} \underbrace{\mathcal{W}}_{=1} \\
&= -\xi D_{par} + \frac{1}{\rho}
\end{aligned}$$

In (A.49), $C\left(s_0\right)$ and $S\left(s_0\right)$ are the same cosine-like and sine-like functions appearing in the matrix $\mathcal{T}_{(i \to i+1)}$. Adding the particular solution (A.49) to the homogeneous solution (A.45) we can write:

$$\begin{aligned}
x\left(s_0\right) &= x_0 C\left(s_0\right) + x_0' S\left(s_0\right) + \delta D_{par} \\
x'\left(s_0\right) &= x_0 C'\left(s_0\right) + x_0' S'\left(s_0\right) + \delta D'_{par}
\end{aligned}$$

or

$$\begin{pmatrix} x\left(s_0\right) \\ x'\left(s_0\right) \end{pmatrix} = \begin{pmatrix} C\left(s_0\right) & S\left(s_0\right) \\ C'\left(s_0\right) & S'\left(s_0\right) \end{pmatrix} \begin{pmatrix} x_0 \\ x_0' \end{pmatrix} + \delta \begin{pmatrix} D_{par} \\ D'_{par} \end{pmatrix} \tag{A.50}$$

Appendix B

Numerical inversion of the relation between the measured velocity spectra and the cross sections

We present a simple numerical method to reverse the relation (3.4) and extract $\sigma(v)$ as a function of the absolute velocity $v = |\vec{v}|$ in the centre of mass of the hot remnant. For each velocity v, we define a shell in the velocity space with internal radius v and external radius $v + \delta v$; the ratio between the portion of the shell transmitted through the spectrometer and the volume of the shell, determines the coefficient of transmission $t(\varphi, v_\perp, u)$. This coefficient can be calculated geometrically, paying a special attention to the change of frame: neither the reaction recoil, nor the slowing down of the projectile and the residues in the target should be neglected. On the other hand, the detailed features of the acceptance of the spectrometer should be calculated with an ion-optics code [Benlliure 2002]

The $\mathcal{V}_{a,p,\varphi}$ is the volume element in the three-dimensional velocity space corresponding to an absolute velocity interval of $[a, a+\delta v[$, a longitudinal projection (in the beam direction) with a range of $[p, p+\delta v[$, and a rotation angle varying in $[\varphi, \varphi+\delta\varphi[$ around the beam direction. $\mathcal{I}_{a,p,\varphi}$ is the probability that a particle is emitted within the limits of $\mathcal{V}_{a,p,\varphi}$.

The experiment provided the apparent cross section of emission of a residue with a longitudinal velocity component $+v$ or $-v$ in respect to the centre of mass. We label $\mathcal{Y}_{+v}$ the apparent cross section measured in the forward direction, and $t_+(v, \vec{v}_{Lab})$ the transmission calculated only for the forward half of the velocity shell. The cross section for the emission of the particle with absolute velocity v in the centre of mass frame is deduced from the relation

$$\sigma_v \frac{t_+(v, \vec{v}_{Lab})}{2} = \mathcal{Y}_{+v} - \mathcal{G}_{+v} + \mathcal{L}_{+v} \quad , \tag{B.1}$$

where $\mathcal{G}_{+v}$ is the contribution gained from velocity vectors with higher magnitude than v and projection equal to v. $\mathcal{L}_{+v}$ is the contribution lost due to the projection of $\vec{v}$ on lower longitudinal velocity components than v. We can write:

$$\mathcal{G}_{+v} = \sum_{\varphi=0,\mathrm{d}\varphi,2\delta\varphi,\ldots,2\pi} \quad \sum_{p=v+\delta v,v+2\delta v,\ldots,a\star} \frac{\mathcal{V}_{a,v,\varphi}}{\mathcal{V}_{a,p,\varphi}} \mathcal{I}_{p,p,\varphi} \quad ,$$

$$\mathcal{L}_{+v} = \sum_{\varphi=0,\delta\varphi,2\delta\varphi,\ldots,2\pi} \quad \sum_{a=v-\delta v,v-2\delta v,\ldots,p\star} \frac{\mathcal{V}_{v,p,\varphi}}{\mathcal{V}_{a,p,\varphi}} \mathcal{I}_{v,v,\varphi} \quad ,$$

where $p\star$ is the smallest longitudinal projection of $\vec{v}$ permitted by the acceptance. $a\star$ is the largest absolute velocity whose longitudinal component is equal to v.

The terms $\mathcal{G}_{+v}$ and $\mathcal{L}_{+v}$ couple the equation (B.1) with all the equations of the same kind defining the cross sections for lower and higher velocities than v. The result is a system of equation that, if solved in order of decreasing velocity starting from the largest, is triangular and can be solved straightforward.

Since we assumed that the emission is isotropic with respect to the centre of mass, the same result derived for σ_v should be obtained using the apparent cross section $\mathcal{Y}_{-v}$, measured in backward direction with respect to the centre of mass. The difference in the value of σ_v, when obtained from $\mathcal{Y}_{+v}$ or from $\mathcal{Y}_{-v}$ can be an indication of the uncertainty introduced in the extraction of the cross section σ_v by the assumption of isotropic emission.

Appendix C

Isotopic cross sections

In the section 2.4 the procedure to extract cross sections from the measured longitudinal velocity spectra was described. The results for the light nuclides formed in the systems ^{56}Fe+p and ^{56}Fe+$^{\mathrm{nat}}$Ti are presented in table C.1 with the statistical uncertainties. In appendix B the numerical tool used in the analysis was presented. It should be observed that the velocity-reconstruction method allows to obtain cross sections for isotopes of which at least a half of the longitudinal velocity spectrum is measured. In this case, some needed parameters like the mean recoil velocity or the width of the distribution could be extrapolated from neighboring isotopes. On the other hand, the whole procedure is valid up to a certain extent: due to the assumption of isotropic emission, ideal cases should result into equal (equal area and equal centroid) absolute-velocity distributions deduced from the forward and the backward part of the measured longitudinal velocity distributions. Deviations from this ideal case derive either from the physics of the reaction process, that could differ from a purely isotropic emission , or by the lack of statistics in some parts of the spectrum, resulting in complicating the convergence of the numerical calculation. This leads to results that fluctuate by 10% in the average. We take this value as the statistical uncertainty (and not simply the statistics of counts).

The systematic uncertainties are in general very small in FRS measurements of spallation residues. Indeed they rise to considerably high values when the measurement is dedicated to fragments having very high velocities in the projectile frame. This is the case of very light fragments emitted in fission-like events or in break-up processes. The largest source of uncertainty is the angular acceptance. Heavy residues, close to the projectile mass are emitted very forward, and the angular acceptance is close to 100%. On the contrary, light fragments are strongly affected. The multiplicity of the intermediate-mass fragments could not directly be measured. From physical arguments we could safely infer that light fragments are emitted in events with multiplicity (of fragments with A>4) prevalently equal to two. Indeed we could not exclude the possible contribution of higher multiplicity processes. We estimated the systematic uncertainty to be up to 30%.

Tableau C.1: Spallation and fragmentation residue isotopic cross sections measured in this work for the formation of Li, Be, B, C, N and O in the reaction ^{56}Fe+p and ^{56}Fe+^{nat}Ti, respectively.

Isotope	^{56}Fe+p, σ [mb]	^{56}Fe+^{nat}Ti, σ [mb]
^{6}Li	14.89± 1.5	128.50± 12.9
^{7}Li	3.06± 0.3	103.46± 10.3
^{7}Be	3.09± 0.3	62.28± 6.2
^{9}Be	2.11± 0.2	29.88± 3.0
^{10}B	2.03± 0.2	35.06± 3.5
^{11}B	3.82± 0.4	61.58± 6.2
^{12}B	0.36± 0.04	9.56± 1.0
^{11}C	1.12± 0.1	16.02± 1.6
^{12}C	4.69± 0.4	62.50± 6.3
^{13}C	2.76± 0.3	37.59± 3.6
^{14}C	1.87± 0.2	14.74± 1.5
^{13}N	0.14± 0.01	.
^{14}N	1.25± 0.1	18.67± 1.9
^{15}N	2.97± 0.3	37.33± 3.7
^{16}N	0.33± 0.03	5.04± 0.5
^{17}N	0.11± 0.01	2.44± 0.2
^{18}N	.	0.01± 0.001
^{14}O	0.01± 0.001	.
^{15}O	0.33± 0.03	5.91± 0.6
^{16}O	2.78± 0.3	36.62± 3.7
^{17}O	1.46± 0.1	15.58± 1.5
^{18}O	0.75± 0.08	9.12± 0.9
^{19}O	0.13± 0.01	1.99± 0.2

It might be remarked that the greatest contribution to the total uncertainty comes from the systematic uncertainty. On the other hand, the cross-section ratios of different nuclides are very consistent as they are related to small statistical uncertainties.

The results for the nuclide production measured for the systems ^{136}Xe+p and ^{136}Xe+^{nat}Ti is entirely presented in table C.2. Statistical uncertainties vary from around 15% for the lightest masses to 2-3 % for the heavier masses. Rather than the number of counts, the main contribution to this uncertainty derives from the finite angular acceptance. Also for these systems we estimated the systematic uncertainty to be up to 30%.

Tableau C.2: Spallation and fragmentation residue isotopic cross sections measured in this work for the formation of nuclides ranging from Li, to Ba in the reaction ^{136}Xe+p and ^{136}Xe+$^{\mathrm{nat}}$Ti.

Isotope	^{136}Xe+p, σ [mb]	^{136}Xe+$^{\mathrm{nat}}$Ti, σ [mb]
^{6}Li	7.9863± 0.6653	304.161± 36.922
^{7}Li	15.5454± 1.2902	455.708± 54.736
^{8}Li	2.6310± 0.2250	110.653± 13.148
^{9}Li	0.4225± 0.0349	13.002± 1.547
^{7}Be	0.4307± 0.0362	31.160± 3.751
^{9}Be	3.5901± 0.2986	114.761± 13.484
^{10}Be	3.5310± 0.2917	119.718± 13.885
^{11}Be	0.1658± 0.0165	8.421± 0.978
^{12}Be	0.0490± 0.0042	1.624± 0.200
^{8}B	0.0050± 0.0008	0.458± 0.061
^{10}B	0.9125± 0.0754	46.286± 5.373
^{11}B	4.6740± 0.3816	199.431± 22.820
^{12}B	1.3981± 0.1166	48.835± 5.518
^{13}B	0.4445± 0.0407	21.512± 2.398
^{14}B	0.0160± 0.0017	1.340± 0.168
^{10}C	0.0045± 0.0007	0.330± 0.044
^{11}C	0.1737± 0.0144	9.926± 1.141
^{12}C	1.5520± 0.1251	82.203± 9.279
^{13}C	2.2017± 0.1780	108.465± 12.067
^{14}C	1.6637± 0.1356	70.564± 7.735
^{15}C	0.1705± 0.0187	10.633± 1.153
^{16}C	0.0400± 0.0033	4.078± 0.437
^{17}C	0.0045± 0.0005	0.269± 0.033
^{13}N	0.0254± 0.0023	1.501± 0.172
^{14}N	0.4911± 0.0394	28.551± 3.133
^{15}N	2.2146± 0.1751	117.304± 12.649
^{16}N	0.5814± 0.0487	27.156± 2.887
^{17}N	0.3734± 0.0329	18.010± 1.883
^{18}N	0.0277± 0.0022	3.908± 0.406
^{15}O	0.0437± 0.0037	2.675± 0.293
^{16}O	0.7094± 0.0551	44.620± 4.735
^{17}O	0.5765± 0.0454	36.065± 3.765
^{18}O	0.7667± 0.0609	41.033± 4.207
^{19}O	0.2883± 0.0251	13.253± 1.338
^{20}O	0.0198± 0.0016	5.173± 0.516

Isotope	^{56}Xe+p, σ [mb]	^{56}Xe+^{nat}Ti, σ [mb]
^{17}F	0.0117± 0.0011	0.794± 0.087
^{18}F	0.1209± 0.0096	8.090± 0.834
^{19}F	0.4798± 0.0368	30.383± 3.059
^{20}F	0.5931± 0.0462	33.992± 3.357
^{21}F	0.4311± 0.0347	20.811± 2.017
^{22}F	0.1052± 0.0106	5.203± 0.498
^{23}F	0.0079± 0.0007	1.501± 0.144
^{19}Ne	0.0085± 0.0008	0.573± 0.061
^{20}Ne	0.1666± 0.0125	11.477± 1.136
^{21}Ne	0.4433± 0.0328	29.536± 2.859
^{22}Ne	0.6546± 0.0486	39.625± 3.756
^{23}Ne	0.2571± 0.0212	14.319± 1.333
^{24}Ne	0.1306± 0.0120	6.097± 0.558
^{21}Na	0.0048± 0.0005	0.297± 0.031
^{22}Na	0.0843± 0.0063	5.657± 0.539
^{23}Na	0.4391± 0.0312	27.837± 2.584
^{24}Na	0.3968± 0.0287	24.570± 2.232
^{25}Na	0.3140± 0.0239	18.206± 1.618
^{26}Na	0.2347± 0.0167	4.975± 0.436
^{27}Na	0.0010± 0.0001	1.733± 0.151
^{23}Mg	0.0058± 0.0006	0.461± 0.047
^{24}Mg	0.1467± 0.0102	9.665± 0.879
^{25}Mg	0.3117± 0.0214	20.894± 1.855
^{26}Mg	0.4622± 0.0316	29.696± 2.574
^{27}Mg	0.2413± 0.0179	13.959± 1.185
^{28}Mg	0.1243± 0.0106	6.455± 0.537
^{29}Mg	0.0410± 0.0040	1.078± 0.091
^{30}Mg	0.0007± 0.0001	0.417± 0.037
^{25}Al	0.0018± 0.0002	0.155± 0.016
^{26}Al	0.0512± 0.0036	3.408± 0.299
^{27}Al	0.2977± 0.0196	20.396± 1.727
^{28}Al	0.3358± 0.0221	20.494± 1.694
^{29}Al	0.2792± 0.0192	16.872± 1.360
^{30}Al	0.0895± 0.0078	5.203± 0.412
^{31}Al	0.0362± 0.0043	2.337± 0.183
^{32}Al	0.0121± 0.0016	0.457± 0.038
^{33}Al	0.0004± 0.0001	0.135± 0.013
^{13}Si	0.0024± 0.0003	0.157± 0.016

Isotope	^{136}Xe+p, σ [mb]	^{136}Xe+^{nat}Ti, σ [mb]
^{28}Si	0.0861± 0.0056	5.746± 0.477
^{29}Si	0.2154± 0.0137	14.981± 1.207
^{30}Si	0.3840± 0.0239	26.019± 2.040
^{31}Si	0.2439± 0.0158	14.290± 1.093
^{32}Si	0.1088± 0.0085	6.740± 0.504
^{33}Si	0.0293± 0.0035	1.585± 0.119
^{34}Si	0.0133± 0.0021	0.575± 0.044
^{29}P	0.0162± 0.0010	0.054± 0.007
^{30}P	0.0170± 0.0012	1.126± 0.092
^{31}P	0.1620± 0.0099	11.211± 0.858
^{32}P	0.2558± 0.0154	17.556± 1.306
^{33}P	0.2395± 0.0149	16.889± 1.221
^{34}P	0.1176± 0.0085	7.096± 0.502
^{35}P	0.0532± 0.0051	3.072± 0.214
^{36}P	0.0315± 0.0026	0.729± 0.053
^{31}S	0.0006± 0.0001	0.049± 0.006
^{32}S	0.0219± 0.0014	1.565± 0.120
^{33}S	0.1126± 0.0066	7.753± 0.563
^{34}S	0.2721± 0.0155	18.637± 1.308
^{35}S	0.2196± 0.0129	14.737± 1.005
^{36}S	0.1442± 0.0094	8.824± 0.586
^{37}S	0.0542± 0.0048	3.095± 0.203
^{38}S	0.0200± 0.0026	1.147± 0.076
^{34}Cl	0.0067± 0.0005	0.469± 0.036
^{35}Cl	0.0844± 0.0048	5.749± 0.394
^{36}Cl	0.1896± 0.0104	13.081± 0.866
^{37}Cl	0.2197± 0.0121	15.210± 0.974
^{38}Cl	0.1270± 0.0079	8.505± 0.530
^{39}Cl	0.0698± 0.0055	4.376± 0.267
^{40}Cl	0.0316± 0.0033	1.656± 0.101
^{41}Cl	0.0120± 0.0019	0.575± 0.037
^{36}Ar	0.0097± 0.0006	0.553± 0.040
^{37}Ar	0.0609± 0.0033	3.988± 0.259
^{38}Ar	0.1837± 0.0095	12.219± 0.759
^{39}Ar	0.1992± 0.0104	13.942± 0.837
^{40}Ar	0.1508± 0.0084	9.986± 0.581
^{41}Ar	0.0810± 0.0056	4.993± 0.284
^{42}Ar	0.0369± 0.0035	2.070± 0.117
^{43}Ar	0.0133± 0.0019	0.598± 0.036

Isotope	^{136}Xe+p, σ [mb]	^{136}Xe+^{nat}Ti, σ [mb]
^{38}K	0.0029± 0.0002	0.192± 0.015
^{39}K	0.0449± 0.0024	2.921± 0.179
^{40}K	0.1344± 0.0066	9.212± 0.536
^{41}K	0.1830± 0.0090	12.637± 0.709
^{42}K	0.1479± 0.0077	10.322± 0.560
^{43}K	0.1025± 0.0062	6.510± 0.342
^{44}K	0.0407± 0.0036	2.536± 0.132
^{45}K	0.0170± 0.0021	0.920± 0.050
^{40}Ca	0.0043± 0.0003	0.245± 0.018
^{41}Ca	0.0388± 0.0019	2.436± 0.140
^{42}Ca	0.1266± 0.0059	8.590± 0.466
^{43}Ca	0.1892± 0.0086	12.878± 0.671
^{44}Ca	0.1781± 0.0083	11.914± 0.599
^{45}Ca	0.1065± 0.0059	6.751± 0.329
^{46}Ca	0.0510± 0.0039	3.110± 0.149
^{47}Ca	0.0214± 0.0023	1.006± 0.050
^{42}Sc	0.0013± 0.0001	0.092± 0.008
^{43}Sc	0.0233± 0.0012	1.391± 0.076
^{44}Sc	0.0899± 0.0041	6.056± 0.307
^{45}Sc	0.1769± 0.0076	12.074± 0.584
^{46}Sc	0.1640± 0.0073	11.262± 0.524
^{47}Sc	0.1208± 0.0060	7.892± 0.354
^{48}Sc	0.0598± 0.0041	3.528± 0.156
^{49}Sc	0.0230± 0.0025	1.307± 0.059
^{50}Sc	0.0066± 0.0012	0.317± 0.018
^{44}Ti	0.0163± 0.0007	0.082± 0.007
^{45}Ti	0.0162± 0.0008	0.969± 0.051
^{46}Ti	0.0841± 0.0035	5.396± 0.254
^{47}Ti	0.1579± 0.0063	10.962± 0.490
^{48}Ti	0.1733± 0.0070	11.824± 0.506
^{49}Ti	0.1179± 0.0054	8.037± 0.332
^{50}Ti	0.0647± 0.0039	4.040± 0.163
^{51}Ti	0.0234± 0.0023	1.398± 0.059
^{52}Ti	0.0089± 0.0014	0.448± 0.022
^{46}V	0.0006± 0.0001	0.040± 0.004
^{47}V	0.0133± 0.0006	0.554± 0.029
^{48}V	0.0531± 0.0022	3.597± 0.158
^{49}V	0.1373± 0.0052	9.185± 0.378
^{50}V	0.1602± 0.0061	11.017± 0.433

Isotope	^{136}Xe+p, σ [mb]	^{136}Xe+$^{\mathrm{nat}}$Ti, σ [mb]
^{51}V	0.1238± 0.0051	8.289± 0.313
^{52}V	0.0672± 0.0036	4.044± 0.150
^{53}V	0.0346± 0.0027	1.877± 0.071
^{54}V	0.0117± 0.0015	0.597± 0.026
^{55}V	0.0047± 0.0009	0.219± 0.012
^{48}Cr	0.0004± 0.0001	0.031± 0.004
^{49}Cr	0.0069± 0.0004	0.366± 0.019
^{50}Cr	0.0479± 0.0018	2.647± 0.109
^{51}Cr	0.1226± 0.0042	7.946± 0.298
^{52}Cr	0.1567± 0.0052	10.396± 0.371
^{53}Cr	0.1175± 0.0042	7.567± 0.259
^{54}Cr	0.0751± 0.0030	4.826± 0.159
^{55}Cr	0.0318± 0.0016	1.984± 0.065
^{56}Cr	0.0141± 0.0009	0.866± 0.029
^{57}Cr	0.0054± 0.0005	0.285± 0.010
^{50}Mn	0.0005± 0.0001	0.029± 0.003
^{51}Mn	0.0081± 0.0005	0.418± 0.019
^{52}Mn	0.0556± 0.0024	3.193± 0.120
^{53}Mn	0.1419± 0.0057	9.379± 0.330
^{54}Mn	0.1874± 0.0080	12.773± 0.433
^{55}Mn	0.1673± 0.0078	11.234± 0.372
^{56}Mn	0.0976± 0.0052	6.054± 0.204
^{57}Mn	0.0571± 0.0033	3.452± 0.114
^{58}Mn	0.0249± 0.0016	1.356± 0.047
^{59}Mn	0.0088± 0.0008	0.557± 0.020
^{60}Mn	0.0024± 0.0003	0.169± 0.008
^{53}Fe	0.0064± 0.0004	0.285± 0.013
^{54}Fe	0.0439± 0.0018	2.332± 0.082
^{55}Fe	0.1248± 0.0049	7.392± 0.240
^{56}Fe	0.2026± 0.0080	12.416± 0.384
^{57}Fe	0.1699± 0.0076	10.344± 0.316
^{58}Fe	0.1277± 0.0062	7.560± 0.231
^{59}Fe	0.0601± 0.0036	3.840± 0.120
^{60}Fe	0.0284± 0.0020	1.841± 0.059
^{61}Fe	0.0142± 0.0010	0.677± 0.023
^{62}Fe	0.0053± 0.0004	0.241± 0.010
^{55}Co	0.0036± 0.0003	0.156± 0.008
^{56}Co	0.0283± 0.0013	1.421± 0.048
^{57}Co	0.1048± 0.0039	6.034± 0.180

Isotope	^{136}Xe+p, σ [mb]	^{136}Xe+^{nat}Ti, σ [mb]
^{58}Co	0.1746± 0.0067	10.805± 0.306
^{59}Co	0.2143± 0.0082	12.057± 0.329
^{60}Co	0.1452± 0.0063	7.934± 0.222
^{61}Co	0.0835± 0.0043	4.902± 0.138
^{62}Co	0.0395± 0.0024	2.208± 0.065
^{63}Co	0.0187± 0.0013	0.991± 0.030
^{64}Co	0.0064± 0.0006	0.363± 0.013
^{65}Co	0.0023± 0.0003	0.120± 0.006
^{57}Ni	0.0023± 0.0002	0.084± 0.005
^{58}Ni	0.0200± 0.0009	0.841± 0.029
^{59}Ni	0.0874± 0.0031	4.094± 0.115
^{60}Ni	0.1966± 0.0066	9.936± 0.256
^{61}Ni	0.2198± 0.0080	12.058± 0.298
^{62}Ni	0.1789± 0.0071	10.160± 0.250
^{63}Ni	0.1049± 0.0048	5.744± 0.149
^{64}Ni	0.0589± 0.0031	3.052± 0.081
^{65}Ni	0.0253± 0.0016	1.368± 0.039
^{66}Ni	0.0095± 0.0007	0.513± 0.016
^{67}Ni	0.0031± 0.0003	0.171± 0.007
^{68}Ni	0.0006± 0.0001	0.049± 0.003
^{60}Cu	0.0121± 0.0006	0.430± 0.016
^{61}Cu	0.0620± 0.0022	2.683± 0.073
^{62}Cu	0.1611± 0.0053	7.607± 0.183
^{63}Cu	0.2245± 0.0075	11.687± 0.262
^{64}Cu	0.2039± 0.0072	10.233± 0.230
^{65}Cu	0.1376± 0.0055	7.320± 0.168
^{66}Cu	0.0867± 0.0037	4.047± 0.094
^{67}Cu	0.0410± 0.0021	2.031± 0.050
^{68}Cu	0.0158± 0.0010	0.813± 0.022
^{69}Cu	0.0065± 0.0005	0.296± 0.010
^{70}Cu	0.0016± 0.0002	0.097± 0.005
^{71}Cu	0.0006± 0.0001	0.022± 0.002
^{61}Zr	0.0026± 0.0001	0.026± 0.003
^{62}Zr	0.0104± 0.0005	0.289± 0.011
^{63}Zr	0.0539± 0.0019	1.992± 0.052
^{64}Zr	0.1626± 0.0048	6.849± 0.151
^{65}Zr	0.2404± 0.0074	11.447± 0.232
^{66}Zr	0.2552± 0.0079	11.723± 0.233
^{67}Zr	0.1797± 0.0063	8.583± 0.178
^{68}Zr	0.1186± 0.0044	4.992± 0.107

Isotope	^{136}Xe+p, σ [mb]	^{136}Xe+$^{\mathrm{nat}}$Ti, σ [mb]
^{69}Zr	0.0593± 0.0026	2.589± 0.058
^{70}Zr	0.0264± 0.0014	1.130± 0.028
^{71}Zr	0.0109± 0.0006	0.449± 0.013
^{72}Zr	0.0035± 0.0003	0.147± 0.006
^{73}Zr	0.0009± 0.0001	0.040± 0.003
^{64}Ga	0.0062± 0.0004	0.144± 0.007
^{65}Ga	0.0369± 0.0014	1.144± 0.032
^{66}Ga	0.1216± 0.0037	4.514± 0.100
^{67}Ga	0.2487± 0.0068	9.651± 0.183
^{68}Ga	0.2648± 0.0078	11.499± 0.209
^{69}Ga	0.2231± 0.0068	9.404± 0.178
^{70}Ga	0.1482± 0.0050	6.278± 0.122
^{71}Ga	0.0835± 0.0032	3.643± 0.071
^{72}Ga	0.0407± 0.0019	1.647± 0.036
^{66}Ge	0.0053± 0.0003	0.090± 0.005
^{67}Ge	0.0298± 0.0011	0.781± 0.024
^{68}Ge	0.1174± 0.0032	3.800± 0.081
^{69}Ge	0.2609± 0.0064	8.636± 0.154
^{70}Ge	0.3239± 0.0082	12.306± 0.200
^{71}Ge	0.2784± 0.0075	10.797± 0.182
^{72}Ge	0.2086± 0.0059	7.677± 0.135
^{73}Ge	0.1232± 0.0039	4.346± 0.078
^{74}Ge	0.0608± 0.0023	2.265± 0.044
^{75}Ge	0.0262± 0.0012	0.928± 0.021
^{76}Ge	0.0100± 0.0006	0.357± 0.010
^{68}As	0.0026± 0.0002	0.047± 0.003
^{69}As	0.0200± 0.0008	0.417± 0.014
^{70}As	0.0914± 0.0025	2.361± 0.055
^{71}As	0.2291± 0.0055	7.132± 0.125
^{72}As	0.3352± 0.0080	11.040± 0.170
^{73}As	0.3503± 0.0082	12.040± 0.183
^{74}As	0.2686± 0.0065	8.594± 0.143
^{75}As	0.1832± 0.0048	5.692± 0.093
^{76}As	0.0915± 0.0029	2.887± 0.052
^{77}As	0.0448± 0.0017	1.443± 0.028
^{78}As	0.0179± 0.0008	0.538± 0.013
^{79}As	0.0062± 0.0004	0.200± 0.007
^{80}As	0.0021± 0.0002	0.060± 0.003
^{81}As	0.0007± 0.0001	0.018± 0.002

Isotope	^{136}Xe+p, σ [mb]	^{136}Xe+^{nat}Ti, σ [mb]
^{70}Se	0.0023± 0.0002	0.030± 0.003
^{71}Se	0.0187± 0.0007	0.324± 0.013
^{72}Se	0.0912± 0.0023	1.867± 0.045
^{73}Se	0.2387± 0.0052	5.920± 0.103
^{74}Se	0.4145± 0.0083	11.317± 0.160
^{75}Se	0.4194± 0.0087	12.321± 0.173
^{76}Se	0.3501± 0.0076	10.536± 0.157
^{77}Se	0.2324± 0.0055	6.452± 0.100
^{78}Se	0.1456± 0.0037	3.981± 0.063
^{79}Se	0.0704± 0.0022	1.869± 0.035
^{80}Se	0.0317± 0.0011	0.795± 0.017
^{81}Se	0.0115± 0.0005	0.311± 0.009
^{82}Se	0.0041± 0.0003	0.101± 0.005
^{83}Se	0.0008± 0.0001	0.026± 0.002
^{72}Br	0.0016± 0.0001	0.022± 0.003
^{73}Br	0.0128± 0.0005	0.176± 0.008
^{74}Br	0.0667± 0.0018	1.158± 0.033
^{75}Br	0.2234± 0.0046	4.538± 0.083
^{76}Br	0.4151± 0.0078	9.331± 0.134
^{77}Br	0.5159± 0.0094	12.893± 0.167
^{78}Br	0.4297± 0.0083	10.842± 0.156
^{79}Br	0.3486± 0.0067	8.413± 0.119
^{80}Br	0.2062± 0.0045	4.971± 0.073
^{81}Br	0.1215± 0.0030	2.680± 0.044
^{82}Br	0.0515± 0.0016	1.185± 0.022
^{83}Br	0.0213± 0.0007	0.443± 0.011
^{84}Br	0.0073± 0.0004	0.142± 0.006
^{85}Br	0.0019± 0.0002	0.046± 0.003
^{74}Kr	0.0013± 0.0001	0.014± 0.002
^{75}Kr	0.0114± 0.0005	0.119± 0.007
^{76}Kr	0.0655± 0.0016	0.792± 0.025
^{77}Kr	0.2108± 0.0041	3.509± 0.070
^{78}Kr	0.4773± 0.0080	9.021± 0.125
^{79}Kr	0.6021± 0.0098	11.937± 0.152
^{80}Kr	0.6085± 0.0096	12.776± 0.165
^{81}Kr	0.4688± 0.0078	9.520± 0.130
^{82}Kr	0.3247± 0.0057	6.363± 0.085
^{83}Kr	0.1886± 0.0038	3.495± 0.052
^{84}Kr	0.0901± 0.0022	1.617± 0.028
^{85}Kr	0.0361± 0.0011	0.657± 0.014
^{86}Kr	0.0123± 0.0005	0.223± 0.007

Isotope	^{136}Xe+p, σ [mb]	^{136}Xe+$^{\mathrm{nat}}$Ti, σ [mb]
^{87}Kr	0.0044± 0.0003	0.076± 0.004
^{88}Kr	0.0011± 0.0001	0.023± 0.002
^{77}Rb	0.0066± 0.0003	0.056± 0.004
^{78}Rb	0.0455± 0.0013	0.482± 0.011
^{79}Rb	0.1780± 0.0035	2.554± 0.031
^{80}Rb	0.4305± 0.0070	6.929± 0.067
^{81}Rb	0.7029± 0.0102	12.213± 0.108
^{82}Rb	0.7404± 0.0104	13.007± 0.125
^{83}Rb	0.6835± 0.0094	11.317± 0.112
^{84}Rb	0.4758± 0.0069	7.769± 0.081
^{85}Rb	0.3073± 0.0049	4.590± 0.055
^{86}Rb	0.1515± 0.0030	2.266± 0.033
^{87}Rb	0.0615± 0.0015	0.951± 0.018
^{88}Rb	0.0229± 0.0007	0.356± 0.010
^{89}Rb	0.0088± 0.0004	0.130± 0.005
^{90}Rb	0.0030± 0.0002	0.046± 0.003
^{79}Sr	0.0055± 0.0003	0.034± 0.003
^{80}Sr	0.0384± 0.0007	0.319± 0.009
^{81}Sr	0.1571± 0.0030	1.906± 0.025
^{82}Sr	0.4652± 0.0062	6.298± 0.058
^{83}Sr	0.8233± 0.0081	11.608± 0.098
^{84}Sr	1.0167± 0.0119	14.131± 0.125
^{85}Sr	0.9537± 0.0110	12.911± 0.120
^{86}Sr	0.7316± 0.0086	9.489± 0.091
^{87}Sr	0.4604± 0.0060	5.700± 0.062
^{88}Sr	0.2391± 0.0038	2.785± 0.039
^{89}Sr	0.1095± 0.0021	1.331± 0.021
^{90}Sr	0.0433± 0.0012	0.564± 0.012
^{91}Sr	0.0169± 0.0005	0.204± 0.007
^{92}Sr	0.0074± 0.0003	0.085± 0.004
^{93}Sr	0.0020± 0.0002	0.030± 0.002
^{81}Y	0.0005± 0.0001	0.005± 0.001
^{82}Y	0.0239± 0.0006	0.176± 0.007
^{83}Y	0.1216± 0.0025	1.246± 0.019
^{84}Y	0.4066± 0.0059	4.610± 0.047
^{85}Y	0.8613± 0.0106	10.255± 0.086
^{86}Y	1.2329± 0.0130	14.338± 0.122
^{87}Y	1.3076± 0.0127	14.379± 0.128
^{88}Y	1.0521± 0.0105	11.098± 0.102
^{89}Y	0.6905± 0.0075	6.788± 0.070

Isotope	^{56}Xe+p, σ [mb]	^{56}Xe+$^{\mathrm{nat}}$Ti, σ [mb]
^{90}Y	0.3723± 0.0050	3.610± 0.046
^{91}Y	0.1828± 0.0030	1.784± 0.026
^{92}Y	0.0823± 0.0015	0.803± 0.014
^{93}Y	0.0372± 0.0008	0.364± 0.009
^{94}Y	0.0136± 0.0004	0.145± 0.005
^{95}Y	0.0047± 0.0003	0.056± 0.003
^{96}Y	0.0014± 0.0001	0.018± 0.002
^{84}Y	0.0164± 0.0006	0.120± 0.006
^{85}Y	0.0953± 0.0021	0.837± 0.015
^{86}Y	0.3411± 0.0053	3.585± 0.040
^{87}Y	1.1230± 0.0127	8.986± 0.077
^{88}Y	1.4852± 0.0140	13.952± 0.117
^{89}Y	1.7318± 0.0143	15.194± 0.132
^{90}Y	1.4025± 0.0111	11.799± 0.109
^{91}Y	0.9132± 0.0080	7.659± 0.077
^{92}Y	0.5708± 0.0064	4.593± 0.054
^{93}Y	0.3206± 0.0042	2.455± 0.033
^{94}Y	0.1659± 0.0023	1.308± 0.021
^{95}Y	0.0748± 0.0012	0.637± 0.013
^{96}Y	0.0317± 0.0007	0.277± 0.008
^{97}Y	0.0126± 0.0004	0.119± 0.005
^{99}Y	0.0008± 0.0001	0.015± 0.002
^{86}Nb	0.0250± 0.0010	0.078± 0.010
^{87}Nb	0.0957± 0.0020	0.614± 0.023
^{88}Nb	0.4135± 0.0054	2.932± 0.052
^{89}Nb	1.1560± 0.0131	8.430± 0.106
^{90}Nb	2.1511± 0.0235	14.777± 0.189
^{91}Nb	2.4312± 0.0258	16.505± 0.197
^{92}Nb	1.5777± 0.0120	14.017± 0.205
^{93}Nb	1.2244± 0.0095	9.669± 0.132
^{94}Nb	0.8289± 0.0072	6.437± 0.100
^{95}Nb	0.5387± 0.0056	3.342± 0.048
^{96}Nb	0.2934± 0.0033	1.862± 0.026
^{97}Nb	0.1489± 0.0018	1.002± 0.017
^{98}Nb	0.0666± 0.0010	0.449± 0.010
^{99}Nb	0.0280± 0.0006	0.215± 0.006
^{100}Nb	0.0110± 0.0004	0.086± 0.004
^{89}Mo	0.0745± 0.0017	0.384± 0.011
^{90}Mo	0.4088± 0.0038	2.335± 0.036
^{91}Mo	1.3008± 0.0116	7.653± 0.088
^{92}Mo	2.4831± 0.0391	14.883± 0.299

Isotope	^{56}Xe+p, σ [mb]	^{56}Xe+$^{\mathrm{nat}}$Ti, σ [mb]
^{93}Mo	2.7734$\pm$ 0.0430	15.276$\pm$ 0.290
^{94}Mo	2.2520$\pm$ 0.0305	15.552$\pm$ 0.321
^{95}Mo	1.7403$\pm$ 0.0213	11.545$\pm$ 0.220
^{96}Mo	1.1015$\pm$ 0.0087	9.818$\pm$ 0.227
^{97}Mo	0.7688$\pm$ 0.0065	5.617$\pm$ 0.114
^{98}Mo	0.4766$\pm$ 0.0045	3.188$\pm$ 0.059
^{99}Mo	0.2528$\pm$ 0.0027	1.394$\pm$ 0.020
^{100}Mo	0.1216$\pm$ 0.0014	0.709$\pm$ 0.014
^{101}Mo	0.0572$\pm$ 0.0009	0.354$\pm$ 0.009
^{102}Mo	0.0253$\pm$ 0.0006	0.160$\pm$ 0.005
^{103}Mo	0.0080$\pm$ 0.0003	0.063$\pm$ 0.003
^{104}Mo	0.0016$\pm$ 0.0002	0.017$\pm$ 0.002
^{91}Tc	0.0593$\pm$ 0.0010	0.246$\pm$ 0.009
^{92}Tc	0.3841$\pm$ 0.0036	1.763$\pm$ 0.029
^{93}Tc	1.3539$\pm$ 0.0113	6.421$\pm$ 0.077
^{94}Tc	2.5936$\pm$ 0.0228	12.365$\pm$ 0.147
^{95}Tc	3.3050$\pm$ 0.0322	16.063$\pm$ 0.212
^{96}Tc	2.9981$\pm$ 0.0346	16.320$\pm$ 0.216
^{97}Tc	2.6900$\pm$ 0.0344	15.157$\pm$ 0.211
^{98}Tc	2.0527$\pm$ 0.0297	11.459$\pm$ 0.193
^{99}Tc	1.4779$\pm$ 0.0246	8.304$\pm$ 0.154
^{100}Tc	0.9251$\pm$ 0.0193	5.319$\pm$ 0.113
^{101}Tc	0.5621$\pm$ 0.0148	3.199$\pm$ 0.078
^{102}Tc	0.2900$\pm$ 0.0102	1.654$\pm$ 0.054
^{103}Tc	0.1377$\pm$ 0.0065	0.836$\pm$ 0.040
^{104}Tc	0.0580$\pm$ 0.0039	0.463$\pm$ 0.031
^{105}Tc	0.0226$\pm$ 0.0023	0.210$\pm$ 0.022
^{106}Tc	0.0082$\pm$ 0.0014	0.105$\pm$ 0.019
^{93}Ru	0.0464$\pm$ 0.0008	0.169$\pm$ 0.007
^{94}Ru	0.3513$\pm$ 0.0031	1.319$\pm$ 0.024
^{95}Ru	1.2130$\pm$ 0.0099	4.791$\pm$ 0.063
^{96}Ru	2.7075$\pm$ 0.0219	10.491$\pm$ 0.128
^{97}Ru	3.8486$\pm$ 0.0333	15.013$\pm$ 0.199
^{98}Ru	3.9725$\pm$ 0.0389	17.770$\pm$ 0.228
^{99}Ru	3.6169$\pm$ 0.0396	17.172$\pm$ 0.221
^{100}Ru	3.2249$\pm$ 0.0372	14.982$\pm$ 0.218
^{101}Ru	2.3858$\pm$ 0.0315	11.149$\pm$ 0.185
^{102}Ru	1.5911$\pm$ 0.0251	7.708$\pm$ 0.142
^{103}Ru	0.9442$\pm$ 0.0193	4.697$\pm$ 0.097
^{104}Ru	0.5223$\pm$ 0.0141	2.745$\pm$ 0.070
^{105}Ru	0.2664$\pm$ 0.0092	1.401$\pm$ 0.050
^{106}Ru	0.1287$\pm$ 0.0059	0.786$\pm$ 0.040

Isotope	^{56}Xe+p, σ [mb]	^{56}Xe+^{nat}Ti, σ [mb]
^{107}Ru	0.0533± 0.0036	0.331± 0.027
^{109}Ru	0.0094± 0.0012	0.075± 0.016
^{95}Rh	0.0358± 0.0007	0.094± 0.005
^{96}Rh	0.2637± 0.0025	0.807± 0.019
^{97}Rh	1.0658± 0.0084	3.315± 0.050
^{98}Rh	2.5335± 0.0199	8.246± 0.107
^{99}Rh	4.2821± 0.0336	13.778± 0.183
^{100}Rh	4.8053± 0.0416	17.354± 0.228
^{101}Rh	4.8421± 0.0450	19.284± 0.232
^{102}Rh	4.3278± 0.0430	17.024± 0.230
^{103}Rh	3.5774± 0.0385	14.236± 0.214
^{104}Rh	2.5568± 0.0316	10.447± 0.168
^{105}Rh	1.7053± 0.0259	7.373± 0.125
^{106}Rh	1.0103± 0.0196	4.351± 0.089
^{107}Rh	0.5750± 0.0138	2.509± 0.066
^{108}Rh	0.2782± 0.0091	1.396± 0.052
^{109}Rh	0.1351± 0.0058	0.688± 0.038
^{110}Rh	0.0544± 0.0035	0.334± 0.028
^{111}Rh	0.0198± 0.0021	0.187± 0.024
^{112}Rh	0.0063± 0.0012	0.072± 0.015
^{97}Pd	0.0206± 0.0005	0.053± 0.004
^{98}Pd	0.1865± 0.0020	0.473± 0.014
^{99}Pd	0.8308± 0.0067	2.257± 0.040
^{100}Pd	2.3428± 0.0179	6.337± 0.089
^{101}Pd	4.3249± 0.0324	12.101± 0.166
^{102}Pd	5.8431± 0.0446	17.194± 0.229
^{103}Pd	5.8029± 0.0483	19.694± 0.233
^{104}Pd	5.8821± 0.0503	19.937± 0.245
^{105}Pd	5.0748± 0.0457	17.882± 0.243
^{106}Pd	3.9476± 0.0394	13.927± 0.197
^{107}Pd	2.7681± 0.0329	10.380± 0.157
^{108}Pd	1.8296± 0.0264	6.752± 0.111
^{109}Pd	1.0857± 0.0197	4.182± 0.086
^{110}Pd	0.5793± 0.0133	2.580± 0.070
^{111}Pd	0.2856± 0.0086	1.368± 0.052
^{112}Pd	0.1352± 0.0057	0.732± 0.041
^{113}Pd	0.0608± 0.0037	0.417± 0.034
^{114}Pd	0.0261± 0.0024	0.229± 0.029
^{115}Pd	0.0084± 0.0015	0.159± 0.026
^{116}Pd	0.0013± 0.0003	0.009± 0.002

Isotope	^{56}Xe+p, σ [mb]	^{56}Xe+$^{\mathrm{nat}}$Ti, σ [mb]
^{99}Ac	0.0114± 0.0004	0.021± 0.002
^{100}Ac	0.1093± 0.0014	0.227± 0.009
^{101}Ac	0.5826± 0.0051	1.308± 0.029
^{102}Ac	1.8515± 0.0150	4.324± 0.070
^{103}Ac	4.1343± 0.0302	9.894± 0.141
^{104}Ac	6.1337± 0.0444	15.273± 0.216
^{105}Ac	6.8510± 0.0517	19.705± 0.233
^{106}Ac	7.1013± 0.0552	20.986± 0.248
^{107}Ac	6.7268± 0.0522	21.039± 0.265
^{108}Ac	5.5952± 0.0472	17.745± 0.227
^{109}Ac	4.4443± 0.0413	14.432± 0.193
^{110}Ac	3.0183± 0.0340	10.186± 0.137
^{111}Ac	2.0183± 0.0275	7.181± 0.113
^{112}Ac	1.1716± 0.0190	4.401± 0.089
^{113}Ac	0.6884± 0.0139	2.861± 0.075
^{114}Ac	0.3277± 0.0088	1.517± 0.058
^{115}Ac	0.1897± 0.0064	0.850± 0.044
^{116}Ac	0.0834± 0.0042	0.453± 0.036
^{117}Ac	0.0386± 0.0030	0.224± 0.030
^{118}Ac	0.0169± 0.0021	0.102± 0.023
^{119}Ac	0.0060± 0.0008	0.032± 0.004
^{120}Ac	0.0041± 0.0005	0.027± 0.004
^{121}Ac	0.0005± 0.0000	0.004± 0.001
^{102}Cd	0.0575± 0.0010	0.102± 0.006
^{103}Cd	0.3490± 0.0037	0.690± 0.020
^{104}Cd	1.3818± 0.0121	2.725± 0.053
^{105}Cd	3.5089± 0.0263	7.283± 0.115
^{106}Cd	6.1707± 0.0432	13.384± 0.200
^{107}Cd	7.2274± 0.0523	18.751± 0.229
^{108}Cd	8.1508± 0.0587	22.338± 0.253
^{109}Cd	8.3153± 0.0584	22.833± 0.269
^{110}Cd	7.3435± 0.0545	21.824± 0.262
^{111}Cd	6.1457± 0.0480	18.909± 0.225
^{112}Cd	4.7049± 0.0427	14.931± 0.175
^{113}Cd	3.3297± 0.0355	11.077± 0.143
^{114}Cd	2.2037± 0.0268	7.668± 0.114
^{115}Cd	1.3456± 0.0200	4.856± 0.097
^{116}Cd	0.7675± 0.0135	3.167± 0.082
^{117}Cd	0.4478± 0.0103	1.874± 0.064
^{118}Cd	0.2310± 0.0068	0.985± 0.051
^{119}Cd	0.1133± 0.0050	0.577± 0.043

Isotope	^{56}Xe+p, σ [mb]	^{56}Xe+^{nat}Ti, σ [mb]
^{120}Cd	0.0623± 0.0039	0.393± 0.046
^{121}Cd	0.0411± 0.0049	0.166± 0.026
^{122}Cd	0.0317± 0.0014	0.068± 0.007
^{123}Cd	0.0126± 0.0008	0.026± 0.005
^{124}Cd	0.0024± 0.0001	0.009± 0.001
^{125}Cd	0.0005± 0.0000	0.006± 0.001
^{104}In	0.0233± 0.0006	0.043± 0.004
^{105}In	0.1677± 0.0022	0.280± 0.012
^{106}In	0.8028± 0.0086	1.421± 0.037
^{107}In	2.4810± 0.0211	4.682± 0.088
^{108}In	5.0818± 0.0379	9.792± 0.166
^{109}In	7.2306± 0.0514	16.107± 0.217
^{110}In	8.2473± 0.0582	21.308± 0.243
^{111}In	9.3966± 0.0621	24.172± 0.271
^{112}In	9.0801± 0.0604	24.920± 0.290
^{113}In	8.3512± 0.0559	23.498± 0.251
^{114}In	6.9158± 0.0519	20.592± 0.219
^{115}In	5.3073± 0.0442	16.630± 0.174
^{116}In	3.9075± 0.0372	12.220± 0.144
^{117}In	2.6695± 0.0280	9.067± 0.132
^{118}In	1.7047± 0.0208	5.900± 0.106
^{119}In	1.0895± 0.0160	4.259± 0.099
^{120}In	0.6223± 0.0112	2.540± 0.076
^{121}In	0.3697± 0.0089	1.463± 0.066
^{122}In	0.2028± 0.0067	0.953± 0.063
^{123}In	0.1358± 0.0055	0.478± 0.052
^{124}In	0.0909± 0.0025	0.159± 0.010
^{125}In	0.0359± 0.0016	0.126± 0.010
^{127}In	0.0032± 0.0001	0.018± 0.002
^{107}Sn	0.0683± 0.0013	0.107± 0.008
^{108}Sn	0.3911± 0.0056	0.678± 0.024
^{109}Sn	1.4834± 0.0154	2.591± 0.062
^{110}Sn	3.7637± 0.0317	6.693± 0.132
^{111}Sn	6.2227± 0.0466	12.638± 0.198
^{112}Sn	7.9118± 0.0561	18.925± 0.225
^{113}Sn	9.7129± 0.0641	23.774± 0.267
^{114}Sn	10.3230± 0.0637	26.380± 0.302
^{115}Sn	10.2070± 0.0626	27.576± 0.273
^{116}Sn	9.3961± 0.0599	26.512± 0.263
^{117}Sn	7.8670± 0.0537	22.733± 0.200
^{118}Sn	6.3578± 0.0493	19.447± 0.188
^{119}Sn	4.7991± 0.0375	15.131± 0.164

Isotope	^{56}Xe+p, σ [mb]	^{56}Xe+$^{\mathrm{nat}}$Ti, σ [mb]
^{120}Sn	3.3753± 0.0312	11.786± 0.149
^{121}Sn	2.2841± 0.0226	8.658± 0.138
^{122}Sn	1.5711± 0.0188	5.753± 0.110
^{123}Sn	1.0105± 0.0140	4.144± 0.108
^{124}Sn	0.5923± 0.0114	2.467± 0.092
^{125}Sn	0.3445± 0.0091	1.596± 0.093
^{127}Sn	0.1764± 0.0034	0.434± 0.016
^{128}Sn	0.0431± 0.0019	0.289± 0.014
^{129}Sn	0.0145± 0.0002	0.055± 0.003
^{130}Sn	0.0041± 0.0001	0.020± 0.002
^{110}Sb	0.1272± 0.0029	0.215± 0.013
^{111}Sb	0.5910± 0.0093	0.964± 0.036
^{112}Sb	1.9187± 0.0215	3.171± 0.086
^{113}Sb	4.0896± 0.0370	7.933± 0.160
^{114}Sb	5.7150± 0.0469	13.148± 0.185
^{115}Sb	8.2591± 0.0594	19.330± 0.240
^{116}Sb	9.7863± 0.0615	24.245± 0.286
^{117}Sb	10.9081± 0.0658	28.307± 0.288
^{118}Sb	10.8855± 0.0629	30.035± 0.287
^{119}Sb	10.4755± 0.0631	29.461± 0.234
^{120}Sb	9.1172± 0.0584	27.687± 0.231
^{121}Sb	8.0986± 0.0506	24.501± 0.199
^{122}Sb	6.3476± 0.0437	21.388± 0.207
^{123}Sb	4.9736± 0.0337	17.549± 0.185
^{124}Sb	3.8579± 0.0307	14.034± 0.179
^{125}Sb	2.8392± 0.0232	10.879± 0.159
^{126}Sb	1.9673± 0.0208	7.824± 0.152
^{127}Sb	1.3618± 0.0171	5.585± 0.152
^{128}Sb	0.8959± 0.0170	3.773± 0.149
^{130}Sb	0.3780± 0.0052	1.013± 0.028
^{131}Sb	0.2330± 0.0034	0.481± 0.011
^{111}Te	0.0063± 0.0004	0.009± 0.002
^{112}Te	0.0469± 0.0017	0.068± 0.007
^{113}Te	0.2363± 0.0057	0.390± 0.022
^{114}Te	0.9716± 0.0150	1.649± 0.059
^{115}Te	2.4495± 0.0279	4.496± 0.121
^{116}Te	3.9228± 0.0388	8.650± 0.151
^{117}Te	6.0060± 0.0498	13.958± 0.204
^{118}Te	8.1506± 0.0575	19.641± 0.249
^{119}Te	9.5356± 0.0625	26.012± 0.294
^{120}Te	11.0342± 0.0641	29.897± 0.280

Isotope	^{56}Xe+p, σ [mb]	^{56}Xe+^{nat}Ti, σ [mb]
^{121}Te	11.6976± 0.0662	33.705± 0.274
^{122}Te	11.4786± 0.0650	34.300± 0.261
^{123}Te	11.2267± 0.0626	33.605± 0.234
^{124}Te	10.0910± 0.0536	32.853± 0.264
^{125}Te	8.9245± 0.0478	30.609± 0.234
^{126}Te	7.6362± 0.0408	28.479± 0.277
^{127}Te	6.8880± 0.0386	24.859± 0.231
^{128}Te	5.4211± 0.0320	21.787± 0.259
^{129}Te	4.3572± 0.0322	16.994± 0.249
^{130}Te	3.4273± 0.0282	14.636± 0.296
^{131}Te	3.2944± 0.0177	10.801± 0.138
^{132}Te	2.6947± 0.0128	6.460± 0.060
^{133}Te	2.5928± 0.0141	2.745± 0.052
^{113}I	0.0005± 0.0001	0.001± 0.001
^{114}I	0.0099± 0.0006	0.035± 0.006
^{115}I	0.0735± 0.0031	0.149± 0.017
^{116}I	0.3335± 0.0082	0.565± 0.033
^{117}I	1.0227± 0.0179	1.816± 0.076
^{118}I	1.9137± 0.0264	4.187± 0.105
^{119}I	3.3764± 0.0372	8.197± 0.154
^{120}I	4.9332± 0.0446	12.251± 0.192
^{121}I	6.8523± 0.0515	18.286± 0.258
^{122}I	8.3089± 0.0560	23.011± 0.239
^{123}I	10.3006± 0.0618	30.544± 0.285
^{124}I	10.8514± 0.0649	33.098± 0.235
^{125}I	12.4245± 0.0681	40.743± 0.282
^{126}I	12.1880± 0.0611	39.286± 0.256
^{127}I	13.1836± 0.0613	47.413± 0.305
^{128}I	11.9872± 0.0524	44.143± 0.298
^{129}I	13.6406± 0.0557	52.086± 0.333
^{130}I	11.8021± 0.0474	47.156± 0.334
^{131}I	12.8236± 0.0508	51.246± 0.368
^{132}I	11.6194± 0.0502	48.689± 0.439
^{133}I	12.1454± 0.0643	54.113± 0.593
^{134}I	39.5615± 0.0324	42.664± 0.165
^{116}Xe	0.0024± 0.0003	0.009± 0.003
^{117}Xe	0.0161± 0.0013	0.038± 0.006
^{118}Xe	0.0726± 0.0037	0.143± 0.016
^{119}Xe	0.3288± 0.0099	0.691± 0.046
^{120}Xe	0.7805± 0.0174	1.548± 0.068
^{121}Xe	1.3064± 0.0230	3.154± 0.093

Isotope	^{56}Xe+p, σ [mb]	^{56}Xe+^{nat}Ti, σ [mb]
^{122}Xe	2.3100± 0.0318	5.846± 0.131
^{123}Xe	3.1763± 0.0352	8.633± 0.178
^{124}Xe	4.6516± 0.0428	12.513± 0.178
^{125}Xe	5.6084± 0.0458	17.393± 0.227
^{126}Xe	7.3510± 0.0532	21.314± 0.194
^{127}Xe	8.2564± 0.0566	27.937± 0.256
^{128}Xe	10.2641± 0.0581	33.014± 0.233
^{129}Xe	10.9882± 0.0589	42.290± 0.327
^{130}Xe	12.7411± 0.0562	49.657± 0.309
^{131}Xe	14.0317± 0.0604	62.943± 0.445
^{132}Xe	17.1044± 0.0615	75.913± 0.410
^{133}Xe	18.8146± 0.0657	104.828± 0.655
^{134}Xe	25.1824± 0.0841	203.275± 0.894
^{135}Xe	43.5342± 0.1116	574.042± 2.006
^{121}Cd	0.0481± 0.0037	0.118± 0.017
^{122}Cd	0.1293± 0.0071	0.350± 0.035
^{123}Cd	0.2425± 0.0100	0.682± 0.041
^{124}Cd	0.4371± 0.0143	1.256± 0.062
^{125}Cd	0.6453± 0.0157	1.938± 0.081
^{126}Cd	0.9274± 0.0204	2.944± 0.094
^{127}Cd	1.2430± 0.0207	4.335± 0.106
^{128}Cd	1.5458± 0.0266	5.098± 0.097
^{129}Cd	1.8385± 0.0245	7.071± 0.110
^{130}Cd	2.2056± 0.0311	7.894± 0.106
^{131}Cd	2.4064± 0.0248	9.779± 0.130
^{132}Cd	2.4942± 0.0263	10.725± 0.129
^{133}Cd	2.4032± 0.0215	10.567± 0.145
^{134}Cd	2.1284± 0.0265	8.283± 0.119
^{135}Cd	1.1313± 0.0136	4.940± 0.105
^{136}Cd	0.4027± 0.0095	1.813± 0.060
^{127}Ba	0.0242± 0.0032	0.121± 0.019
^{128}Ba	0.0323± 0.0036	0.192± 0.029
^{129}Ba	0.0321± 0.0035	0.127± 0.019
^{130}Ba	0.0305± 0.0036	0.127± 0.021
^{131}Ba	0.0243± 0.0032	0.121± 0.014
^{132}Ba	0.0128± 0.0023	0.082± 0.015

Bibliography

A.

[Andronenko 1986] MASS YIELD DISTRIBUTIONS FOR 1 GEV PROTON-INDUCED NUCLEAR REACTIONS ON NI AND AG, L.N. Andronenko, A.A. Kotov, L.A. Vaishnene, W. Neubert, H.W. Barz, J.P. Bondorf, R. Donangelo, H. Schulz, Phys. Lett. B 174, 18 (1986).

[Armbruster 2004] MEASUREMENT OF OF A COMPLETE SET OF NUCLIDES, CROSS-SECTIONS AND KINETIC ENERGIES IN SPALLATION OF 238U 1A GEV WITH PROTONS, P. Armbruster, J. Benlliure, M. Bernas, A. Boudard, E. Casarejos, S. Czajkowski, T. Enqvist, S. Leray, P. Napolitani, J. Pereira, F. Rejmund, M.-V. Ricciardi, K.-H. Schmidt, C. Stephan, J. Taieb, L. Tassan-Got, C. Volant arXiv nucl-ex/0406032

[Avdeyev 1998] THERMAL MULTIFRAGMENTATION IN P + AU INTERACTIONS AT 2.16, 3.6 AND 8.1 GEV INCIDENT ENERGIES, S.P. Avdeyev, V.A. Karnaukhov, W.D. Kuznetsov, L.A. Petrov, V.K. Rodionov, A.S. Zubkevich, H. Oeschler, O.V. Bochkarev, L.V. Chulkov, E.A. Kuzmin, A. Budzanovski, W. Karcz, M. Janicki, E. Norbeck, A.S. Botvina, W.A. Friedman, W. N orenberg, G. Papp, Eur. Phys. J. A 3, 75 (1998).

B.

[Babinet 1981] SYSTEMATICS OF COMPLEX FRAGMENT EMISSION IN NIOBIUM-INDUCED REACTIONS, R. Babinet, These, Université de Paris Sud, Orsay (1981).

[Barz 1986] Onset of Multifragmentation Dominance at 1 GeV Proton-Induced Nuclear Reaction for Target Nuclei with A $\leq$ 160, H.W. Barz, J.P. Bondorf, H. Schulz, L.N. Andronenko, A.A. Kotov, L.A. Vaishnene, W. Neubert, Nucl. Phys. A 460, 714 (1986).

[Benlliure 2001] Isotopic production cross sections of fission residues in ^{197}Au-on-proton collisions at 800 A MeV, J. Benlliure, P. Armbruster, M. Bernas A. Boudard, J. P. Dufour, T. Enqvist, R. Legrain, S. Leray, B. Mustapha, F. Rejmund, K.-H. Schmidt, C. Stéphan, L. Tassan-Got, C. Volant, Nucl. Phys. A 683, 513 (2001).

[Benlliure 2002] New approach to determine the angular transmission in zero-degree magnetic spectrometers, J. Benlliure, J. Pereira-Conca, K.-H. Schmidt, Nucl. Instrum. Methods. A 478, 493 (2002).

[Bernas 2002] Fission residues produced in the spallation reaction ^{238}U+p at 1 A GeV, M. Bernas, P. Armbruster, J. Benlliure, A. Boudard, E. Casajeros, S. Czajkowski, T. Enqvist, R. Legrain, S. Leray, B. Mustapha, P. Napolitani, J. Pereira, F. Rejmund, V. Ricciardi, K.-H. Schmidt, C. Stéphan, J. Taieb, L. Tassan-Got, C. Volant, Nucl. Phys. A 725, 213 (2003).

[Blann 1971] Hybrid Model for Pre-Equilibrium Decay in Nuclear Reactions, M.Blann, Phys. Rev. Lett. 27, 337 (1971).

[Bondorf 1985] Statistical multifragmentation of nuclei, J.P. Bondorf, R. Donangelo, I.N. Mishustin, H. Schulz, Nucl. Phys. A 444, 460 (1985).

[Bondorf 1995] Statistical multifragmentation of nuclei, J.P. Bondorf, A.S. Botvina, A.S. Iljinov, I.N. Mishustin, K. Sneppen, Phys. Rep. 257, 133 (1995).

[Borderie 2002] Dynamics and Thermodynamics of the Liquid-Gas Phase Transition in Hot Nuclei Studied with the Marie98 Array, B. Borderie, J. Phys. (London) G 28, R217 (2002).

[Botvina 1985a] Multifragmentation of nuclei at excitation energies 10 MeV/nucleon, A.S. Botvina, A.S. Iljinov, I.N. Mishustin, Yad. Fiz. 42, 1127 (1985); Sov. J. Nucl. Phys., 42, No. 5 712 (1985).

[Botvina 1985b] Multifragmentation of nuclei by high-energy protons, A.S. Botvina, A.S. Iljinov, I.N. Mishustin, JETP Lett. 42, 572 (1985).

[Botvina 1987] STATISTICAL SIMULATION OF THE BREAK-UP OF HIGHLY EXCITED NUCLEI, A.S. Botvina, A.S. Iljinov, I.N. Mishustin, J.P. Bondorf, R. Donangelo, K. Sneppen, Nucl. Phys. A 475, 663 (1987).

[Botvina 1990] MULTIFRAGMENT BREAK-UP OF NUCLEI BY INTERMEDIATE-ENERGY PROTONS, A.S. Botvina, A.S. Iljinov, I.N. Mishustin, Nucl. Phys. A 507, 649 (1990).

[Botvina 1995] MULTIFRAGMENTATION OF SPECTATORS IN RELATIVISTIC HEAVY-ION REACTIONS, A.S. Botvina, I.N. Mishustin, M. Begemann-Blaich, T. Hofmann, J. Hubele, G. Imme, I. Iori, P. Kretz, G.J. Kunde, W.D. Kunze, V. Lindenstruth, U. Lynen, A. Moroni, W.F.J. Müller, C.A. Ogilvie, J. Pochodzalla, G. Raciti, H. Sann, A. Schüttauf, W. Seidel, W. Trautmann, A. Worner, *Nucl. Phys.* A **584**, 737 (1995).

[Botvina 2001] STATISTICAL EVOLUTION OF ISOTOPE COMPOSITION OF NUCLEAR FRAGMENTS, A.S.Botvina and I.N.Mishustin, *Phys. Rev.* C **63**, 061601(R) (2001).

[Boudard 2001] INTRANUCLEAR CASCADE MODEL FOR A COMPREHENSIVE DESCRIPTION OF SPALLATION REACTION DATA, A. Boudard, J. Cugnon, S. Leray, C. Volant, *Phys. Rev.* C **C66**, 044615 (2001).

[Brohm 1994] STATISTICAL ABRASION OF NUCLEONS FROM REALISTIC NUCLEAR-MATTER DISTRIBUTIONS, T. Brohm, K.-H. Schmidt, Nucl. Phys. A 569, 821 (1994).

[Bugaev 2001] STATISTICAL MULTIFRAGMENTATION IN THERMODYNAMIC LIMIT, K.A. Bugaev, M.I. Gorenstein, I.N. Mishustin, W. Greiner, Phys.Lett. B 498, 144 (2001).

[Businaro 1955a] ON THE INTERPRETATION OF FISSION ASYMMETRY ACCORDING TO THE LIQUID DROP NUCLEAR MODEL, U.L. Businaro, S. Gallone, Nuovo Cimento 1, 629 (1955).

[Businaro 1955b] SADDLE SHAPES, THRESHOLD ENERGIES AND FISSION ASYMMETRY ON THE LIQUID DROP MODEL, U.L. Businaro, S. Gallone, Nuovo Cimento 1, 1277 (1955).

[Butler 1963] DEUTERONS FROM HIGH-ENERGY PROTON BOMBARDMENT OF MATTER, S.T. Butler, C.A. Pearson , Phys.Rev. 129, 836 (1963).

C.

[Campi 2003] LITTLE BIG BANG SCENARIO OF MULTIFRAGMENTATION, X. Campi, H. Krivine, E. Plagnol, N. Sator, Phys.Rev. C 67, 044610 (2003).

[Charity 1988] Systematics of complex fragment emission in niobium-induced reactions, R.J. Charity, M.A. McMahan, G.J. Wozniak, R.J. McDonald, L.G. Moretto, D.G. Sarantites, L.G. Sobotka, G. Guarino, A. Pantaleo, L. Fiore, A. Gobbi, K.D. Hildenbrand, Nucl. Phys. A 483, 371 (1988).

[Charity 1998] N-Z distributions of secondary fragments and the evaporation attractor line, R.J. Charity, Phys.Rev. C 58, 1073 (1998).

[Chomaz 2004] Nuclear spinodal fragmentation, P.Chomaz, M.Colonna, J.Randrup, Phys. Rep. 389, 263 (2004).

D.

[D'Agostino 2003] Critical-like behaviours in central and peripheral collisions: a comparative analysis, M.D'Agostino, M.Bruno, F.Gulminelli, R.Bougault, F.Cannata, Ph.Chomaz, F.Gramegna, I.Iori, N.Le Neindre, G.V.Margagliotti, A.Moroni, G.Vannini, J.P.Wieleczko, Nucl. Phys. A 724, 455 (2003).

[Duarte 2000] H. Duarte, Proc. of the SARE-5 workshop on models and codes for spallation neutron sources, Paris, (Jul 2000).

E.

[von Egidy 1987] Interaction and annihilation of antiprotons and nuclei. T. von Egidy, PNature 328, 773 (1987).

[Elliott 2002] Liquid to Vapor Phase Transition in Excited Nuclei, J.B. Elliott, L.G. Moretto, L. Phair, G.J. Wozniak, L. Beaulieu, H. Breuer, R.G. Korteling, K. Kwiatkowski, T. Lefort, L. Pienkowski, A. Ruangma, V.E. Viola, S.J. Yennello, and the ISiS Collaboration, Phys.Rev.Lett. 88, 042701 (2002).

[Enqvist 1999] Systematic experimental survey on projectile fragmentation and fission induced in collisions of ^{238}U at 1 *A GeV* with lead, T. Enqvist, J. Benlliure, F. Farget, K.-H. Schmidt, P. Armbruster, M. Bernas, L. Tassan-Got, A. Boudard, R. Legrain, C. Volant, C. Böckstiegel, M. de Jong, J. P. Dufour, *Nucl. Phys.* A **658**, 47 (1999).

[Enqvist 2001a] Primary-residues production cross sections and kinetic energies in 1 *A GeV* ^{208}Pb on deuterons reactions, T. Enqvist, P. Armbruster, J. Benlliure, M. Bernas, A. Boudard, S. Czajkowski, R. Legrain, S. Leray, B. Mustapha, M. Pravikoff, F. Rejmund, K.-H. Schmidt, C. Stéphan, J. Taieb, L. Tassan-Got, F. Vives, C. Volant, W. Wlazlo, *Nucl. Phys.* A, **703**, 435 (2002).

[Enqvist 2001b] ISOTOPIC YIELDS AND KINETIC ENERGIES OF PRIMARY RESIDUES IN 1 A GEV ^{208}PB + P REACTIONS, T. Enqvist, W. Wlazlo, P. Armbruster, J. Benlliure, M. Bernas, A. Boudard, S. Czajkowski, R. Legrain, S. Leray, B. Mustapha, M. Pravikoff, F. Rejmund, K.-H. Schmidt, C, Stephan, J. Taieb, L. Tassan-Got, C. Volant, Nucl. Phys. A 686, 481 (2001).

F.

[Friedman 1988] BASIS FOR A CHARACTERISTIC TEMPERATURE IN NUCLEAR FRAGMENTATION, W.A. Friedman, Phys.Rev.Lett. 60, 2125 (1988).

[Friedman 1990] RAPID MASSIVE CLUSTER FORMATION, W.A. Friedman, Phys. Rev. C 42, 667 (1990).

G.

[Gaimard 1991] A REEXAMINATION OF THE ABRASION-ABLATION MODEL FOR THE DESCRIPTION OF THE NUCLEAR FRAGMENTATION REACTION, J.-J. Gaimard, K.-H. Schmidt, Nucl. Phys. A 531, 709 (1991).

[Geissel 1992] THE GSI PROJECTILE FRAGMENT SEPARATOR (FRS): A VERSATILE MAGNETIC SYSTEM FOR RELATIVISTIC HEAVY IONS, H. Geissel, P. Armbruster, K.H. Behr, A. Brünle, K. Burkard, M. Chen, H. Folger, B. Franczak, H. Keller, O. Klepper, B. Langenbeck, F. Nickel, E. Pfeng, M. Pfützner, E. Roeckl, K. Rykaczewski, I. Schall, D. Schardt, C. Scheidenberger, K.-H. Schmidt, A. Schroter, T. Schwab, K. Sümmerer, M. Weber, G. Münzenberg, T. Brohm, H.-G. Clerc, M. Fauerbach, J.-J. Gaimard, A. Grewe, E. Hanelt, B. Knödler, M. Steiner, B. Voss, J. Weckenmann, C. Ziegler, A. Magel, H. Wollnik, J.P. Dufour, Y. Fujita, D.J. Vieira, B. Sherrill, Nucl. Instrum. Methods B 70, 286 (1992).

[Goldhaber 1974] STATISTICAL MODEL OF FRAGMENTATION PROCESSES, A.S. Goldhaber, Phys. Lett. B 53, 306 (1974).

[Grover 1962] NUCLEAR REACTIONS OF TANTALUM WITH 5.7-GEV PROTONS, J. Robb Grover, *Phys. Rev.* **126**, 1540 (1962).

[Griffin 1966] STATISTICAL MODEL OF INTERMEDIATE STRUCTURE, J. J. Griffin, Phys. Rev. Lett. 17, 478 (1966).

[Grotowski 1984] SYMMETRIC SPLITTING OF VERY LIGHT SYSTEMS, K. Grotowski, Z. Majka, R. Pl-strokeancta, M. Szczodrak, Y. Chan, G. Guarino, L. G. Moretto, D. J. Morissey, L. G. Sobotka, R. G. Stokstad, I. Tserruya, S. Wald, G. J. Wozniak, Phys. Rev. C 30, 1214 (1984).

[Gross 1997] MICROCANONICAL THERMODYNAMICS AND STATISTICAL FRAGMENTATION OF DISSIPATIVE SYSTEMS. THE TOPOLOGICAL STRUCTURE OF THE N-BODY PHASE SPACE, D.H.E. Gross, Phys.Rep. C 279, 119 (1997).

[Gudima 1983] CASCADE-EXCITON MODEL OF NUCLEAR REACTIONS, K.K. Gudima, S.G. Mashnik, V.D. Toneev, Nucl. Phys. A 401, 329 (1983).

[Gulminelli 2002] SCALING IN THE LATTICE GAS MODEL, F.Gulminelli, Ph.Chomaz, M.Bruno, M.D'Agostino, Phys. Rev. C 65, 051601(R) (2002).

H.

[Hanelt 1992] A METHOD FOR CALCULATING PHASE-SPACE DENSITIES IN ION-OPTICAL SYSTEMS, E. Hanelt, K-H. Schmidt, Nucl. Instrum. Methods A 321, 434 (1992).

[Henzlova 2004] INVESTIGATION OF THE N/Z OF THE HEAVY FRAGMENTATION PRODUCTS-THE ISOSPIN THERMOMETER METHOD D. Henzlova, M.V. Ricciardi, J. Benlliure, A.S. Botvina, T. Enqvist, A. Kelic, P. Napolitani, J. Pereira, K.-H. Schmidt, Prog.Part.Nucl.Phys. 53, 97 (2004).

[Henzlova] D. Henzlova, PhD thesis in progress, GSI, Darmstadt.

[Hirsch 1984] EXPERIMENTAL RESULTS FROM HIGH ENERGY PROTON-NUCLEUS INTERACTIONS, CRITICAL PHENOMENA, AND THE THERMAL LIQUID DROP MODEL OF FRAGMENT PRODUCTION, A.S. Hirsch, A. Bujak, J.E. Finn, L.J. Gutay, R.W. Minich, N.T. Porile, R.P. Scharenberg, and B.C. Stringfellow, Phys. Rev. C 29, 508 (1984).

J.

[Jaqaman 1983] NUCLEAR CONDENSATION, H.R. Jaqaman, A.Z. Mekjian, L. Zamick, Phys.Rev. C 27, 2782 (1983).

[Jaqaman 1989a] COULOMB INSTABILITY OF HOT NUCLEI, H.R. Jaqaman, Phys.Rev. C 39, 169 (1989).

[Jaqaman 1989b] INSTABILITY OF HOT NUCLEI, H.R. Jaqaman, Phys.Rev. C 40, 1677 (1989).

[Junghans 1998] A.R. Junghansa, M. de Jong, H.-G. Clerc, A.V. Ignatyuk, G.A. Kudyaev and K.-H. Schmidt, PROJECTILE-FRAGMENT YIELDS AS A PROBE FOR THE COLLECTIVE ENHANCEMENT IN THE NUCLEAR LEVEL DENSITY, Nucl. Phys. A 629 635 (1998).

[Jurado 2002] Application of a secondary-electron transmission monitor for high-precision intensity measurements of relativistic heavy-ion beams, B. Jurado, K.-H. Schmidt, K.-H. Behr Nucl.Instrum.Methods A 483, 603 (2002).

K.

[Karnaukhov 1999] Multifragmentation Induced by Light Relativistic Projectiles and Heavy Ions: Similarities and differences, V.A. Karnaukhov, S.P. Avdeyev, W.D. Kuznetsov, L.A. Petrov, V.K. Rodionov, A.S. Zubkevich, H. Oeschler, O.V. Bochkarev, L.V. Chulkov, E.A. Kuzmin, A. Budzanowski, W. Karcz, M. Janicki, E. Norbeck, A.S. Botvina, Yad.Fiz. 62, No 2, 2272 (1999); Phys. Atomic Nuclei 62, 237 (1999).

[Karnaukhov 2003a] Thermal Multifragmentation of Hot Nuclei and Liquid-Fog Phase Transition, V.A. Karnaukhov, S.P. Avdeyev, E.V. Duginova, L.A. Petrov, V.K. Rodionov, H. Oeschler, A. Budzanowski, W. Karcz, M. Janicki, O.V. Bochkarev, E.A. Kuzmin, L.V. Chulkov, E. Norbeck, A.S. Botvina, Yad. Fiz. 66, 1282 (2003); Phys. Atomic Nuclei 66, 1242 (2003).

[Karnaukhov 2003b] Critical temperature for the nuclear liquid-gas phase transition, V.A. Karnaukhov, H. Oeschler, S.P. Avdeyev, E.V. Duginova, V.K. Rodionov, A. Budzanowski, W. Karcz, O.V. Bochkarev, E.A. Kuzmin, L.V. Chulkov, E. Norbeck, A.S. Botvina, Phys. Rev. C 67, 011601 (2003).

[Karol 1975] Nucleus-nucleus reaction cross sections at high energies: soft-sphere model, P.J. Karol, Phys. Rev. C 11, 1203 (1975); Proceeding of Symposium on the Hahn-Meitner-Institut f ur Kernforshung,Berlin (1979).

[Kaufman 1976] Nuclear reactions of ^{197}Au with 11.5- and 300-GeV protons, S.B. Kaufman, M.W. Weisfield, E.P. Steinberg, B.D. Wilkins, D. Henderson, *Phys. Rev.* C **14**, 1121 (1976).

[Klotz-Engmann 1987] Transition From Fission to Multifragmentation, G. Klotz-Engmann, H. Oeschler, E. Kankeleit, Y. Cassagnou, M. Conjeaud, R. Dayras, S. Harar, M. Mostefai, R. Legrain, E.C. Pollacco, C. Volant, Phys. Lett. **187 B**, 245 (1987).

[Klotz-Engmann 1989] Properties of binary fission and multifragmentation in the transition regime, G. Klotz-Engmann, H. Oeschler, J. Stroth, E. Kankeleit, Y. Cassagnou, M. Conjeaud, R. Dayras, S. Harar, R. Legrain, B.C. Pollacco, C. Volant, Nucl. Phys. A 499 392 (1989).

[Korteling 1990] LIGHT FRAGMENT EMISSION AS STUDIED BY THE (P,PHE) REACTIONS ON BE AND AG WITH 300 MEV PROTONS, R.G. Korteling, R.E.L. Green, J.M. D'Auria, R.L. Helmer, K.P. Jackson, S.B. Kaufman, B.D. Wilkins, Phys. Rev. C 41, 2571 (1990).

[Kotov 1995] INTERMEDIATE MASS FRAGMENT PRODUCTION ON AU,AG,NI AND AL TARGETS INDUCED BY 1 GEV PROTONS, A.A. Kotov, L.N. Andronenko, M.N. Andronenko, Y.I. Gusev, K.V. Lukashin, W. Neubert, D.M. Seliverstov, I.I. Strakovsky, L.A. Vaishnene, Nucl. Phys. A 583, 575 (1995).

L.

[Levit 1985] COULOMB INSTABILITY IN HOT COMPOUND NUCLEI APPROACHING LIQUID-GAS TRANSITION, S. Levit, P. Bonche, Nucl. Phys. A 437, 426 (1985)

M.

[Marie 1998] EXPERIMENTAL DETERMINATION OF FRAGMENT EXCITATION ENERGIES IN MULTIFRAGMENTATION EVENTS, N. Marie, A. Chbihi, J.B. Natowitz, A. Le Fevre, S. Salou, J.P. Wieleczko, L. Gingras, M.Assenard, G. Auger, Ch.O. Bacri, F. Bocage, B. Borderie, R. Bougault, R. Brou, P. Buchet, J.L. Charvet, J. Cibor, J. Colin, D. Cussol, R. Dayras, A. Demeyer, D. Dore, D. Durand, P. Eudes, J.D. Frankland, E. Galichet, E. Genouin-Duhamel, E. Gerlic, M. Germain, D. Gourio, D. Guinet, K. Hagel, P. Lautesse, J.L. Laville, J.F. Lecolley, T. Lefort, R. Legrain, N. Le Neindre, O. Lopez, M. Louvel, Z. Majka, A.M. Maskay, L. Nalpas, A.D. Nguyen, M. Parlog, J. Peter, E. Plagnol, A. Rahmani, T. Reposeur, M.F. Rivet, E. Rosato, F. Saint-Laurent, J.C. Steckmeyer, M. Stern, G. Tabacaru, B. Tamain, O. Tirel, E. Vient, C. Volant, R. Wada, Phys.Rev. C 58, 256 (1998).

[Moretto 1975] STATISTICAL EMISSION OF LARGE FRAGMENTS: A GENERAL THEORETICAL APPROACH, L.G. Moretto, Nucl. Phys. A 247, 211 (1975).

[Moretto 1989] THE CATEGORICAL SPACE OF FISSION, L.G. Moretto, G.J. Wozniak, Pramana, J. Phys. 33, 209 (1989).

[Morrissey 1989] SYSTEMATICS OF MOMENTUM DISTRIBUTIONS FOR REACTIONS WITH RELATIVISTIC IONS, D.J. Morrissey, Phys. Rev. C 39, 460 (1989).

N.

[Napolitani 2001a] MEASUREMENT OF SPALLATION RESIDUES OF THE REACTION ^{56}FE+P AT 1 $A\ GeV$, P. Napolitani, DEA-report, IPN-Orsay (2001).

[Napolitani 2001b] DETERMINATION OF THE FREEZE-OUT TEMPERATURE BY THE ISOSPIN THERMOMETER, P. Napolitani, K.-H. Schmidt, P. Armbruster, A. S. Botvina, B. Jurado, A. Kelic, M. V. Ricciardi, O. Yordanov, L. Tassan-Got, L. Audouin, F. Rejmund, T. Enqvist, A. Boudard, L. Donadille, C. Volant, J. Benlliure, M. F. Ordonez, J. Pereira , Arnd Junghans, experimental proposal GSI, 2001.

[Napolitani 2002a] DETERMINATION OF THE FREEZE-OUT TEMPERATURE BY THE ISOSPIN THERMOMETER, P. Napolitani, K.-H. Schmidt, P. Armbruster, A.S. Botvina, M.V. Ricciardi, L. Tassan-Got, F. Rejmund, T. Enqvist, Yad.Fiz. 66, No. 8, 1517 (2003); Phys. Atomic Nuclei 66, No. 8, 1471 (2003).

[Napolitani 2002b] BINARY AND MULTIFRAGMENT EMISSION OF LIGHT RESIDUES IN THE SPALLATION OF 56FE, P. Napolitani, A. S. Botvina, F. Rejmund, K.-H. Schmidt, L. Tassan-Got, C. Villagrasa, GSI annual report 2002.

[Napolitani 2003a] SIGNATURE OF BINARY AND MULTIPLE BREAK-UP IN THE PRODUCTION OF LIGHT PARTICLES IN THE REACTIONS 56FE+P AND 56FE+TI AT 1 A GEV". P. Napolitani et Al A. S. Botvina, F. Rejmund, K.-H. Schmidt, L. Tassan-Got, C. Villagrasa. *XLI Int. Winter Meeting on Nuclear Physics* (Bormio, Italy, 2003).

[Napolitani 2003b] A MODEL FOR CONSECUTIVE SPALLATION AND FRAGMENTATION REACTIONS IN INVERSE KINEMATICS AT RELATIVISTIC ENERGIES, P.Napolitani, L.Tassan-Got, P.Armbruster, M.Bernas, Nucl.Phys. A727, 120 (2003).

[Napolitani 2004a] STRUCTURAL EFFECTS IN THE NUCLIDE DISTRIBUTIONS OF THE RESIDUES OF HIGHLY EXCITED SYSTEMS, P.Napolitani, F.Rejmund, L.Tassan-Got, M.V.Ricciardi, A.Kelic, K.-H.Schmidt, O.Yordanov, A.V.Ignatyuk, C.Villagrasa, Int.J.Mod.Phys. E13, 333 (2004).

[Napolitani 2004b] HIGH-RESOLUTION VELOCITY MEASUREMENTS ON FULLY IDENTIFIED LIGHT NUCLIDES PRODUCED IN 56FE + HYDROGEN AND 56FE + TITANIUM SYSTEM, P. Napolitani, K.-H. Schmidt, A. S. Botvina, F. Rejmund, L. Tassan-Got, C. Villagrasa, Preprints GSI-2004-13, INPO-DR-04-03, submittet to PRC, (2004).

[Natowitz 2002] CALORIC CURVES AND CRITICAL BEHAVIOR IN NUCLEI, J.B.Natowitz, R.Wada, K.Hagel, T.Keutgen, M.Murray, A.Makeev, L.Qin, P.Smith, C.Hamilton, Phys.Rev. C 65, 034618 (2002).

[Natowitz 2002] LIMITING TEMPERATURES AND THE EQUATION OF STATE OF NUCLEAR MATTER, J.B.Natowitz, K.Hagel, Y.Ma, M.Murray, L.Qin, R.Wada, J.Wang, Phys.Rev.Lett. C 89, 212701 (2002).

[Nörenberg 2002] STABILITY AND INSTABILITY OF A HOT AND DILUTE NUCLEAR DROPLET II. DISSIPATIVE ISOSCALAR MODES, W.Nörenberg, G.Papp, P.Rozmej Eur.Phys.J. A 14, 43 (2002)

O.

[Odeh 2000] FRAGMENT KINETIC ENERGIES AND MODES OF FRAGMENT FORMATION, T. Odeh, R. Bassini, M. Begemann-Blaich, S. Fritz, S. J. Gaff-Ejakov, D. Gourio, C. Gross, G. Immé, I. Iori, U. Kleinevoss, G. J. Kunde, W. D. Kunze, U. Lynen, V. Maddalena, M. Mahi, T. M ohlenkamp, A. Moroni, W. F. J. M uller, C. Nociforo, B. Ocker, F. Petruzzelli, J. Pochodzalla, G. Raciti, G. Riccobene, F. P. Romano, A. Saija, M. Schnittker, A. Sch uttauf, C. Schwarz, W. Seidel, V. Serfling, C. Sfienti, W. Trautmann, A. Trzcinski, G. Verde, A. W orner, Hongfei Xi, B. Zwieglinski, Phys. Rev. Lett. 84, 4557 (2000).

[Oeschler 1900] VARIATION OF THE COULOMB REPLUSION IN MULTIFRAGMENTATION, H. Oeschler, A.S. Botvina, D.H.E. Gross, S.P. Avdeyev, V.A. Karnaukhov, L.A. Petrov, V.K. Rodionov, O.V. Bochkarev, L.V. Chulkov, E.A. Kuzmin, A. Budzanowski, W. Karcz, M. Janicki, E. Norbeck, Part. and Nucl., Lett. 99, 70 (2000).

P.

[Pochodzalla 1995] PROBING THE NUCLEAR LIQUID-GAS PHASE TRANSITION, J. Pochodzalla, T. Mohlenkamp, T. Rubehn, A. Schüttauf, A. Worner, E. Zude, M. Begemann-Blaich, T. Blaich, H. Emling, A. Ferrero, C. Gross, G. Imme, I. Iori, G.J. Kunde, W.D. Kunze, V. Lindenstruth, U. Lynen, A. Moroni, W.F.J. Müller, B. Ocker, G. Raciti, H. Sann, C. Schwarz, W. Seidel, V. Serfling, J. Stroth, W. Trautmann, A. Trzcinski, A. Tucholski, G. Verde, B. Zwieglinski, Phys.Rev.Lett. 75, 1040 (1995).

R.

[Randrup 1981] THE DISASSEMBLY OF NUCLEAR MATTER J. Randrup, S.E. Koonin Nucl.Phys. A 356, 223 (1981).

[Reinhold 1998] PROJECTILE FRAMENTATION OF ^{129}XE AT $E_{\mathrm{lab}} = 790$ A MEV J.Reinhold, J.Friese, H.-J.Korner, R.Schneider, K.Zeitelhack, H.Geissel, A.Magel, G.Munzenberg, K.Summerer, Phys.Rev. C 58, 247 (1998).

[Ricciardi 2002] M.V. Ricciardi, K.-H. Schmidt, P. Napolitani, F. Rejmund, A. V. Ignatyuk, *Symposium on Nuclear Clusters; from Light*

Exotic to Superheavy Nuclei (Rauischholzhausen, Germany, 2002).

[Ricciardi 2003] THE ISOSPIN THERMOMETER - A NEW METHOD TO DETERMINE THE FREEZE-OUT TEMPERATURE IN FRAGMENTATION REACTIONS", M.V. Ricciardi, A. Botvina, T. Enqvist, P. Napolitani, K.-H. Schmidt, " International Workshop XXXI on Gross Properties of Nuclei and Nuclear Excitations", Hirschegg, Austria, January 12-18, 2003.

[Ricciardi 2003] EXPERIMENTAL INDICATIONS FOR THE RESPONSE OF THE SPECTATOR TO THE PARTICIPANT BLAST, M. V. Ricciardi, T. Enqvist, J. Pereira, J. Benlliure, M. Bernas, E. Casarejos, V. Henzl, A. Kelic, J. Taieb, K.-H. Schmidt, Phys.Rev.Lett. 90 212302 (2003)

[Ricciardi 2004a] COMPLEX NUCLEAR-STRUCTURE PHENOMENA REVEALED FROM THE NUCLIDE PRODUCTION IN FRAGMENTATION REACTIONS, M.V. Ricciardi, A.V. Ignatyuk, A. Kelic, P. Napolitani, F. Rejmund, K.-H. Schmidt, O. Yordanov, Nucl.Phys. A 733, 299 (2004).

[Ricciardi 2004b] M.V. Ricciardi, PhD Thesis, Santiago de Compostela (2004).

[Richert 2001] MICROSCOPIC MODEL APPROACHES TO FRAGMENTATION OF NUCLEI AND PHASE TRANSITIONS IN NUCLEAR MATTER, J. Richert and P. Wagner, Phys. Rep. 350, 1 (2001).

S.

[Sanders 1999] BINARY DECAY OF LIGHT NUCLEAR SYSTEMS, S.J. Sanders, A. Szanto de Toledo, C. Beck, Phys. Rep. 311, 487 (1999).

[Sauer 1976] THERMAL PROPERTIES OF NUCLEI, G. Sauer, H. Chandra, U. Mosel, Nucl. Phys. A 264, 221 (1976).

[Scharenberg 2001] COMPARISON OF 1 A GEV ^{197}AU + C DATA WITH THERMODYNAMICS: THE NATURE OF THE PHASE TRANSITION IN NUCLEAR MULTIFRAGMENTATION, R.P. Scharenberg, B.K. Srivastava, S. Albergo, F. Bieser, F.P. Brady, Z. Caccia, D.A. Cebra, A.D. Chacon, J.L. Chance, Y. Choi, S. Costa, J.B. Elliott, M.L. Gilkes, J.A. Hauger, A.S. Hirsch, E.L. Hjort, A. Insolia, M. Justice, D. Keane, J.C. Kintner, V. Lindenstruth, M.A. Lisa, H.S. Matis, M. McMahan, C. McParland, W.F. J. Müller, D.L. Olson, M.D. Partlan, N.T. Porile, R. Potenza, G. Rai, J. Rasmussen, H.G. Ritter, J. Romanski, J.L. Romero, G.V. Russo, H. Sann, A. Scott, Y. Shao, T.J.M. Symons, M. Tincknell, C. Tuvé, S. Wang, P. Warren, H.H. Wieman, T. Wienold, K. Wolf (EOS Collaboration), Phys.Rev. C 64, 054602 (2001).

[Schmidt 1987] THE MOMENTUM-LOSS ACHROMAT - A NEW METHOD FOR THE ISOTOPICAL SEPARATION OF RELATIVISTIC HEAVY IONS, K-H. Schmidt, E. Hanelt, H. Geissel, G. Münzenberg, J.-P. Dufour, Nucl. Instr. Meth. A 260, 287 (1987).

[Schmidt 2002] PRODUCTION OF NEUTRON-RICH HEAVY RESIDUES AND THE FREEZE-OUT TEMPERATURE IN THE FRAGMENTATION OF RELATIVISTIC 238U PROJECTILES DETERMINED BY THE ISOSPIN THERMOMETER, K.-H.Schmidt, M.V.Ricciardi, A.S.Botvina, T.Enqvist, Nucl. Phys. A 710, 157 (2002).

[Schüttauf 1996a] A. Schüttauf, Ph.D. Thesis, Frankfurt am Main (1996).

[Schüttauf 1996b] UNIVERSALITY OF SPECTATOR FRAGMENTATION AT RELATIVISTIC BOMBARDING ENERGIES, A. Schüttauf, W.D. Kunze, A. Worner, M. Begemann-Blaich, Th. Blaich, D.R. Bowman, R.J. Charity, A. Cosmo, A. Ferrero, C.K. Gelbke, C. Gross, W.C. Hsi, J. Hubele, G. Imme, I. Iori, J. Kempter, P. Kreutz, G.J. Kunde, V. Lindenstruth, M.A. Lisa, W.G. Lynch, U. Lynen, M. Mang, T. Mohlenkamp, A. Moroni, W.F.J. Müller, M. Neumann, B. Ocker, C.A. Ogilvie, G.F. Peaslee, J. Pochodzalla, G. Raciti, F. Rosenberger, Th. Rubehn, H. Sann, C. Schwarz, W. Seidel, V. Serfling, L.G. Sobotka, J. Stroth, L. Stuttge, S. Tomasevic, W. Trautmann, A. Trzcinski, M.B. Tsang, A. Tucholski, G. Verde, C.W. Williams, E. Zude, B. Zwieglinski, Nucl.Phys. A 607, 457 (1996).

[Siemens 1979] EVIDENCE FOR A BLAST WAVE FROM COMPRESSED NUCLEAR MATTER, P.J. Siemens, J.O. Rasmussen, Phys. Rev. Lett. 42, 880 (1979).

[Steinhaeuser 1998] ODD-EVEN EFFECTS OBSERVED IN THE FISSION OF NUCLEI WITH UNPAIRED PROTONS S. Steinhaeuser, J. Benlliure, C. Bockstiegel, H.-G. Clerc, A. Heinz, A. Grewe, M. de Jong, A.R. Junghans, J. Muller, M. Pfutzner, K.-H. Schmidt, *Nucl. Phys.* **A634**, 89 (1998).

[Strutinski 1958] V. M. Strutinski, *Int. Conf. on Nuclear Physics*, p. 617 (Paris, Italy, 1958).

[Sudov 1993] PRODUCTION OF LIGHT PARTICLES AFTER ANTIPROTON-NUCLEUS ANNIHILATION AND THEIR INTERPRETATION WITH STATISTICAL MODELS, A.S.Sudov, A.S.Botvina, A.S.Iljinov, Ye.S.Golubeva, V.G.Nedorezov, H.Daniel, T.von Egidy, F.J.Hartmann, P.Hofmann, W.Kanert, H.S.Plendl, G.Schmidt, C.A.Schug, G.Riepe, *Nucl. Phys.* **A554**, 223 (1993).

T.

[Tavares 1992] A New Systematics of Fragment Total Kinetic Energy Release in Fission, O.A.P. Tavares, M.L. Terranova, Nuovo Cim. A 105, 723 (1992).

[Taieb03] Evaporation residues produced in the spallation reaction 238U + p at 1 A GeV, J. Taieb, K.-H. Schmidt, L. Tassan-Got, P. Armbruster, J. Benlliure, M. Bernas, A. Boudard, E. Casarejos, S. Czajkowski, T. Enqvist, R. Legrain, S. Leray, B. Mustapha, M. Pravikoff, F. Rejmund, C: Stephan, C. Volant, W. Wlazlo *Nucl. Phys.* **A724**, 413 (2003).

[Tracy 1972] Rb and Cs Isotopic Cross Sections from 40-60-Mev-Proton Fission of 238U, 232Th, and 235U B.L. Tracy et Al, J. Chaumont, R. Klapisch, J.M. Nitschke, A.M. Poskanzer, E. Roeckl, C. Thibault, *Phys. Rev* **C5**, 222 (1972).

V.

[Viola 1985] Systematics of Fission Fragment Total Kinetic Energy Release, V.E. Viola, K. Kwiatkowski, M. Walker, Phys. Rev. C 31, 1550 (1985).

W.

[Wang 1999] Source Size and Time Dependence of Multifragmentation Induced by GeV 3He Beams, G. Wang, K. Kwiatkowski, D.S. Bracken, E. Renshaw Foxford, W.-C. Hsi, K.B. Morley, V.E. Viola, N.R. Yoder, C. Volant, R. Legrain, E.C. Pollacco, R.G. Korteling, W.A. Friedman, A. Botvina, J. Brzychczyk, H. Breuer, Phys. Rev. C 60, 014603 (1999).

[Weber 1992] New neutron-rich isotopes in the scandium-to-nickel region, produced by fragmentation of a 500 MeV/u ^{86}Kr beam, M. Weber, C. Donzaud, J.P. Dufour, H. Geissel, A. Grewe, D. Guillemaud-Mueller, H. Keller, M. Lewitowicz, A. Magel, A.C. Mueller, G. Münzenberg, F. Nickel, M. Pfützner, A. Piechaczek, M. Pravikoff, E. Roeckl, K. Rykaczewski, M.G. Saint-Laurent, I. Schall, C. Stephan, K. Sümmerer, L. Tassan-Got, D.J. Vieira, B. Voss, *Z.Physik* A **343**, 67 (1992).

[Westfall 1978] Energy Spectra of Nuclear Fragments Produced by High Energy Protons, G.D. Westfall, R.G. Sextro, A.M. Poskanzer, A.M. Zebelman, G.W. Butler, E.K. Hyde, Phys. Rev. C 17, 1368 (1978).

Y.

[Yariv 1979] Intranuclear cascade calculation of high-energy heavy-ion interaction, Y. Yariv, Z. Fraenkel, *Phys. Rev.* C **20**, 2227 (1979).

[Junghans 1996] A self-calibrating ionisation chamber for the precise intensity calibration of high-energy heavy-ion beam monitors, A. Junghans, H.-G. Clerck, A. Grewe, M. de Jong, J. Müller, K.-H. Schmidt, Nucl. Instr. Meth. A 370, 312 (1996).

Acknowledgments

I would like to express all my gratitude to Karl-Heinz Schmidt and Laurent Tassan-Got for guiding me through so many discoveries, and giding me through the FRagment Separator at relativistic velocity, together with fission fragments and reaction residues. Without their constant supervising and teaching this thesis would not exist.

I am especially indebited to A.S. Botvina, M. Bernas and P. Armbruster for their enlighting explanations and for always helping me in interpreting the fundamental aspects of the data I was analizing.

I am grateful to my youger colligues AleKsandra Kelić , Maria Valentina Ricciardi, O. Jordanov, Beatriz Jurado, Daniela Henzlova, Vladimir Henzl, and Christelle Schmitt for sharing, and increasing our common enthusiasm on our common researches.

I would like to thank Francesca Gulminelli, Bernard Borderie and Nimet Frascaria for accepting to take part in the jury for my dissertation, and for their precious comments and advices.

The experimental data exploited in this paper are part of a vast experimental program devoted to the collection of nuclear data for the design of accelerator-driven subcritical reactors. I would like to thank the colleagues who partecipated to the measurement of ^{136}Xe+p and ^{136}Xe+$^{\mathrm{nat}}$Ti : L. Audouin, J. Benlliure, E. Cassarejos, T. Enqvist, M. Fernández Ordóñez, A. Heinz, D. Henzlova, V. Henzl, A. Kelic, A. Lafriaskh, S. Leray, J. Perieira Conca, M.V. Ricciardi, F. Rejmund, K.-H. Schmidt, C. Schmitt, L. Tassan-Got, C. Villagrasa, C. Volant, and O. Yordanov. I'm also grateful to the participants of the measurement of ^{56}Fe+p and ^{56}Fe+$^{\mathrm{nat}}$Ti : L. Audouin, C.-O. Bacri, J. Benlliure, B. Berthier, A. Boudard, E. Casarejos, J.J. Connell, S. Czajkowski, J.-E. Ducret, T. Enqvist, T. Faestermann, B. Fernandez, L. Ferrant, J.S. George, F. Hammache, A. Heinz, K. Helariutta, A.R. Junghans, B. Jurado, D. Karamanis, S. Leray, R.A. Mewaldt, M. Fernández Ordóñez, J. Pereira-Conca, F. Rejmund, M.V. Ricciardi, K.-H. Schmidt, K. Sümmerer, C. Stéphan,

L. Tassan-Got, C. Villagrasa, F. Vivès, C. Volant, M.E. Wiedenbeck, and N.E. Yanasak.

July 2004